9-2011

Search for Contact Interactions with Dimuons at the Atlas Detector

Emily Thompson
University of Massachusetts Amherst, emily.thompson@gmail.com

SEARCH FOR CONTACT INTERACTIONS WITH DIMUONS AT THE ATLAS DETECTOR

A Dissertation Presented

by

EMILY THOMPSON

Submitted to the Graduate School of the
University of Massachusetts Amherst in partial fulfillment
of the requirements for the degree of

DOCTOR OF PHILOSOPHY

September 2011

Physics

SEARCH FOR CONTACT INTERACTIONS WITH DIMUONS AT THE ATLAS DETECTOR

A Dissertation Presented

by

EMILY THOMPSON

Approved as to style and content by:

Stéphane Willocq, Chair

Benjamin Brau, Member

Eugene Golowich, Member

Stephen Schneider, Member

Donald Candela, Department Chair
Physics

To my family and my friends, all over the world.

ABSTRACT

SEARCH FOR CONTACT INTERACTIONS WITH DIMUONS AT THE ATLAS DETECTOR

SEPTEMBER 2011

EMILY THOMPSON

B.Sc., CALIFORNIA STATE POLYTECHNIC UNIVERSITY, POMONA

M.Sc., UNIVERSITY OF MASSACHUSETTS, AMHERST

Ph.D., UNIVERSITY OF MASSACHUSETTS, AMHERST

Directed by: Professor Stéphane Willocq

The Standard Model has been very successful over the last few decades in its agreement with experimental evidence; however there are some remaining puzzles in our understanding of the Universe which have yet to be solved. Even if the Higgs boson and Super Symmetry are discovered, questions still arise, such as why Nature is primarily made of matter when antimatter should have been produced in equal amounts at the beginning of the Universe, why the fundamental particles have the mass hierarchy that they do, what the nature of dark matter is, or whether or not quarks and leptons are themselves made of constituent parts, just to name a few. Theories Beyond the Standard Model attempt to tackle these questions, and also provide alternative explanations for electroweak symmetry breaking in case the Higgs mechanism in the Standard Model contradicts what is observed. The ATLAS detector was

built to discover new physics from high-energy proton-proton collisions delivered by the Large Hadron Collider and to probe the electroweak scale with hard interactions at energies near $\sim$1 TeV. While searching for new physics processes occurring at a much higher invariant mass than available at previous colliders, understanding the performance of the detector is crucial, especially during the first few months of running. This thesis presents a motivation for using dimuons to search for new physics in early ATLAS data, a measurement of the $Z^0/\gamma^* \to \mu\mu$ cross section as a first test of Standard Model theoretical predictions at $\sqrt{s}$ =7 TeV, and finally a search for new physics via a four-fermion contact interaction in the dimuon channel ($qq\mu\mu$) using the full 2010 data set.

TABLE OF CONTENTS

LIST OF TABLES

Table **Page**

LIST OF FIGURES

Figure **Page**

INTRODUCTION

Over the last few decades, experimental results have consistently agreed with the observable expectations of electromagnetic and weak unification in the Standard Model (SM); yet the cause of electroweak symmetry breaking (EWSB), necessary to give mass to the $W^{\pm}$ and Z^0 bosons, remains unconfirmed. While the Higgs mechanism tends to be the most popular theoretical explanation for EWSB, it suffers from the "Hierarchy Problem" (quadratic divergences of radiative corrections to the Higgs mass). The SM also contains 21 arbitrary parameters, and is unable to account for the number of quark/lepton families, matter-antimatter asymmetry, dark matter, or gravity. In the past few decades many theories beyond the Standard Model (BSM) have been developed to address these limitations.

At the Large Hadron Collider (LHC), electroweak (EW) processes are produced mainly through quark/antiquark annihilation in proton-proton collisions. New physics interactions resulting in two muons in the final state have been chosen for this analysis, as they provide a clean signature in the early data recorded by the ATLAS detector. One way to model a new interaction is in the form of a 4-fermion contact interaction, in which the internal production mechanism and fermion couplings remain unknown, but whose presence will still produce an excess of events in the tail of the dimuon invariant mass distribution.

This thesis begins in Chapter 1 by discussing a history of the SM focusing on the EW interaction. The theoretical motivation behind new physics searches at the EW scale is discussed here, and an introduction to proton-proton collider physics is presented, including a description of the Monte Carlo event generators used in the analyses presented in this thesis. Chapter 2 introduces the ATLAS detector at the

LHC at CERN. An emphasis on the ATLAS muon spectrometer (MS) along with the expected performance of high-momentum muons is presented, as the MS is a critical component for the results presented here. Chapter 3 provides detailed information about the detector simulation for contact interaction signals as well as the $Z/\gamma^* \to \mu\mu$ Drell-Yan (DY) process and expected dimuon background processes. Chapter 4 summarizes the first $Z/\gamma^* \to \mu\mu$ cross section measurement performed with 331 nb^{-1} of data and provides the first confirmation of theoretical predictions of the DY produced at $\sqrt{s} = 7$ TeV. Muon performance and selection criteria shown in this chapter are built upon for new physics searches involving dimuons. Chapter 5 begins with detailing the full 2010 dataset used for the contact interaction search. The corrections made to the signal and background simulation samples to provide better agreement with observed data are discussed. In Chapter 6 the event and muon selection for the contact interaction analysis is presented. Here, a data-driven estimation of cosmic-ray muon contamination is shown, as well as the procedure to normalize the SM simulation to the data in the Z^0 peak control region. Finally, kinematic distributions of data and simulation after all selection, simulation corrections and normalization are shown. Chapter 7 begins by illustrating a consistency check of the data with SM expectations. As there was no evidence for the presence of new physics in the data, the thesis proceeds with a discussion of the limit setting procedure for the $qq\mu\mu$ contact interaction energy scale Λ using a Bayesian approach. Chapter 8 discusses all of the mass-dependent systematic uncertainties and how these are handled in the limit calculation. Chapter 9 shows the resulting limits calculated in the Bayesian method described in Chapter 7 and incorporating all of the systematic uncertainties described in Chapter 8. The future of this analysis as the LHC continues to provide data over the next few years is also discussed. Finally, Chapter 10 concludes the thesis and provides a summary of the results presented within.

CHAPTER 1

THEORETICAL BACKGROUND

This chapter introduces the Standard Model of particle physics and in particular details the history and theory of the electroweak interaction. As there are still remaining questions which are not addressed in the Standard Model, a motivation for searching for new physics beyond Standard Model is also presented. In particular, various contact interaction models are shown, along with a review of previous searches. Finally, an introduction to proton-proton collider phenomenology is given to define terminology to be used throughout this thesis.

1.1 Introduction to the Standard Model

The Standard Model (SM) is the accepted theoretical framework which describes the world of particle physics as we understand it today. It is a relativistic quantum field theory (QFT) which characterizes the known fundamental particles and describes the electromagnetic, weak and strong interactions between them. Using a gauge symmetry group $SU(3)_C \times SU(2)_L \times U(1)_Y$, electric charge, color charge, weak isospin and weak hypercharge are conserved in the three interactions. The fourth force in nature, gravity, is not accounted for within its framework. All fundamental particles which have been observed can be divided into two categories according to their spin: fermions which have spin 1/2, and bosons which have spin 1. Matter in the Universe is made of fermions (which also include composite particles like the proton), and the particles which mediate interactions between them are "gauge" bosons, as these force carriers are described within the context of QFT. The SM also allows for every

particle to have an anti-particle partner with the same mass and spin but opposite charge.

Quarks and Leptons - Fundamental fermions are divided into two types: leptons and quarks. There are six of each, not counting antiparticles. The lightest charged lepton is the electron (e^-), followed by the heavier muon (μ^-) and even more massive tau lepton (τ^-), each with electric charge $-e$, where e is the fundamental charge. Thus, their antiparticle partners are positively charged: e^+, μ^+ and τ^+. The other three leptons are the neutrinos (ν_e, ν_μ and ν_τ) which correspond to each of the three charged leptons. Since it is not currently known whether or not the neutral neutrino is its own antiparticle[1], anti-neutrinos are given a separate notation, denoted $\bar{\nu}_e$, $\bar{\nu}_\mu$ and $\bar{\nu}_\tau$. Quarks come in six "flavors" and carry fractional charge with respect to e: up, charm and top quarks (u, c, t) have charge $+\frac{2}{3}e$ and down, strange and bottom quarks (d, s, b) have charge $-\frac{1}{3}e$. The antiquarks, labeled as $\bar{u}$, $\bar{c}$, $\bar{t}$, $\bar{d}$, $\bar{s}$ and $\bar{b}$ carry opposite charge with respect to their quark partners. The quarks and leptons are organized in three families (or "generations"), each containing a doublet of leptons and a doublet of quarks, arranged in order of mass:

$$\begin{array}{cccc} & \text{Leptons:} & & \\ \text{I} & \text{II} & \text{III} & \end{array} \qquad \begin{array}{ccc} & \text{Quarks:} & \\ \text{I} & \text{II} & \text{III} \end{array}$$

$$\begin{pmatrix} \nu_e \\ e \end{pmatrix} \quad \begin{pmatrix} \nu_\mu \\ \mu \end{pmatrix} \quad \begin{pmatrix} \nu_\tau \\ \tau \end{pmatrix}, \qquad \begin{pmatrix} u \\ d \end{pmatrix} \quad \begin{pmatrix} c \\ s \end{pmatrix} \quad \begin{pmatrix} t \\ b \end{pmatrix}.$$

In QFT, fermions are represented by the Dirac field ψ_f, and follow anti-commutation rules (resulting from the Pauli exclusion principle).

Force Carriers - As mentioned above, each interaction is mediated by a spin-1 gauge boson with an energy characterized by the invariant quantity $q^2 = q_\mu q^\mu$, the

[1]If the neutrino is its own antiparticle, then it would be the only Majorana fermion in nature (as opposed to Dirac fermions). Current experiments are looking for evidence that there are non-Dirac fermions in neutrino-less double beta decays.

scalar product of the interaction 4-momentum with itself. From a QFT perspective, bosons in an interaction act as propagators transmitting information from one fermion to another, represented as internal lines on Feynman diagrams. Due to the Heisenberg uncertainty principle, a so-called "virtual boson" can exist on borrowed energy for a very limited amount of time (as long as it satisfies $\Delta E \Delta t < \hbar$), giving it an effective mass different from its rest mass (or "off-shell", rather than "on-shell"). No matter what the process is, energy and momentum are *always* conserved in the full interaction.

Perhaps the most familiar force is the electromagnetic (EM) interaction, mediated by the photon and acting only on charged particles. The coupling constant of the photon to a charged particle $g_e = \sqrt{4\pi\alpha}$ depends on the fine structure constant:

$$\alpha = \frac{e^2}{\hbar c} \simeq \frac{1}{137} \tag{1.1}$$

(from now on, all units will be "natural", that is $\hbar = c = 1$). Because the photon is massless, the EM force is considered "long-range" and is responsible for nearly all the (non-gravitational) forces we feel on a macroscopic scale. It also holds the electrons and protons together inside the atom. The electromagnetic force is a vector interaction represented by the Dirac matrices operator γ^μ, with current given by

$$J^\mu_{em} = \sum_f q_f \bar{\psi}_f \gamma^\mu \psi_f \ , \tag{1.2}$$

where q_f is the charge of the fermion.

The strong interaction is aptly named, for it has the largest coupling of the four forces of nature. Within the atomic nucleus, the strong force holds the protons and neutrons together (via pion exchange), while inside the protons and neutrons themselves it binds the quarks together. The force is mediated by the gluon which only couples to particles having "color", giving rise to the name of the strong interaction

theory: Quantum Chromodynamics (QCD). Quarks come in three colors (red, blue and green) thus feeling the strong force while the colorless leptons do not. The gluon is massless like its electromagnetic counterpart, however, its behavior is fundamentally different than that of the photon. Gluons also carry color, and so can couple to themselves. At a small interaction energy, this causes the strong coupling perturbative calculations to blow up with the addition of higher and higher-order gluon loops. To solve this, a cutoff is introduced and the strong coupling $g_s = \sqrt{4\pi\alpha_s}$ can only be perturbatively calculated for energies much larger than the QCD scale Λ_s (around $\sim$200 MeV):

$$\alpha_s(q^2) \propto \frac{1}{\ln(q^2/\Lambda_s^2)} \quad (\text{for } |q^2| \gg \Lambda_s^2) \ , \tag{1.3}$$

where q^2 is the Lorentz invariant square of the mediating gauge boson four-momentum. The strong interaction becomes weaker as q^2 increases, a very important idea known as asymptotic freedom. Likewise, as q^2 decreases the interaction becomes very strong (also known as confinement) and is the reason why quarks are not seen as free particles and the effects of the strong force are not felt on a macroscopic scale.

The weak force has a few very distinct features. Unlike the electromagnetic or strong forces, the weak interaction is mediated by massive bosons, two charged (W^- and its antiparticle W^+) and one neutral (Z^0, which is its own antiparticle). Due to these massive force carriers, the weak force is short range[2]. The charged current exchange of either a W^+ or W^- boson is the only interaction which can change the flavor of quarks or change the charged leptons into their corresponding neutrinos (and vice versa). The $W^\pm$ bosons can couple to themselves, and because of their charge, the photon as well. Even more striking, $W^\pm$ bosons only couple to left-handed fermions. The neutral current interaction involves the exchange of a Z^0 boson and couples to all

[2]In fact, $\alpha_W \simeq \frac{1}{30}$, more than 4 times stronger than the electromagnetic coupling. However, as will be shown later, the mass of the $W^\pm$ enters the denominator of the propagator term, causing the interaction to be much weaker at low q^2.

fundamental particles except the gluon (because the Z^0 boson does not carry color) and the photon (because the Z^0 boson does not carry charge). In 1970, S.D. Drell and T.M. Yan proposed lepton pair production was possible in hadron collisions either via an electromagnetic or a weak interaction [1], and the process $q\bar{q} \to Z/\gamma^* \to \ell^+\ell^-$ was named after them. Searches for flavor-changing neutral currents (FCNC) have been performed, but so far none have been observed, indicating that the exchange of a neutral boson cannot change the flavor of quarks or leptons.

The fundamental particles in the SM are shown in Fig. 1.1 [2] along with their masses.

1.2 Electroweak Interaction

Throughout the history of fundamental physics, theorists have attempted to combine the forces observed in Nature into compact and elegant forms. Just as J. C. Maxwell joined the electric and magnetic forces to form the theory of electromagnetism in the early 1860's, the EM and weak forces have been similarly combined within the Standard Model. The story of the weak interaction and subsequent development into the electroweak (EW) force starts in 1930 with Wolfgang Pauli.

1.2.1 The Fermi Interaction

By the 1930's, the theory of quantum electrodynamics (QED) and the concept of particle-wave duality had been experimentally confirmed. In nuclear decay, emitted photons (γ) and helium nuclei (α) were observed with discrete energies as predicted. However in β-decay, in which a neutron was observed to decay into a proton while emitting an electron, the electron energy spectrum was observed as a smooth continuum, seemingly defying conservation of energy. Pauli postulated that another particle was also emitted at the time of the neutron decay to solve the energy conservation problem, but would have to be very light or massless to be consistent with the β-

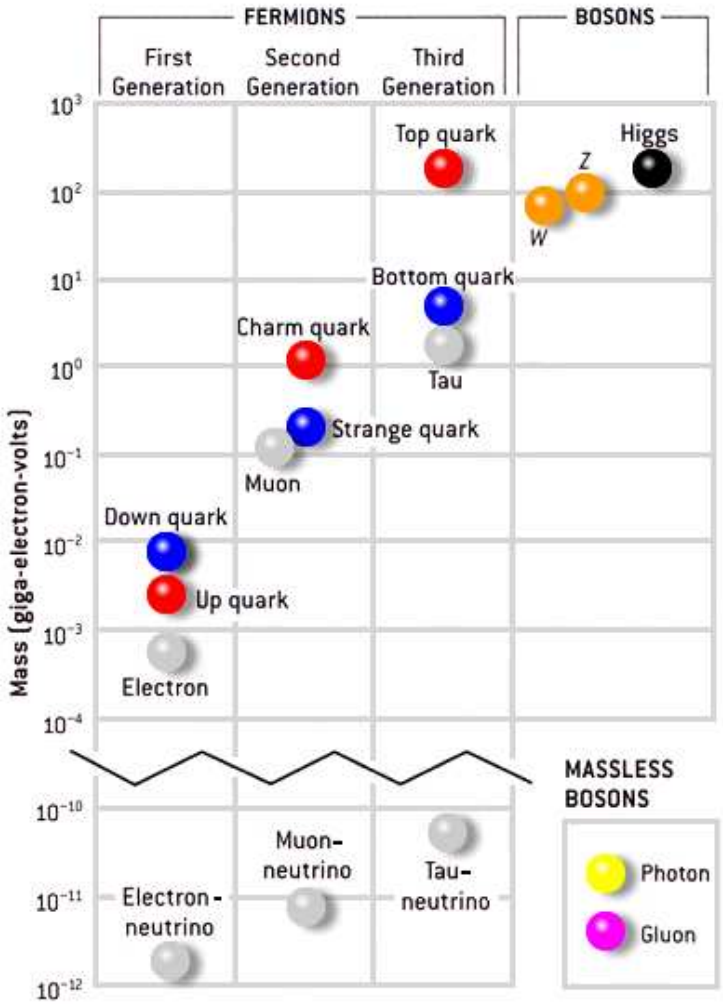

Figure 1.1. Particles described in the Standard Model, arranged according to their masses and generations. The scalar Higgs boson, while necessary in the Standard Model to break electroweak symmetry, has not yet been observed.

decay energy spectrum and neutral to avoid detection [3]. Enrico Fermi picked up on this idea, calling it a "neutrino" (Italian for something "small" and "neutral") and described a 4-point interaction for β-decay as $n \to pe^- \bar{\nu}_e$ [4], fifty years before the mediator of the interaction, the W^- boson, was directly observed (Fig. 1.2).

In analogy to electromagnetism, the interaction was described with a vector coupling and the matrix element had the form:

$$M = \frac{G_F}{\sqrt{2}}[\bar{u}_P \gamma^\mu u_N][\bar{u}_e \gamma \mu v_\nu], \tag{1.4}$$

where G_F is the four-particle coupling constant, also known as the Fermi constant, and u_P, u_N, u_e, v_ν are the proton, neutron, electron and neutrino wave functions, respectively. Later, it was recognized that the fundamental interaction was between charged partons (quarks inside the proton and neutron) rather than the proton and neutron themselves, and would need to include a yet-to-be-discovered massive propagator to save it from divergences at high energy:

$$G_F = \frac{\sqrt{2} g_w^2}{8 M_W^2} \quad (\text{at } |q^2| \ll M_W^2), \tag{1.5}$$

where M_W is the mass of the W boson, and g_w is the charged weak coupling constant.

1.2.2 Development of Electroweak Theory

In the 1950's, the strong and electromagnetic forces were known to conserve parity; that is, a transformation reversing spatial coordinates via the parity operator P would leave the interaction unchanged. In 1956, T.D. Lee and C.N. Yang suggested that the decay of the strange K^+ meson violated parity[3], because the same particle seemed to decay to both an even ($\pi^+\pi^+\pi^-$) and an odd ($\pi^+\pi^0$) state [5]. An experiment

[3]At the time, the K^+ was thought to be two distinct particles, the τ and the θ. Though they decayed differently, their mass, lifetime and properties were otherwise identical.

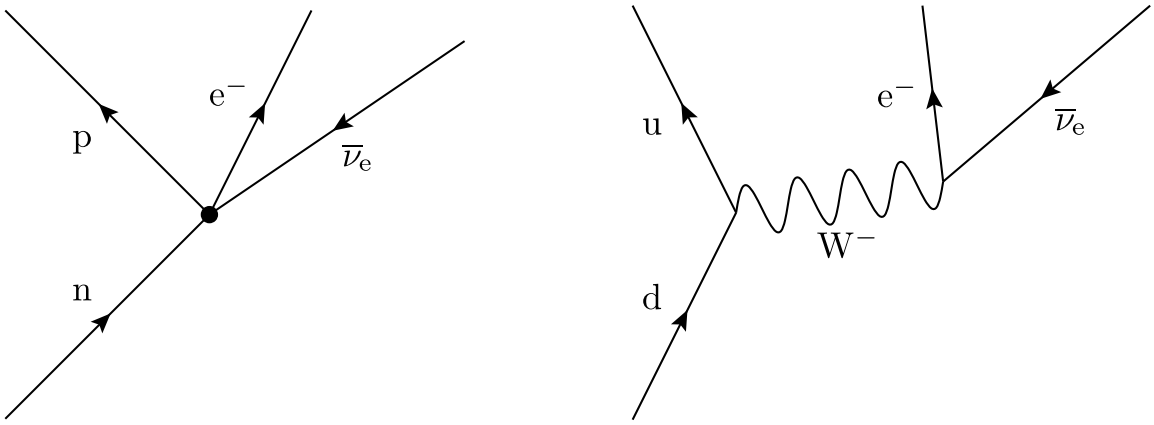

Figure 1.2. The 4-point Fermi interaction describing neutron β-decay (left) and how β-decay is understood today (right). Here, time flows from bottom to top.

by C.S. Wu confirmed that particles undergoing weak interactions not only violated parity conservation, they were *maximally* parity-violating [6]. With this discovery, the vector description Fermi used in his 4-point interaction needed to be revised. Also, all experimental evidence (in muon and strange meson decays) showed that only fermions with left-handed chirality (or right-handed anti-fermions) interacted with the charged weak interaction. In 1958, R. Feynman and M. Gell-Man developed a combination vector (γ^μ) and axial ($\gamma^\mu\gamma^5$) form of the Lagrangian (**V-A**) to account for this [7]. The charged weak current for the decay of a down quark to an up quark was then given by:

$$J^\mu = \bar{\psi_u}\gamma^\mu(1-\gamma^5)\psi_d \ . \tag{1.6}$$

The left-handed fermion fields were introduced as $\psi_{f,L} \equiv \frac{1}{2}(1-\gamma^5)\psi_f$.

While parity-violation in these interactions was finally accepted as a fact of Nature by the early 1960's, theorists still assumed that a system in which both charge *and* parity (together, CP) were reversed would be conserved. This too was found to be false. In 1963, J. Cronin and V. Fitch designed an experiment to show that the short-lived neutral kaon K_s^0 always decayed into either $\pi^+\pi^-$ or $\pi^0\pi^0$, while the longer-lived

K_L^0 would not. However, very rarely, the K_L^0 did in fact decay into two π mesons, verifying the existence of CP violation [8].

In another kaon decay mode, $K^+ \rightarrow \mu^+\nu$, where the positively charged kaon consists of an up and an anti-strange quark, the weak current seemed to allow for first and second generation quarks to interact with each other. In 1963, N. Cabibbo brilliantly hypothesized that the quark weak eigenstates were a superposition of the mass eigenstates [9]. At the time, only the up, down and strange quarks were known to exist. In Cabibbo's theory, the charged weak interaction sees the first generation quarks as:

$$\begin{pmatrix} \psi_u \\ \psi'_d \end{pmatrix} = \begin{pmatrix} \psi_u \\ \psi_d \cos\theta_C + \psi_s \sin\theta_C \end{pmatrix}. \tag{1.7}$$

The quark mixing angle θ_C (also known as the Cabibbo angle) preserves "universality", meaning that the weak coupling constant for quarks is the same as for the leptonic weak interaction. The charged weak current then became

$$J^\mu = \bar{\psi_u}\gamma^\mu(1-\gamma^5)[\psi_d \cos\theta_C + \psi_s \sin\theta_C]. \tag{1.8}$$

In 1970, S. Glashow, J. Iliopoulos and L. Maiani expanded the weak current further with quark mixing to the general form [10]:

$$J^\mu = \bar{U}\ \gamma^\mu(1-\gamma^5)\ C\ D, \quad \text{where:}$$

$$U = \begin{pmatrix} \psi_u \\ \psi_c \end{pmatrix}, \quad D = \begin{pmatrix} \psi_d \\ \psi_s \end{pmatrix} \quad \text{and} \quad C = \begin{pmatrix} \cos\theta_C & \sin\theta_C \\ -\sin\theta_C & \cos\theta_C \end{pmatrix}. \tag{1.9}$$

This extension, named the GIM mechanism after its authors, introduced a fourth quark c (the charm) which was discovered in 1974 as a bound $c\bar{c}$ resonance, now called the J/ψ particle [11, 12]. Finally, after CP violation could not be explained in

the 4-quark model, implying that there was a third family of quarks, the GIM matrix was expanded by M. Kobayashi and T. Maskawa to include a third generation and the mixing terms between them [13]. This matrix which transforms the quarks from mass eigenstates of the strong interaction to weak eigenstates is known today as the Cabibbo-Kobayashi-Maskawa (V_{CKM}) matrix:

$$\begin{pmatrix} \psi'_d \\ \psi'_s \\ \psi'_b \end{pmatrix} = V_{CKM} \begin{pmatrix} \psi_d \\ \psi_s \\ \psi_b \end{pmatrix} = \begin{pmatrix} V_{ud} & V_{us} & V_{ub} \\ V_{cd} & V_{cs} & V_{cb} \\ V_{td} & V_{ts} & V_{tb} \end{pmatrix} \begin{pmatrix} \psi_d \\ \psi_s \\ \psi_b \end{pmatrix} \quad . \tag{1.10}$$

The nine elements in the V_{CKM} matrix can be reduced to 4 independent terms. These values are truly fundamental parameters of the SM and need to be experimentally determined [14]. Finally, the charged weak current (disregarding neutrino oscillations) is given by:

$$J^{\mu}_{ch} \;=\; \bar{\psi}_{\nu}\, \gamma^{\mu}\, \psi_{\ell} \;+\; \bar{\psi}_{U}\, \gamma^{\mu}\, V_{CKM}\, \psi_{D} \quad . \tag{1.11}$$

Here, ψ_{ν} are the neutrino fields, ψ_{ℓ} are the charged-lepton fields, and ψ_U, ψ_D are the triplets of the up- and down-type quark fields, respectively.

So far, only the *charged* weak interaction has been discussed. The neutral weak interaction was first postulated in 1958 by S. Bludman [15]. At the time, the idea did not gain too much traction because not only was there a lack of necessity in any of the previous theories, it was also very difficult to see, as the only "pure" neutral weak interaction came in the form of neutrino scattering (the charged quarks and leptons could also undergo neutral weak interactions, but the photon interaction dominates at low q^2).

In 1961, knowing that the weak interaction was short range, Glashow required a massive neutral weak force carrier in the unification of the electromagnetic and weak interactions [16]. The weak interaction alone is described by the $SU(2)_L$ group (generated by "weak isospin" I, with the subscript L indicating that the weak force

interacts with left-handed particles only) and the EM interaction by the $U(1)_{em}$ group. These are unified into a single gauge group of the form $SU(2)_L \times U(1)_Y$, with the weak hypercharge Y generating $U(1)_Y$. All gauge fields corresponding to the unified group ($W_\mu^{(1,2)}$ and W_μ^0 from the $SU(2)_L$ group and B_μ^0 from the $U(1)_Y$ group) have zero mass. While the new symmetry group worked above the electroweak energy scale, below this some other mechanism was needed in order to break the symmetry and give the weak gauge bosons mass. In 1967-68, S. Weinberg and A. Salam proposed spontaneous symmetry breaking via the Higgs mechanism [17, 18]. A transformation from the electroweak eigenstate into the mass eigenstate formed after symmetry-breaking in the Lagrangian leaves a mass term in the neutral weak field Z_μ, while the mass term for the photon field A_μ cancels out. The transformation is given by:

$$\begin{pmatrix} A_\mu \\ Z_\mu \end{pmatrix} = \begin{pmatrix} \cos\theta_w & \sin\theta_w \\ -\sin\theta_w & \cos\theta_w \end{pmatrix} \begin{pmatrix} B_\mu^0 \\ W_\mu^0 \end{pmatrix}, \tag{1.12}$$

Here, θ_w is the weak mixing angle (also called the Weinberg angle). It is another fundamental parameter in the Standard Model, with a measured value of $\sin^2\theta_w \approx 0.22$.

There are quite a few consequences resulting from this formalism. First, $SU(2) \times U(1)_Y$ is spontaneously broken to the $U(1)_{em}$ group representing electromagnetism. In this scheme the charge Q (playing the role of generator of the $U(1)_{em}$ group) is a linear combination of the weak hypercharge Y and I_3, a component of the weak isospin: $Q = \frac{1}{2}Y + I_3$. Combining the terms in this way, the electromagnetic field does not couple to the Higgs field, keeping the photon massless. Second, the fermions are allowed to interact with the Higgs field, providing a mechanism to give them mass. Third, through the mixing of the neutral currents, the Z^0 gauge field is essentially rotated with respect to the $W^\pm$, giving it a slightly different mass:

Table 1.1. Coefficients to the vector (c_V) and axial (c_A) components of the neutral weak coupling to quarks and leptons.

	c_V	c_A
$\nu_e,\ \nu_\mu,\ \nu_\tau$	1/2	1/2
$e^-,\ \mu^-,\ \tau^-$	-1/2 + 2 $\sin^2\theta_w$	-1/2
$u,\ c,\ t$	1/2 - 4/3 $\sin^2\theta_w$	1/2
$d,\ s,\ b$	-1/2 + 2/3 $\sin^2\theta_w$	-1/2

$$M_Z = \frac{M_W}{\cos\theta_w} \ . \tag{1.13}$$

In addition, the electromagnetic, charged weak and neutral weak coupling constants are related to one another via the weak mixing angle:

$$g_w = \frac{g_e}{\sin\theta_w}, \qquad g_z = \frac{g_e}{\sin\theta_w \cos\theta_w} \ , \tag{1.14}$$

allowing for a theoretical prediction of the mass of the weak gauge bosons. Also because V_{CKM} is a unitary matrix, the neutral current is prohibited from changing the flavor of quarks. The neutral weak current is expressed by:

$$J^\mu_{f,ntl} = \bar{\psi_f}\gamma^\mu(c_V - c_A\gamma^5)\psi_f \ , \tag{1.15}$$

where c_V and c_A depend on the flavor of the fermion and are expressed in terms of θ_w (listed in Table 1.1) [19]. Unlike the charged weak bosons, the Z^0 *is* allowed to couple to right-handed chiral fermions. Finally, the introduction of the Higgs mechanism requires a new massive spin-0 particle: the Higgs boson.

The Lagrangian for the EW interaction after spontaneous symmetry breaking can be written in terms of the currents using Eqns. (1.2), (1.11) and (1.15):

$$L^{EW}_{int} = -\frac{g_w}{\sqrt{8}}(W^+_\mu J^\mu_{ch} + W^-_\mu J^{\mu\dagger}_{ch}) - g_e\cos\theta_w A_\mu J^\mu_{em} - \frac{g_z}{2} Z_\mu J^\mu_{ntl} \ , \tag{1.16}$$

where the first term describes the charged weak interaction[4], the second term describes the EM interaction, and the last term describes the neutral weak interaction [20].

By 1972, once G. 't Hooft and M. Veltman showed that the theory was renormalizable [21], all the pieces seemed to be in place for the Glashow-Weinberg-Salam (GWS) model of the electroweak interaction to be either experimentally validated or rejected. The first evidence of neutral currents was found by the Gargamelle neutrino-scattering experiment in 1973 [22, 23]. Finally, 10 years later, the $W^{\pm}$ and Z^0 gauge bosons were discovered by the UA1 and UA2 collaborations at the Super Proton Synchrotron [24, 25, 26, 27], with masses equal, within error, to those predicted by the GWS model.

The GWS model eventually became known as the Standard Model of particle physics after holding up against experimental tests for the last 40 years and requiring only small modifications (to allow for neutrino mass, for example). Evidence of the tau lepton first came in 1974, confirming the existence of the third generation [28]. The bottom quark was observed at Fermilab in 1977 [29], but it wasn't until 1995 at the Tevatron when the top quark was discovered [30, 31]. Finally, the third generation neutrino ν_τ was observed in 2000 [32]. To this day, all evidence seems to suggest that the SM is the best description of particle physics, with one major piece missing: the scalar Higgs boson has yet to be observed. Discovery of the Higgs boson is crucial to the stability of the theory, and without it, spontaneous EW-symmetry breaking must be explained in some other way.

---

[4]The charged electroweak gauge field mass eigenstates are also superpositions of the electroweak eigenstates:

$$W_\mu^+ = \frac{W_\mu^1 + iW_\mu^2}{\sqrt{2}}, \quad W_\mu^- = \frac{W_\mu^1 - iW_\mu^2}{\sqrt{2}}.$$

1.3 Beyond the Standard Model

After searches for the Higgs boson have been unsuccessful thus far, exploring the $\mathcal{O}(1\text{ TeV})$ energy regime in order to understand the true nature of EWSB has become more important than ever, and the door is wide open for alternative theories beyond the Standard Model to predict what lays beyond the current energy frontier. Already, the fact that neutrinos have mass is perhaps the most striking experimental evidence of new physics, as this was not expected in the original formulation of the Standard Model. In addition, many questions remain unanswered. There is no particular reason why the fermions have the masses that they do, nor why the V_{CKM} matrix elements, responsible for quark flavor mixing, have the relative values they do. The reason why there are exactly three generations of quarks and leptons and why each generation is a heavier copy of the previous is not explained, maybe hinting at some underlying symmetry which has yet to be recognized. The SM also cannot explain why the Universe is mostly made of matter rather than antimatter, nor the origin or composition of dark matter. The LHC was built to probe the electroweak scale in the hopes of answering some of these questions and more, and perhaps discover some surprises as well.

1.3.1 Contact Interactions

The most striking evidence of the presence of beyond the Standard Model (BSM) physics at the LHC would be the direct observation of a new massive particle appearing as a resonance. However, new interactions may take place at energy scales much higher than what is accessible at the LHC. In the same spirit as Fermi described β-decay long before the discovery of the $W^{\pm}$ bosons, one can write an effective Lagrangian describing a new vector interaction without knowing the intermediate process. In the neutral current interaction, the Lagrangian is given by [33]:

$$L = \frac{g^2}{2\Lambda^2}\left[\ \eta_{LL}\left(\bar{\psi}_L\gamma^\mu\psi_L\right)\left(\bar{\psi}'_L\gamma_\mu\psi'_L\right) + \eta_{RR}\left(\bar{\psi}_R\gamma^\mu\psi_R\right)\left(\bar{\psi}'_R\gamma_\mu\psi'_R\right)\right.$$

$$+ \quad \eta_{LR}\left(\bar{\psi}_L\gamma^\mu\psi_L\right)\left(\bar{\psi}'_R\gamma_\mu\psi'_R\right) + \eta_{RL}\left(\bar{\psi}_R\gamma^\mu\psi_R\right)\left(\bar{\psi}'_L\gamma_\mu\psi'_L\right) \ ] \ , \tag{1.17}$$

where g is a coupling constant defined by $g^2 \equiv 4\pi$, and $\psi_{L,R}$ and $\psi'_{L,R}$ are the incoming and outgoing left and right fermionic fields, respectively. The parameter Λ sets the energy scale of the interaction. Experimentally, the presence of a contact interaction (CI) appears as an excess of events in the tail of the diquark or dilepton invariant mass distribution. The value of η is the sign of the interaction term causing either constructive ($\eta = -1$) or destructive ($\eta = +1$) interference with the SM Drell-Yan (DY) process.

Some examples of contact interaction diagrams are shown in Fig. 1.3. In particular, the Lagrangian for the 4-fermion contact interaction with a dimuon final state ($qq\mu\mu$) is given by:

$$\begin{aligned} L &= \frac{g^2}{2\Lambda^2}\left[\ \eta_{LL}\left(\bar{q}_L\gamma^\mu q_L\right)\left(\bar{\mu}_L\gamma_\mu\mu_L\right) + \eta_{LR}\left(\bar{q}_L\gamma^\mu q_L\right)\left(\bar{\mu}_R\gamma_\mu\mu_R\right)\right. \\ &+ \left.\ \eta_{RL}\left(\bar{q}_R\gamma^\mu q_R\right)\left(\bar{\mu}_L\gamma_\mu\mu_L\right) + \eta_{RR}\left(\bar{q}_R\gamma^\mu q_R\right)\left(\bar{\mu}_L\gamma_\mu\mu_L\right)\ \right] \ . \end{aligned} \tag{1.18}$$

Here, $q_{L,R}$ are left or right quark doublets and $\mu_{L,R}$ are the left or right muon fields. Often for search purposes, the terms in this Lagrangian are treated as different models.

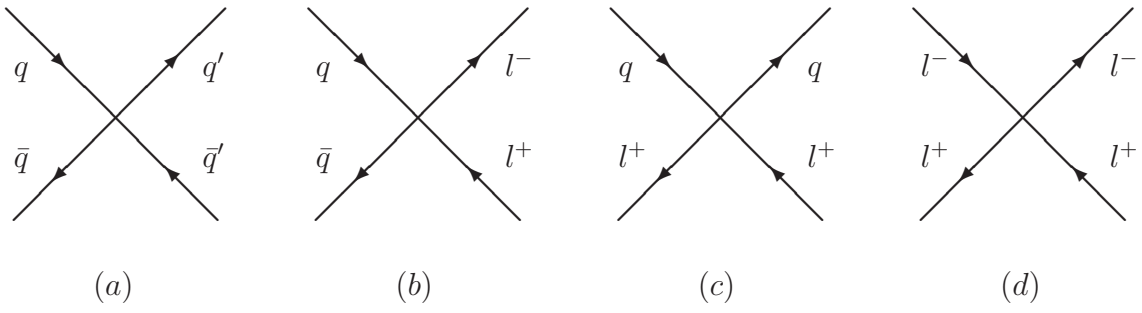

Figure 1.3. Representative Feynman diagrams for various 4-fermion contact interactions. Examples of possible production are shown for (a, b) hadron colliders, (c) hadron-lepton colliders, such as HERA, and (d) lepton colliders, such as LEP.

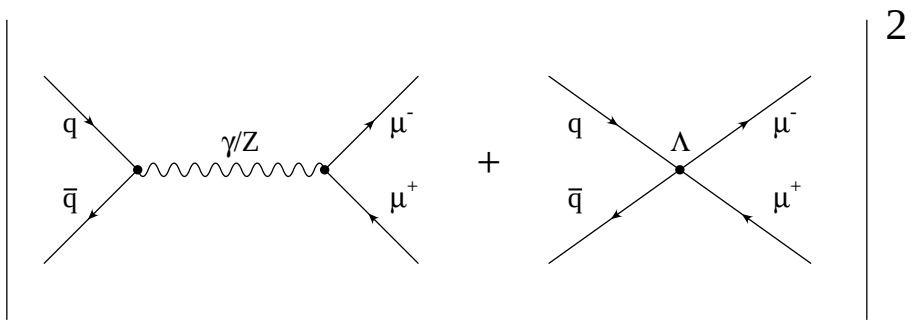

Figure 1.4. Leading order production mechanism of Drell-Yan with additional contact term with scale Λ in the dimuon final state.

With the introduction of this new interaction (Fig. 1.4), the differential cross section for the process $q\,\bar{q} \to \mu^+\mu^-$ is given in terms of the dimuon mass $m_{\mu\mu}$ by

$$\frac{d\sigma}{dm_{\mu\mu}} = \frac{d\sigma_{DY}}{dm_{\mu\mu}} - \eta_{LL}\frac{F_I(m_{\mu\mu})}{\Lambda^2} + \frac{F_C(m_{\mu\mu})}{\Lambda^4}\ , \tag{1.19}$$

which includes a Λ-independent DY term, as well as DY-CI interference (F_I) and pure contact interaction (F_C) terms. Depending on the model of new physics, there may be different interpretations of the scale Λ, two of which are discussed in the next sections

1.3.2 Extra Dimensions in the ADD model

The first concept of extra dimensions began around the beginning of the 20$^{\text{th}}$ century, when T. Kaluza and O. Klein attempted to unify general relativity and electromagnetism by adding an extra spatial dimension [34, 35]. While their initial attempt was unsuccessful, various theories of extra dimensions were developed in the years that followed. In particular, the ADD model of large extra dimensions (LED) is an effective theory which seeks to explain the relative weakness of the gravitational force [36]. In the ADD model, the observable Universe is restricted to a "brane" with 4-dimensions (including time), and gravitons are free to propagate in a higher dimensional space (called the "bulk"), bringing the Plank scale (M_s) down

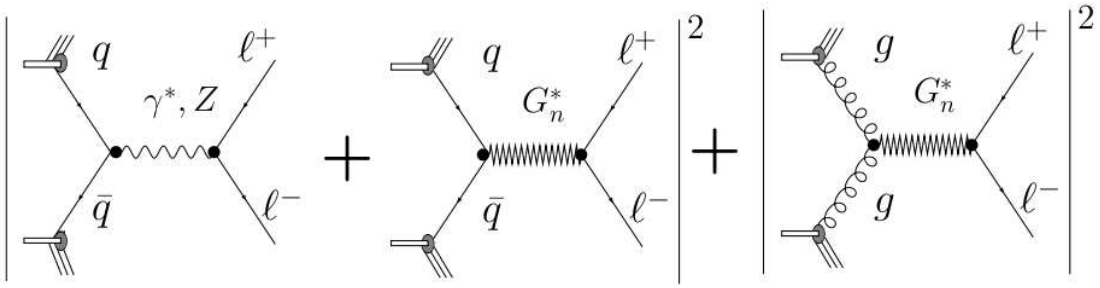

Figure 1.5. Feynman diagrams for enhanced DY production at a hadron collider, considering LEDs.

to $\sim \mathcal{O}$(TeV). The scale M_s is associated to the fundamental Plank scale in the bulk by $M_{Pl}^2 \propto M_s^{n+2} R_n$, with R_n as the characteristic size of the n extra dimensions. Higher-dimensional operators in the model are the analogue of contact interactions, with $\Lambda \equiv M_s$. The deviation from SM production arises through an additional virtual graviton exchange, as can be seen in Fig. 1.5 [37]. Note that besides the cross section terms given in Eq. (1.19), there is also a contribution from initial state gluons. The cross section depends on the formalism describing the virtual graviton exchange relation to the number of extra dimensions (see GRW [38], HLZ [39], and Hewett [40]), but due to the reduction of the Plank scale, all are potentially accessible at the LHC.

1.3.3 Quark and Lepton Compositeness

As previously mentioned, the mass hierarchy of quark/lepton SU(2) doublets remains unaccounted for within the SM. One possible explanation is that quarks and leptons are not fundamental particles but are made of constituent parts [41], often called "preons" in the literature. The preons interact via a new gauge interaction named "metacolor", with properties analogous to pion exchange in the atomic nucleus model. In this scheme, Λ is the metacolor scale beneath which preons are bound to form the SM quarks and leptons.

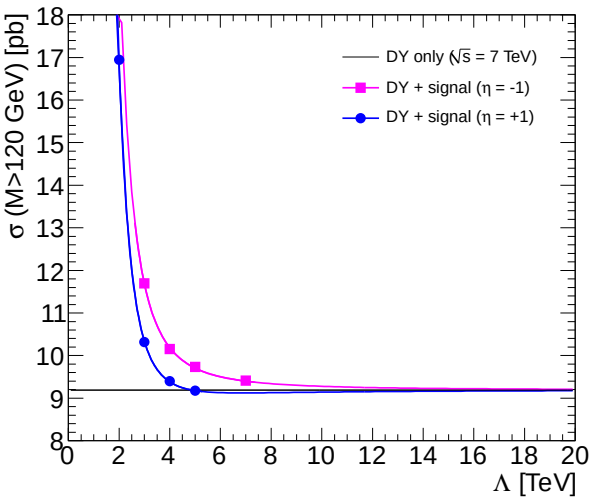

Figure 1.6. Leading-order cross section (for $m_{\mu\mu} > 120$ GeV) in the LLIM as a function of the contact interaction scale Λ.

The Left-left Isoscalar Model (LLIM) of quark compositeness is the benchmark interpretation of a contact interaction used in the analysis presented in this thesis, defined by $\eta_{LL} = \pm 1$ and $\eta_{RR} = \eta_{LR} = 0$. Here, isoscalar refers to the fact that the neutral current does not couple to the analog of weak isospin in the new interaction, and preon flavor-changing neutral currents are not allowed.

Figure 1.6 shows the cross section as a function of Λ for $m_{\mu\mu} > 120$ GeV at $\sqrt{s} = 7$ TeV. Note that as $\Lambda \to \infty$, the cross section approaches the DY value.

1.3.4 Review of Previous Searches

In the extra dimensions model, the combined LEP limit in the Hewett formalism is $\Lambda >$1.12 TeV (95% C.L.) for destructive interference, and $\Lambda >$1.29 TeV (95% C.L.) for constructive interference [42]. Stricter limits have been set by the Tevatron experiments, who have found $\Lambda >$1.27 TeV (95% C.L.) for destructive interference and $\Lambda >$1.43 TeV (95% C.L.) for constructive interference [43]. At both LEP and the Tevatron, the searches were performed in the dielectron channel.

In searches for quark compositeness, the most stringent limit for the $qq\mu\mu$ interaction in the Left-left Isoscalar Model ($\eta_{LL} = \pm 1$, $\eta_{LR} = \eta_{RL} = \eta_{RR} = 0$) is $\Lambda >$ 4.2 TeV (2.9 TeV) for constructive (destructive) interference, at 95% C.L. [44].

1.4 Collider Physics

The parton model of hadrons was proposed by Feynman [45] after an underlying structure in nucleons was observed in electron-nucleon deep inelastic scattering experiments [46]. However, the structure inside the proton is far more complex than the original three-quark (uud) model, especially in the low q^2 limit where the physics becomes non-perturbative. The structure of the proton may be described instead by parton distribution functions (PDFs) $f_a(x)$, which are functions of the probability that a parton a has a fraction x of the proton momentum (Fig. 1.7 [47]). Not only do the valence quark constituents of the proton play a role, but a large fraction of the proton momentum comes from gluons and off-shell (sea) quarks as well[5]. The number of these sea particles depend on the momentum of the proton, and can be approximated by probabilities for the gluons to split into quark-antiquark or gluon pairs and for the quarks to radiate gluons (DGLAP QCD evolution equations [48, 49, 50]). This complicates the calculation of the full production cross section, but luckily the QCD factorization theorem states that a hadron-hadron collision may be separated into two parts: the hard scattering interaction between the two colliding partons and the PDFs for those partons as a function of the momentum transfer q^2 of the interaction [51]. The convolution of the PDF with the hard scattering cross section yields the total cross section observed on a macroscopic scale. For example, the DY cross section (to first order) resulting from proton A colliding with proton B at center of mass energy $\sqrt{s}$ and invariant momentum transfer q^2 is given by:

[5]Incidentally, the *only* way the Drell-Yan process can be produced in proton-proton collisions at the LHC is by utilizing an anti-quark from the sea.

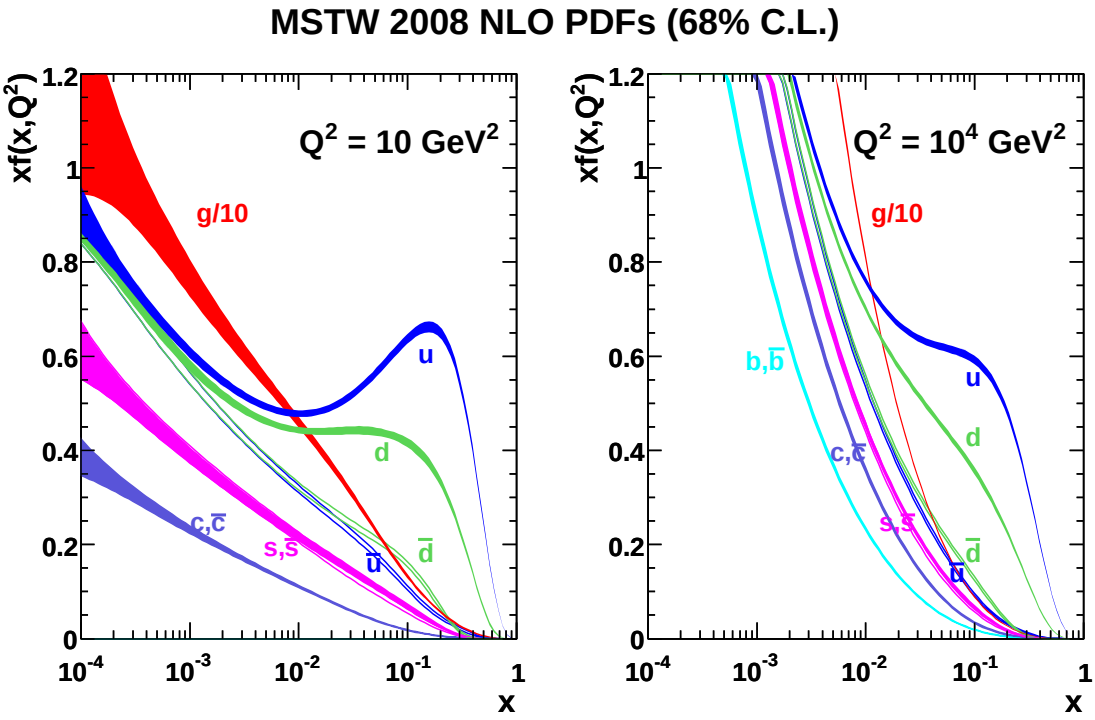

Figure 1.7. Next-to-leading order parton distribution functions of the proton for a momentum transfer of 10 GeV^2 (left) and 1000 GeV^2 (right).

$$\sigma(AB \to \ell^+\ell^- X) = \sum_a \int dx_A dx_B \;\; f_{a/A}(x_A)\; f_{\bar{a}/B}(x_B)\; \sigma_{a\bar{a}\to\ell^+\ell^-}(q^2) \;\; , \qquad (1.20)$$

where $\sigma_{a\bar{a}\to\ell^+\ell^-}$ describes the parton-parton cross section.

The hard scattering between the two partons is not the only interaction which occurs in a proton-proton collision (as denoted by X in the final cross section above). Other processes are listed below:

- *Initial and final state radiation*

  As initial and final state fermions accelerate in the collision, they generally radiate photons or gluons. In the case of DY production at a proton-proton collider, initial state radiation (ISR) of gluons and photons occurs as the incoming quarks

become asymptotically free (see Fig. 1.8), while final state radiation (FSR) includes photons radiated from the leptons produced after the hard scattering.

- *Multiparton interactions*

  There is also the chance that more than one pair of partons may interact within a proton-proton collision. When this occurs, it is known as a "multiparton" interaction (MPI) and should be accounted for when calculating the hadron-hadron interaction cross section. The number of sea quarks in a proton at the LHC is greater than at previous accelerators due to the higher center-of-mass energy of the colliding beams, making them relatively more available to hard scatter in a collision.

- *Remnants, the color field and hadronization*

  The other valence and sea quarks present in the two colliding protons, if not participating in MPIs, will continue on roughly the same longitudinal trajectory. Due to confinement these proton remnants are not free particles, and a color field of gluons forms as the proton breaks apart, growing stronger and stronger until eventually snapping and causing quark-antiquark pairs and gluons to be produced from the vacuum (see Fig. 1.8). In addition, quarks and gluons may radiate more gluons, in turn producing more pairs. As this is a difficult process to calculate at higher order, it can be approximated by a parton shower (PS) algorithm in event generators, which typically assume that the transverse momentum of emitted gluons is small. The quarks bind into color-neutral states and form new hadrons (hadronization), which themselves may be unstable and decay further.

The remnants and other decay products from the parton shower can be detected along with the hard scattering. These other softer QCD processes which form low-energy jets, together with gluons (in the form of jets) and photons emitted in initial

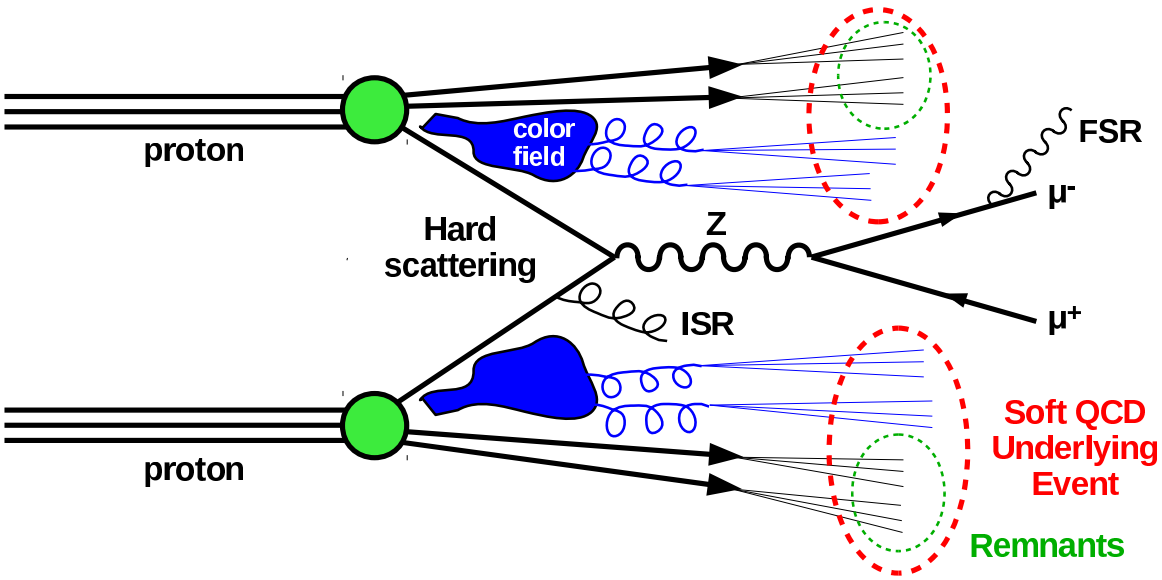

Figure 1.8. Proton-proton collision resulting in a hard scattering, showing the underlying event, initial state radiation (ISR), and final state radiation (FSR).

and final state radiation, are known as the "underlying event". In the detector, the underlying event along with the hard scattering appears as a group of charged tracks originating from the same place, called a "vertex", which makes it possible to discriminate inelastic collisions from other non-collision backgrounds. Processes in a typical hadron collision are illustrated in Fig. 1.8.

ATLAS uses several programs to generate events before they are simulated in the detector. The two main groups which produce PDF sets to be used by event generators at the LHC are MSTW (formerly MRST) [47] and CTEQ [52]. Both of these are capable of describing the proton structure at leading-order (LO), next-to-leading-order (NLO) and next-to-next-to-leading-order (NNLO). The PDFs have been tuned based on data collected from deep inelastic scattering experiments which probe the proton structure as well as on data taken by the Tevatron in proton-antiproton collisions.

Event generators may handle parton showering and hadronization differently. Some details of the programs which were used in this thesis are are highlighted below:

- The PYTHIA [53] event generator package handles all hard scattering at leading-order, as well as computes parton showering and hadronization. For parton showering, it uses a momentum-ordered approach (ie: the hard gluons and photons are emitted with softer and softer momentum as the shower evolves) [54], with SM particles produced at the end of parton showering.

  Hadronization in PYTHIA is done with a string approach. The quarks left after the parton showering are "strung" together to form colorless states, which can either snap and produce more quarks or remain as final underlying event particles. While PYTHIA also handles ISR and FSR, for DY processes at ATLAS, FSR of photons is handled by a separate package PHOTOS [55], which implements all leading-order QED radiative corrections to Z/γ^* decays.

- The HERWIG (Hadron Emission Reactions With Interfering Gluons) package [56] is also a full event generator. The PS evolves in an angle-ordered way, where the gluons and photons with the largest angle (corresponding to a larger transverse momentum) are emitted first. Hadronization in Herwig is handled via a cluster approach, that is, partons produced in the PS "cluster" together into colorless-states which are unstable and then decay into SM particles. In ATLAS HERWIG is often used to model interactions in the underlying event.

- JIMMY [57] is used with the HERWIG package to describe multiparton interactions (also with cluster parton showers). The MPI parton showers from JIMMY are kept separate from the underlying event interactions generated by HERWIG in an event.

- MC@NLO [58] generates hard scatters to NLO accuracy. The kinematic information from the hard scatter is then fed to the HERWIG program.

- HORACE [59], similarly to MC@NLO, generates hard scatters only. In this case, it calculates DY processes including the exact 1-loop electroweak radiative corrections matched with a QED shower.

The specific physics processes which use these programs will be discussed in detail in Chapters 3 and 5.

CHAPTER 2

THE ATLAS EXPERIMENT AT THE LARGE HADRON COLLIDER

This chapter introduces the Large Hadron Collider and the ATLAS detector. Special attention is given to the ATLAS muon spectrometer detector design and reconstruction software in section 2.3, and the expected performance of the muon spectrometer is discussed in section 2.4. Finally, section 2.5 discusses the ATLAS data acquisition system and data quality assessment.

2.1 The Large Hadron Collider

The Large Hadron Collider (LHC) [60, 61] is a proton-proton (pp) and lead-lead (Pb-Pb) collider located at CERN, just outside of Geneva, Switzerland. The main part of the machine is located $\sim$100 m underground in a circular tunnel $\sim$27 km in circumference which used to house the Large Electron-Positron (LEP) collider [62]. The superconducting magnet system is held at a temperature of 4.5K using superfluid helium, and is constructed of many different types of magnets, including dipoles which keep the beam of hadrons in a circular orbit and quadrupoles which focus the beam at the interaction points at the center of each detector. Though the design energy is 7 TeV per beam to give a 14 TeV center of mass energy, the LHC is currently running at half the nominal energy at 3.5 TeV per beam.

The full acceleration process occurs within stages in the CERN accelerator complex (Fig. 2.1) [63]. A duoplasmatron [64] produces protons by stripping electrons away from hydrogen atoms. The protons are then injected from the Linac2 to the

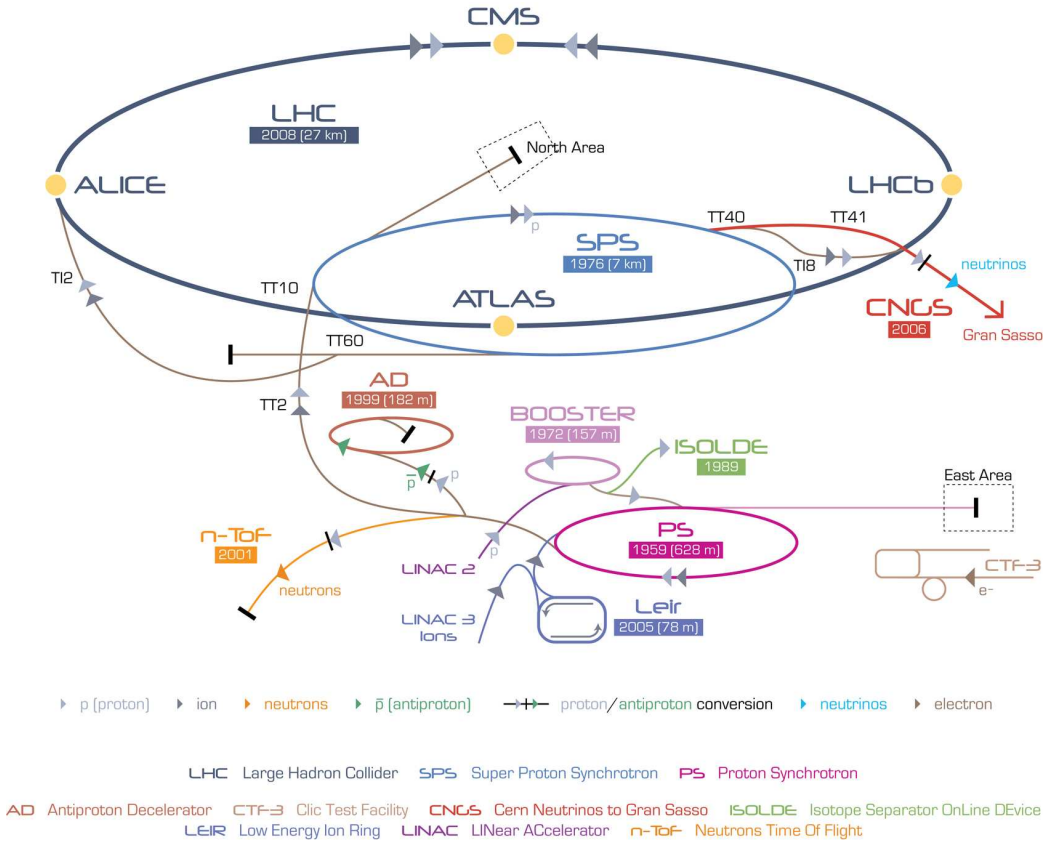

Figure 2.1. The CERN accelerator complex.

Proton Synchrotron booster at an energy of 50 MeV, which then accelerates the protons to 1.4 GeV. From there, the Proton Synchrotron ring receives the protons and accelerates the beam to 25 GeV, injecting it into the Super Proton Synchrotron (SPS). This accelerator, where the experiments UA1 and UA2 first discovered the W and Z bosons, increases the energy of the protons further to 450 GeV before finally passing the beam to the LHC.

The beams are actually made of discrete packets of protons called "bunches". The LHC ring can store up to 2808 bunches per beam at a given time. At nominal running conditions, these bunches are 25 ns apart and up to 40 collisions may occur within any given bunch crossing at the center of the detectors. This corresponds to a design luminosity of 10^{34} cm^{-2}s^{-1}.

2.2 The ATLAS Detector

The ATLAS Experiment [65] is one of two general-purpose detectors on the LHC ring and was designed to measure an array of particles, including electrons, photons, jets, B-mesons, muons and neutrinos (via missing transverse energy), all of which rely on the capability of the detector to reconstruct these objects with precision. The physics program at ATLAS includes a wide range of subjects. While one of the main physics goals is the search for the elusive Higgs boson, the high luminosity at the LHC as well as the possibility to reach the TeV energy regime also provides an opportunity to perform high precision tests of EW and QCD interactions, study the top quark, and verify SM predictions at the EW scale. In addition, the search for physics beyond the SM is a large component of research performed at the ATLAS detector. The detector was built to identify and measure particles with high precision in a large energy range from a few GeV to a few TeV with a large geometrical acceptance. High-momentum particles were especially considered in the design of ATLAS in anticipation of new physics discoveries at the TeV scale.

When the design beam energy is reached, the total proton-proton cross section will be roughly 80 mb and the rate of events in ATLAS will be extremely high. In addition, the high luminosity produced by the LHC will deliver 10^9 collisions/s, which will dwarf the number of interesting new physics events. This large rate (and thus extreme particle fluxes) required the design of the detector to incorporate a balance between a high granularity of detector elements and fast electronics with many read out channels. In addition, because the rate will be too high to process and save every event, a multi-layer trigger system was needed in order to filter the interesting events and save them for physics analyses.

2.2.1 Layout of the Detector

The detector is cylindrically shaped, with the origin situated at the center of the detector where the nominal interaction point lies. A right-handed coordinate system is defined with the x-axis pointing horizontally from the origin to the center of the LHC ring, the y-axis normal to the ground, and the z-axis along the beam pipe. The profile of the ATLAS detector is roughly circular in the $x-y$ plane. The "A-side" of the detector is the region defined by $z>0$ and the "C-side" is the region defined by $z<0$. The azimuthal angle ϕ is measured in the $x-y$ plane around the beam axis, starting from the positive x-axis. The polar angle θ is measured from the positive z-axis, and the radius R_z is defined in the $y-z$ plane by the relation $z = R_z \cos\theta$. For convenience, the term "barrel" is used for detector components which are parallel to the beam in the central region of the detector, while the "endcaps" refer to those components which are perpendicular to the beam on either end of the barrel region.

In pp collisions, it is impossible to know the longitudinal momentum of the parton-parton interaction relative to the rest-frame, as each parton carries an unknown fraction of the proton's momentum. Thus it is convenient to define a Lorentz-invariant variable called rapidity:

$$y = \frac{1}{2} \ln \frac{E + p_z}{E - p_z},$$

where E and p_z are components of the particle 4-momentum. In the limit that the rest energy of the particle is much smaller than its total energy, this can be approximated as the pseudorapidity:

$$\eta = -\ln \tan \frac{\theta}{2}.$$

The Lorentz-boost invariant variables p_T (transverse momentum), ϕ and η cover all of phase space and are used to describe the kinematics of pp collisions.

Another useful variable is the separation between two particles in $\eta - \phi$ space:

$$dR = \sqrt{(\eta_1 - \eta_2)^2 + (\phi_1 - \phi_2)^2}.$$

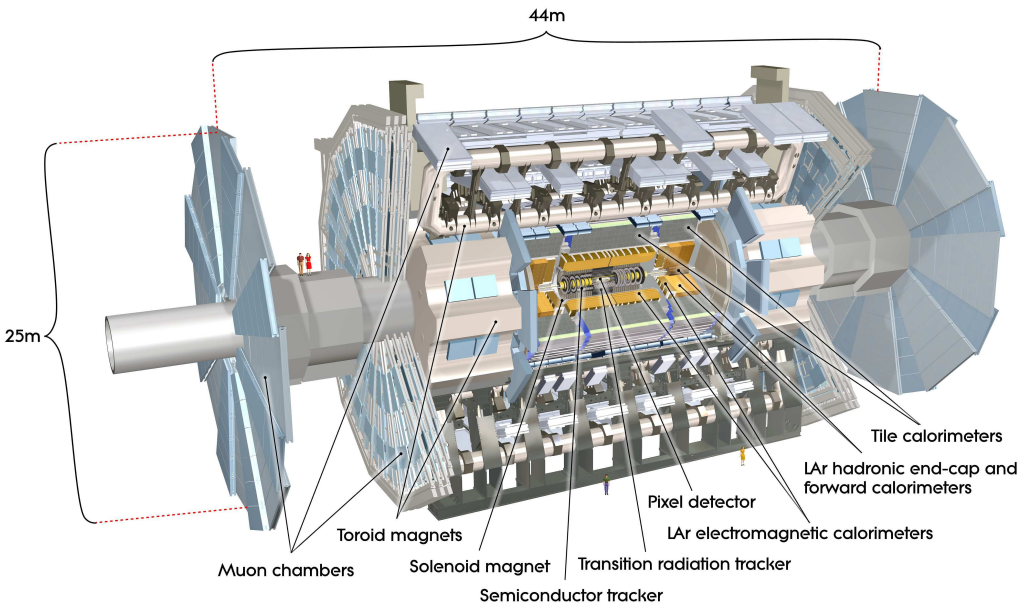

Figure 2.2. The ATLAS Detector.

This is often used to describe the width of a cone around a given particle trajectory.

ATLAS is comprised of multiple subdetectors, each with the capacity to withstand huge particle fluxes (Fig. 2.2). Starting closest to the beam pipe, an inner detector measures charged tracks with high granularity which maximizes charged-particle momentum resolution and efficiency, making it extremely sensitive not only to tracks originating from the primary collision (or "primary vertex") but also to secondary vertexes for b- and τ-tagging as well. Continuing radially outwards, an electromagnetic calorimeter measures and identifies electrons and photons while a hadronic calorimeter makes accurate jet energy and missing transverse energy (missing E_T) measurements. The inner detector and calorimeter systems will be discussed further in sections 2.2.2 and 2.2.3. Finally, a muon spectrometer provides identification, momentum and charge measurement of muons over a large momentum range. Because of its importance for the analyses presented in this thesis, the muon spectrometer will be described in greater detail in section 2.3.

2.2.2 Inner Detector

At high luminosity, thousands of charged tracks from hadron remnants are produced in the detector. In order to properly reconstruct these tracks, an inner detector is located close to the beam pipe. Surrounding the ID is a solenoid magnet providing a 2 T field, which causes charged particles to bend in the azimuthal direction. The ID accurately measures track momentum, performs reconstruction of vertices and discriminates between electrons and other charged particles (such as pions) with high sensor element granularity. It is also crucial for making precision measurements of the track impact parameter variables z_0 and d_0, the longitudinal and transverse distances from the vertex, respectively. The ID consists of three main technologies: a pixel detector, a silicon tracker, and a transition radiation tracker (Fig. 2.3).

The pixel detector [66] is comprised of silicon pixels mounted on 1744 pixel sensors with 46,080 read-out channels per sensor. Each pixel is 50 μm $\times$ 400 μm in size (with some 50 μm $\times$ 600 μm). The sensors are arranged in three layers in the barrel and two sets of 3 disks in the endcaps on each end of the barrel region. The inner-most layer, called the "B-layer", is situated 5 cm from the beam and is important for discriminating between tracks from the primary interaction and secondary processes. The silicon tracker (SCT) [67] consists of layers of silicon strips with a pitch of 80 μm and has a resolution of approximately 17 μm in the bending plane. The SCT is able to measure both the η and ϕ coordinates by daisy-chaining two sensors together with 40 mrad angle between them. Together with the pixel detector, the silicon detectors extend to $|\eta| < 2.5$.

The silicon detectors are essential for reconstruction of vertices (see Fig. 2.4). In order to select a primary vertex, tracks in the ID are required to have $p_T > 150$ MeV, $|d_0| < 4$ mm, an error in the z_0 measurement less than 5 mm, an error in the d_0 measurement less than 10 mm, at least 4 hits in the SCT detector alone and at least 6 hits in the pixel and SCT detectors combined [68].

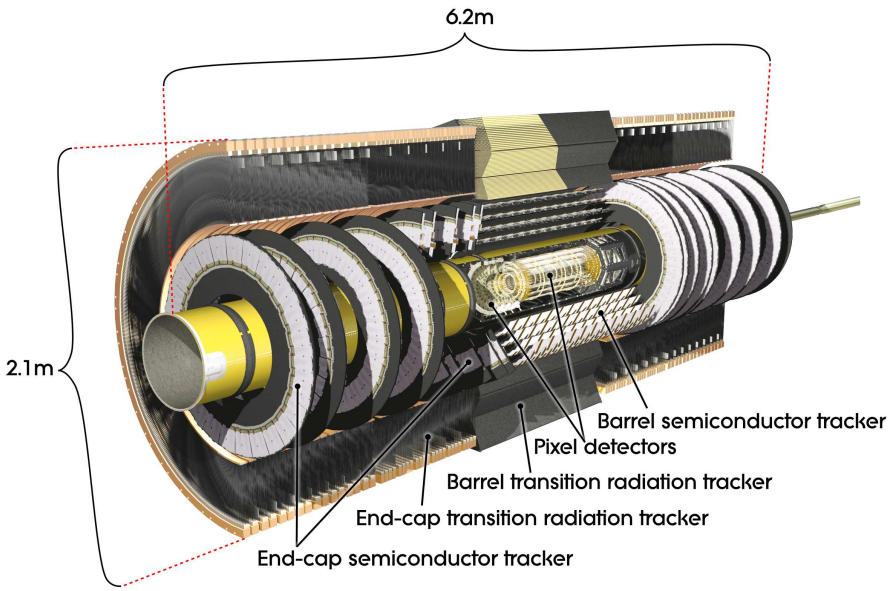

Figure 2.3. The ATLAS Inner Detector.

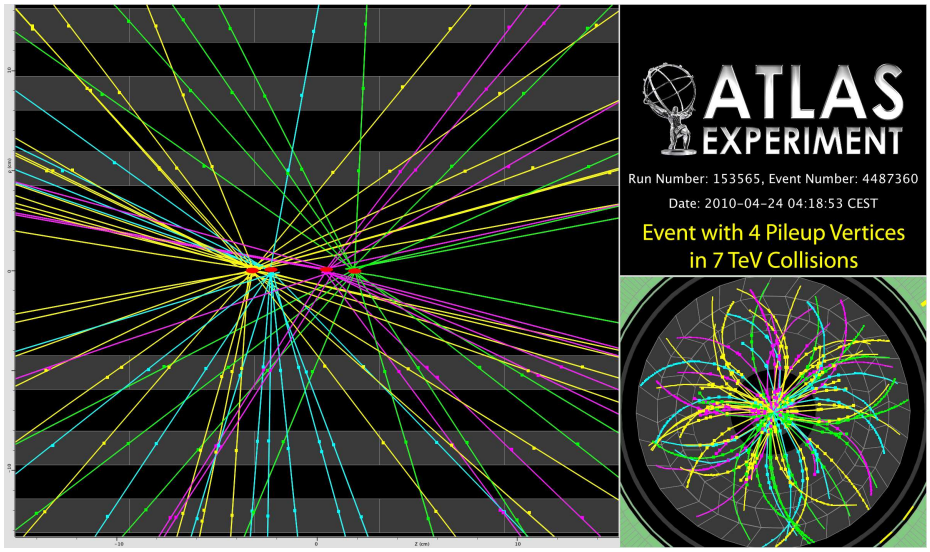

Figure 2.4. Pileup event with four primary vertices.

The transition radiation tracker (TRT) [69, 70] is the largest subdetector in the ID. The TRT contains layers of 4mm-diameter straw tubes which are filled with an $ArCO_2CF_4$ gas mixture, each containing a gold-plated anode wire held at a 1530 V potential. As a charged track passes through a straw, it ionizes the gas causing electrons to drift to the anode wire to form a signal. There are more than 350,000 read-out channels, with a resolution of $\sim$ 130 μm per straw. The straw tubes are interleaved with transition radiation (TR) material, which causes a charged track to emit photons which then produce electron-positron pairs also ionizing the gas inside the straws. This energy loss due to radiation in the TR material differs as a function of particle mass, thus allowing a discrimination between electrons and heavier particles, such as charged mesons. The TRT acceptance extends to $|\eta| < 2.0$.

2.2.3 Calorimetry

The electrons produced in hard scatters are energetic enough that upon encountering dense material, they lose most energy via bremsstrahlung radiation. An emitted photon (or a photon from the hard scattering) can produce an electron-positron pair, each of which can in turn radiate more photons. This cascading process appears as a shower of EM particles in the detector. Similarly, quarks also appear as a shower of particles, called "jets", which are created through the hadronization process. By fully absorbing the EM showers/jets, the energy measured in a calorimeter is related to the total energy of the primary particle of interest.

The ATLAS calorimeter system is comprised of two sampling calorimeters: an electromagnetic and a hadronic calorimeter (Fig. 2.5). Sampling calorimeters have active material which measures energy deposits layered with a denser material called an absorber, which is where most showering interactions occur. The benefit of a sampling calorimeter (as opposed to a homogeneous calorimeter made only of active

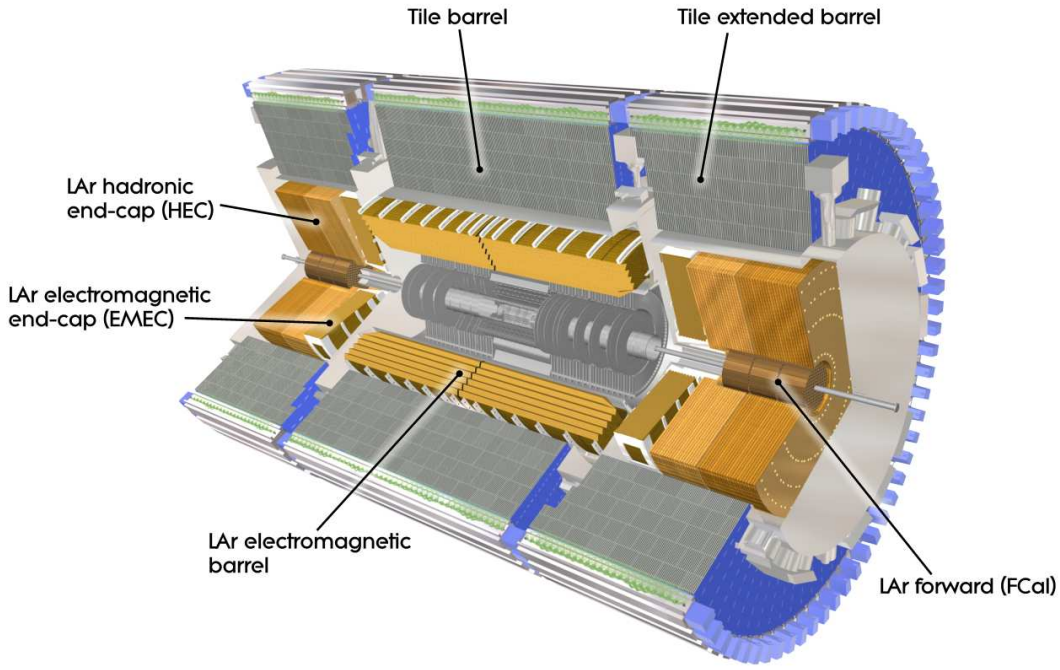

Figure 2.5. The ATLAS Calorimetry system.

material) is that it may be smaller, as a shower or jet has a shorter radiation length through the passive material.

The electromagnetic calorimeter (ECAL) uses a lead absorber and a liquid argon (LAr) active medium to sample energy deposits from electrons, photons and jets. The barrel portion of the ECAL extends to $|\eta| < 1.475$ and endcaps in the region $1.375 < |\eta| < 3.2$. The lead absorbers and active regions are layered in an accordion shape in order to have full azimuthal coverage (Fig 2.6) and capture electromagnetic showers without loss of acceptance between read out electrodes.

However, the ECAL cannot completely contain highly energetic hadronic showers. The hadronic calorimeter, which surrounds the ECAL, measures jet energy with polystyrene scintillating tiles in the barrel (TileCal) and liquid argon in the endcaps. In the TileCal, which is composed of barrel sections in the $|\eta| < 1.0$ and $0.8 < |\eta| < 1.7$ regions, scintillation light is converted into a signal by photomultiplier tubes. The

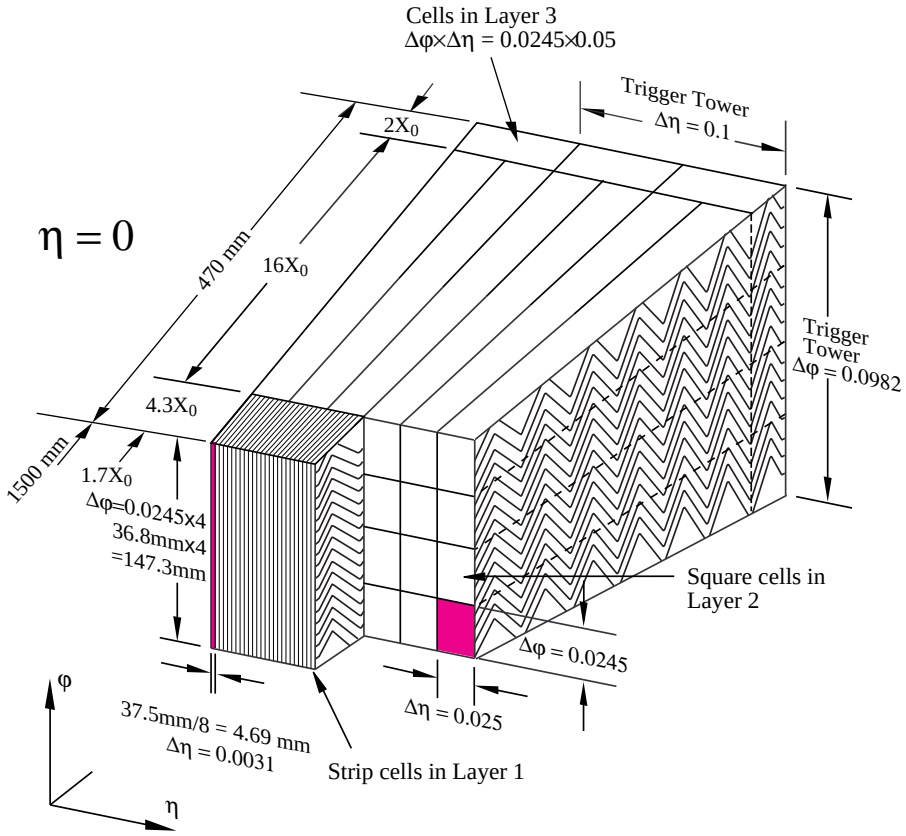

Figure 2.6. Liquid argon electromagnetic calorimeter layout for a module in the barrel.

absorbers in the TileCal are steel plates. The hadronic endcap calorimeter (HEC) was built with copper plates interleaved with LAr active medium, and extends in the range $1.5 < |\eta| < 3.2$, overlapping with both the TileCal and the forward calorimeter (FCal). The FCal provides further calorimeter coverage to $|\eta| < 4.9$ and absorbs much of the forward beam remnants reducing the high-radiation occupancy in the muon spectrometer.

2.3 The ATLAS Muon Spectrometer

The ATLAS muon spectrometer (MS) is situated in an air-core toroidal field which deflects the muon tracks in the R_z plane (Fig. 2.7). The MS is arranged in

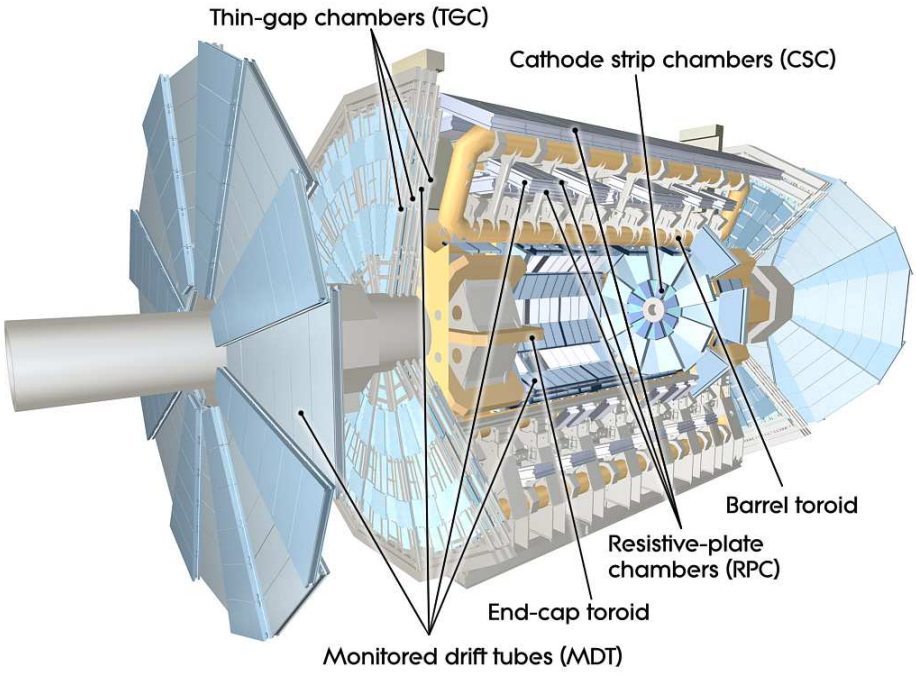

Figure 2.7. The ATLAS Muon Spectrometer.

three cylindrical tiers of chambers labeled the inner (I) middle (M) and outer (O) stations. The barrel region extends to $|\eta| < 1.05$ with an outer diameter of 20 meters. Three discs in each of the endcap regions lay within $1.05 < |\eta| < 2.7$. Together, the barrel and endcap muon chambers span the full length of the detector.

The magnetic field is provided by eight superconducting toroid magnets in the the barrel region and eight in each of the endcap regions, where the endcap toroids are rotated 22.5° in ϕ with respect to those in the barrel (Fig. 2.8). The toroids provide a magnetic field bending power $\int B \cdot d\ell$ in the range from 1.5 Tm to 5.5 Tm in the barrel and 1 Tm to 7.5 Tm in the endcaps. Because of where the endcap toroids are situated, there is only field strength between the inner and middle MS layers in the endcap region. Figure 2.9 shows $\int B \cdot d\ell$ as a function of η and the field distribution in the toroid transition region ($1.4 < |\eta| < 1.6$) where the magnetic field bending power is reduced [71].

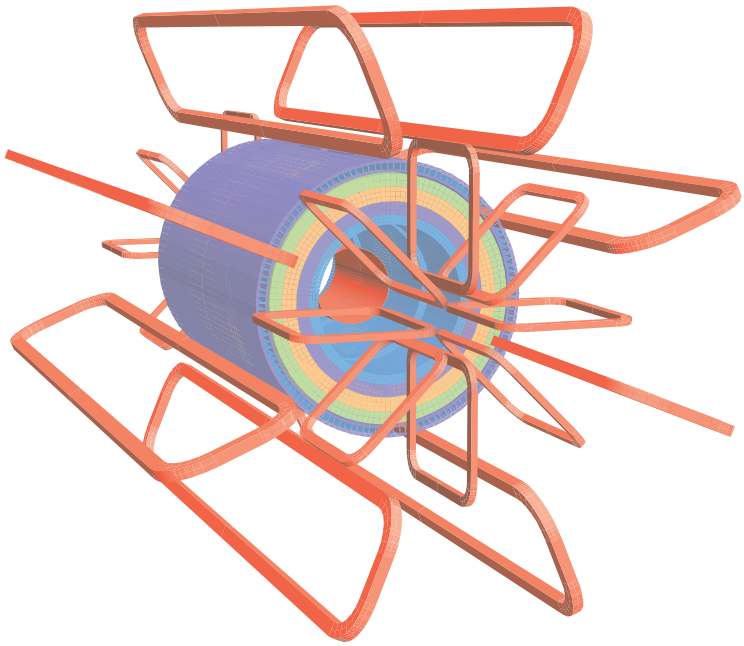

Figure 2.8. The ATLAS Magnet system, showing 8 toroids in the barrel and the 8 toroids in each of the endcaps.

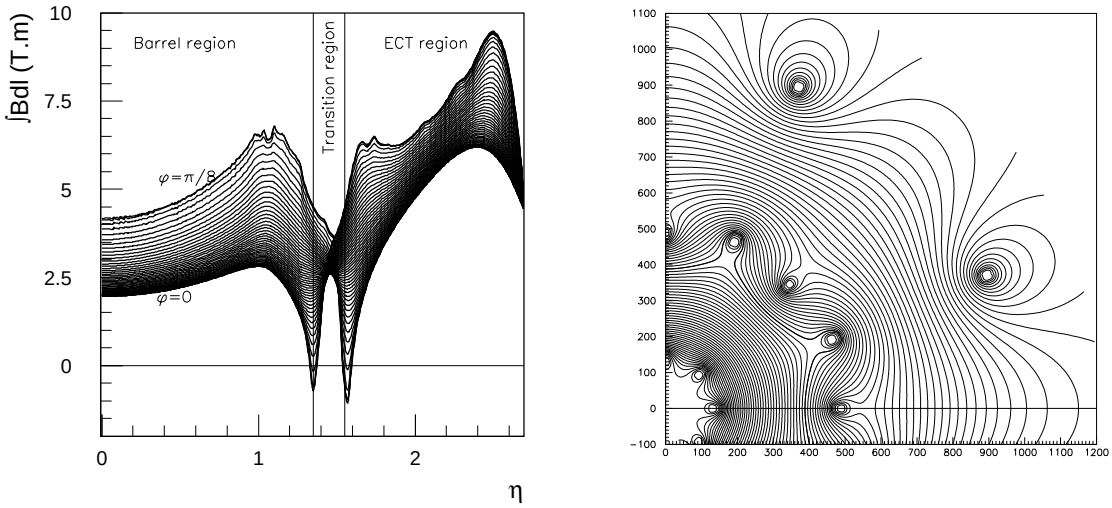

Figure 2.9. Magnetic field bending power $\int B \cdot d\ell$ (left) and field distribution in the barrel-endcap transition region ($1.4 < |\eta| < 1.6$) with 0.1 Tm separating the field lines (left).

Monitored drift tube (MDT) chambers measure the muon track in each station in the bending plane, having a large acceptance extending to $|\eta| < 2.7$. Cathode strip chambers (CSCs) are precision chambers located on each of the inner discs of the MS endcaps in the region $2.0 < |\eta| < 2.7$ where there is a much higher track occupancy closer to the interaction point. Resistive plate chambers (RPCs) and thin gap chambers (TGCs) located in the barrel and endcap regions, respectively, are used to trigger muon events and also measure the second (ϕ) coordinate. Details of these four technologies are below.

Monitored Drift Tubes -

There are ∼1150 MDT chambers in ATLAS, consisting of a total of ∼354,000 read-out channels. Aluminum drift tubes 3 cm in diameter contain a 50 μm-diameter tungsten-rhenium wire running down the center held at a 3080 V potential. The chambers are filled with a 7% Argon, 93% CO_2 gas mixture kept at a pressure of 3 bars. Each MDT station consists of two multi-layers (MLs) of drift tubes[1], with four MDT layers in each ML for the inner station, and three layers in each ML for the middle and outer stations.

The electronics on an MDT chamber include a chamber service module (CSM), which collects data from up to 18 mezzanine cards, each of which services 24 drift tubes. As a muon traverses a tube, it ionizes the gas inside causing electrons to drift to the central wire (Fig. 2.10). An amplifier-shaper-discriminator (ASD) chip located on the mezzanine card converts the signal from the wire to a voltage pulse. A time-to-digital converter (TDC) chip also on the mezzanine card measures the time of the leading and trailing edge of the discriminator output. This time can be turned into a radius via a space-time (r-t) relation in order to determine the transverse distance

[1]There are a few exceptions, where the chambers only have one ML, notably chambers in the barrel-endcap transition region (known as "BIS8" chambers) and the BEE chambers.

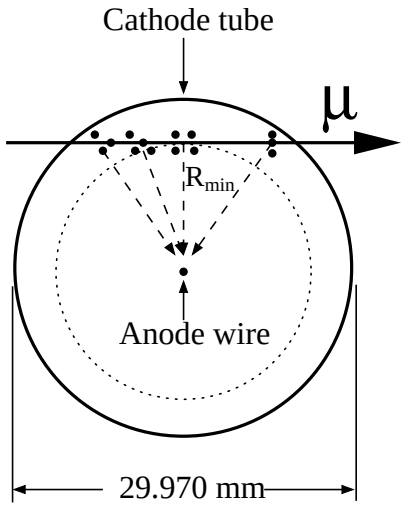

Figure 2.10. Schematic of a muon drift tube.

r_{drift} between the path of the muon in the tube and the central wire. Figure 2.11 shows an example of an MDT chamber TDC time spectrum and an r-t relation determined from cosmic muon studies. Circles of radius r_{drift}, or "hits", are used in offline software reconstruction to measure where the muon track had passed by a fitting a line (called a "segment") tangential to drift circles in each ML. The nominal hit resolution in each tube layer is $\sim$80 μm.

The MDT chambers are arranged in 16 overlapping large and small sectors in ϕ, where the large chambers are located between the barrel toroid coils (Fig. 2.12). The naming convention for the chambers uses three letters XYZ:

- X: "B" or "E", representing barrel or endcap.
- Y: "I", "M", "O" or "E" representing inner, middle, outer or extra chambers. The "extra" chambers are located in the barrel-endcap transition region, with EE chambers perpendicular to the beam line and BEE chambers located on the chassis containing the endcap toroids parallel to the beam line.

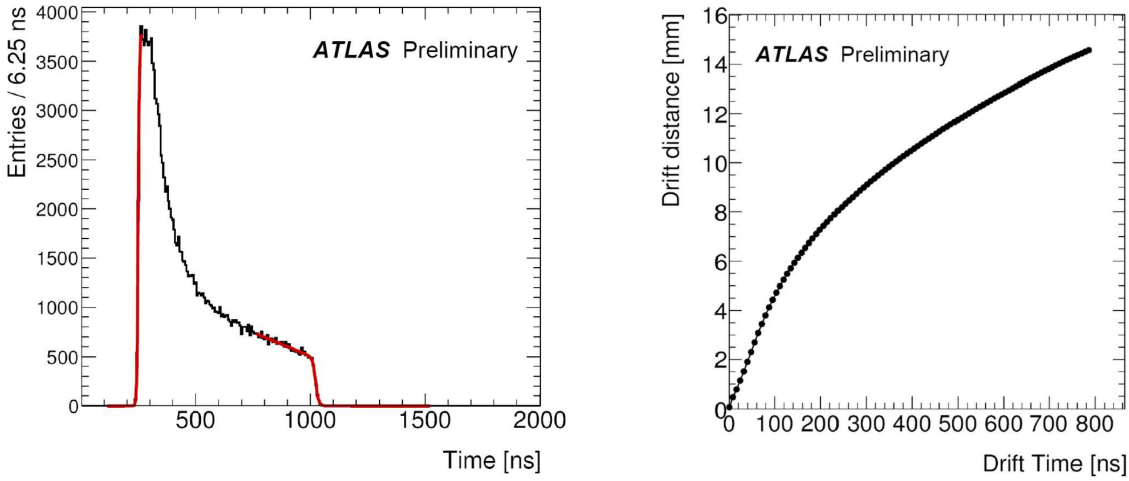

Figure 2.11. A typical MDT drift time spectrum (left) and space-time (r-t) relationship for MDT chambers (right).

- Z: "L" or "S" representing a large or small sector. In addition, there are modified chambers in the barrel region near the feet of the detector, denoted with "M" or "R" in the inner layer, "G" in the outer layer, or "F" in the middle and outer layers.

In addition, each chamber is associated to either the A or C side of the detector, and two numbers define the sector in ϕ (Fig. 2.12) and chamber position in η (Fig. 2.13). So for example, the EML5C13 chamber is a large-sector chamber in the middle layer of the endcap on side C, and is the 5^{th} chamber away from the interaction point located in sector 13.

Cathode Strip Chambers -

In the far-forward region of the MS and close to the interaction point (IP), the particle flux is too high for drift tube chambers which can only handle counting rates of about 150 Hz/cm^2. CSCs are placed 7 m from the center of the detector in the inner layer of each of the MS endcaps and can handle rates up to 1000 Hz/cm^2. There are 16 CSCs in each endcap, and similarly to the MDT chambers, are segmented

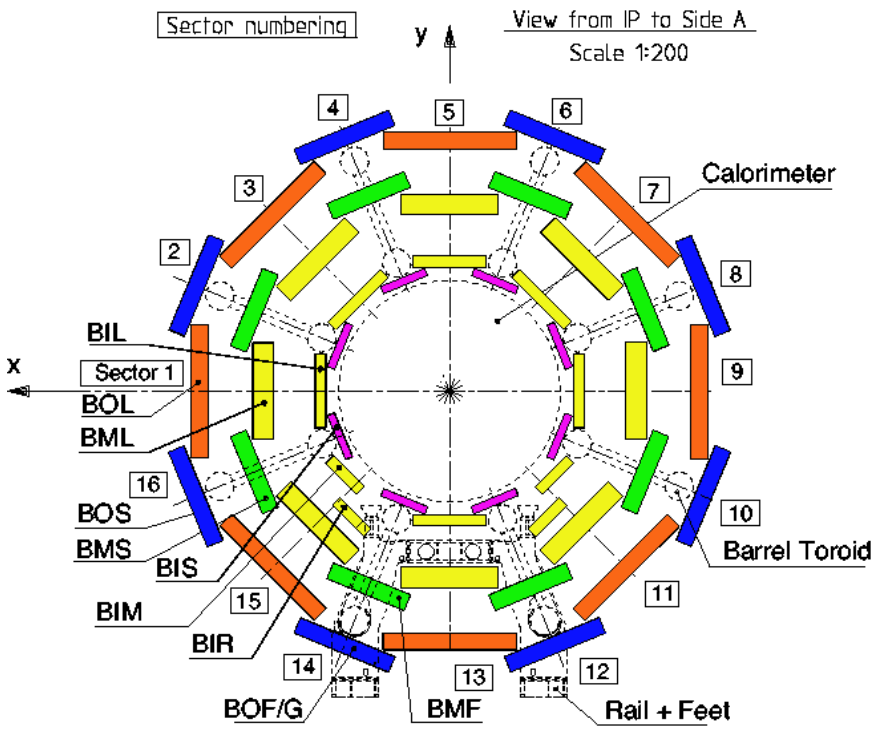

Figure 2.12. Muon chamber sectors, showing the naming convention of barrel chambers.

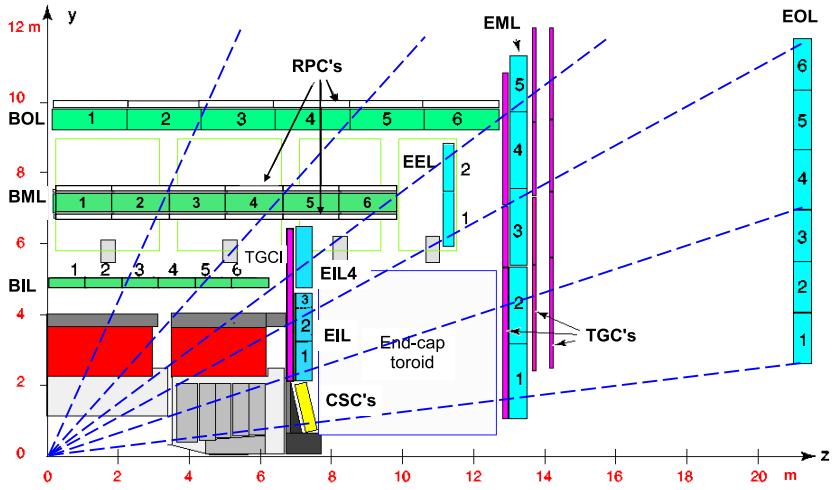

Figure 2.13. Muon chambers in η, showing the barrel and endcap regions and naming conventions for the chambers.

into large and small sectors in ϕ. The chambers are inclined 7° with respect to the endcap MDT chambers (which are perpendicular to the beam pipe) in order to ensure that particles coming from the interaction point are entering the chambers in an approximately perpendicular direction, allowing for better spatial resolution.

Each chamber consists of 4×2 alternating layers of anode wires and cathode strips and are filled with a gas mixture $ArCO_2CF_4$. A muon track traversing a CSC ionizes the gas and causes an avalanche of electrons around anode wires held at a potential of 1900 V, which induces a charge distribution on the cathode strips. The cathode strips are spaced with a pitch of 5.31 mm and 5.56 mm in the large and small chambers respectively, and can measure muons with a nominal spatial resolution of 60 μm in the bending plane. The CSCs also measure the second coordinate ϕ, but with coarser granularity, having a nominal resolution of 5 mm.

Resistive Plate Chambers -

The RPC trigger system is located in the barrel region $|\eta| < 1.05$. Two layers are mounted on the inside and outside of the middle MDT stations, and a third layer is positioned on the outer MDT stations (either on the outside of the stations in the large sectors or on the inside in the small sectors). Because of where they are located, the naming scheme for the RPCs is the same as that for the MDT barrel chambers. There are two RPC units in each chamber, where a unit consists of two resistive plates kept at a 2 mm separation with an electric field of 4.9 kV/mm between them. Each chamber contains a gas mixture of $C_2H_2F_4$/Iso-C_4H_10/SF_6. As a muon passes through, it ionizes the gas and an avalanche of ionization electrons drift to the anode plate producing an avalanche of electrons in its vicinity. This avalanche becomes the signal read out by the chamber electronics. The RPCs measure the second coordinate ϕ as well as the z coordinate with a lower granularity than the precision chambers (10 mm spatial resolution in both the *phi* and z directions). However, the

electron avalanche signal full-width-half-maximum of 5 ns with an intrinsic time jitter of $\leq$1.5 ns makes these chambers optimally designed to trigger on muon events, associating muon signals to bunch crossings which are 25 ns apart.

Thin-Gap Chambers -

The TGC system, forming circular discs, is located in the endcap region $1.05 < |\eta| < 2.4$. One TGC disc with two detector layers is located on the inside inner endcap wheel, and seven detector layers are located in three discs on the middle MDT wheel.

The TGC units, similarly to the CSC design, are multi-wire proportional chambers which contain anode wires that measure the muon in the bending plane and radial strips that measure the ϕ coordinate. The strips are arranged in such a way as to provide a granularity in the ϕ direction of 2 to 3 mrad, corresponding to a nominal spatial resolution of 3 to 7 mm. The anode wire pitch in the chambers is 1.8 mm, giving a nominal spacial resolution in the radial direction of 2 to 6 mm. The TGCs are filled with a CO_2/n-pentane gas mixture and operate with a gas gain of approximately 3×10^5. A large electric field surrounding the wires held at a 2900 V potential, along with their granularity, makes it possible to measure the muon signal with excellent time resolution, triggering the signal within one bunch crossing.

2.3.1 Muon Tracking Software

The Athena software framework, based on the Gaudi architecture [72], is used for event simulation, trigger, reconstruction and physics analysis tools at ATLAS. In particular, muons are identified through measurements in both the ID and MS and reconstructed with two main software chains [73]. These are described below:

The Staco (STAtistical COmbination) collection contains the muon candidates identified and reconstructed by three algorithms:

- The **MuonBoy** algorithm uses precision hit information to create segments in MS stations and fits a muon track to them within a region of activity. Here, a region of activity is determined using both first- and second-coordinate hit patterns in the trigger chambers or CSCs, thus requiring a ϕ hit in the reconstruction of the track. This track is then extrapolated back to the primary vertex, taking energy loss in the calorimeter into account. Track parameters (q/p_T, η, ϕ, z_0 and d_0) are expressed at the primary vertex.

- A **Staco Combined** muon is formed by combining the MuonBoy track with an ID track. Here, the combined track parameters are computed by taking the statistical average between track parameters for pairs of MS and ID tracks. The match-χ^2 of the combined track is given by

$$\chi^2 = (P_1 - P_2)^T (C_1^{-1} + C_2^{-1})^{-1} (P_1 - P_2), \tag{2.1}$$

  where P_1 and P_2 are the track parameter vectors, and C_1 and C_2 are the covariance matrices of the track parameters for the ID and MS, respectively. For more than one ID track associated to an MS track meeting a minimum match-χ^2 requirement, the pair with the lowest match-χ^2 is kept as a combined muon candidate.

- The **MuTag** algorithm begins with ID tracks and associates MuonBoy segments to them. These "tagged" muons are formed only for ID tracks which were not combined with full MuonBoy tracks, and are able to recover muons in η regions where there are less than three MS stations.

The Muid (MUon-ID) muon collection consists of five algorithms:

- The **MOORE** (Muon Object Oriented REconstruction) reconstructs standalone muon tracks by using hit information in the MS to create segments identified

within a global road using all MS subdetectors. The track parameters of the track-fit to these segments are expressed at the entrance of the MS.

- The **Muid Standalone** (MuidSA) algorithm expresses the MOORE tracks at the vertex, taking energy loss in the calorimeter into account, and is analogous to MuonBoy muons in the Staco collection.

- **Muid Combined** muons are formed by matching MuidSA tracks with tracks in the ID and refitting a combined track using the full hit information in the ID and MS.

- **MuGirl** muons are created by starting in the ID and searching for segments in the MS. The tracks are then formed either by refitting using the full hit information from both the ID and MS or, if a combined muon is not possible, creating a a "tagged" muon in which an ID track is associated to a muon segment.

- The **MuTagIMO** (MUon TAGged Inner-Middle-Outer) algorithm extrapolates ID tracks to the MS and searches for MOORE segments, creating a tagged muon.

The most important track parameter measured by the reconstruction algorithm is the muon momentum. The momentum p of a muon with charge q in a magnetic field B traversing an arc length L is inversely proportional to the arc depth, also called the sagitta s:

$$p \propto \frac{q \cdot B \cdot L^2}{s}. \tag{2.2}$$

The three station layout of the MS makes it possible to measure the sagitta with high precision (Fig. 2.14).

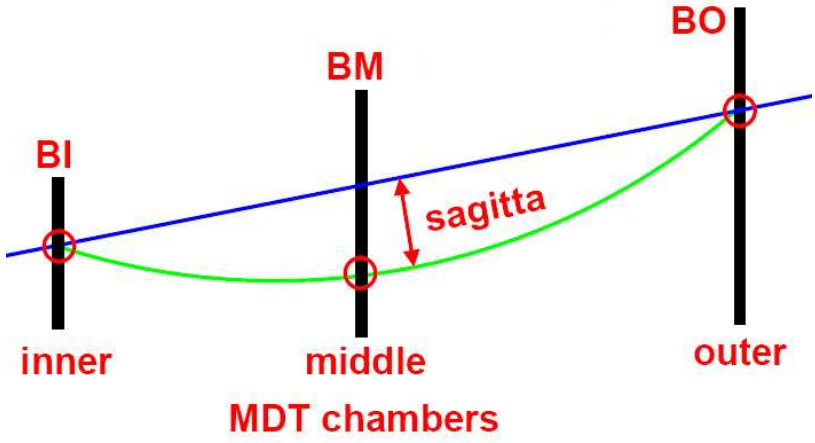

Figure 2.14. Diagram of MS track sagitta measurement in three MDT barrel stations. In the endcap, the muon sagitta is measured only between the inner and middle stations where there is a magnetic field.

2.3.2 Alignment and Calibration

The track position resolution requirements within any given precision chamber have been met in construction, but the position of the chambers in the cavern with respect to each other is only known to roughly 5 mm. In order to determine their position with more accuracy and achieve the design resolution, an optical alignment system has been installed. The position of some chambers are not measured with optical alignment sensors, such as the BEE and BIS8 chambers, as well as the small sector chambers in the barrel, and so muon tracks themselves must be used for alignment. Muon tracks are also needed for globally aligning the large and small sectors in the barrel with respect to each other, and for aligning the barrel chambers with respect to the endcap.

Because the track position is determined from r-t relations, the measured resolution is also affected by shifts in these functions which can occur due to various issues:

- The anode wire sagging under the gravitational force.

- Wire "aging", which refers to buildup of impurities on the anode wire.
- Impurities in the gas.
- Temperature fluctuations.
- Delays due to read out electronics and cables.
- Non-uniformity of the magnetic field within the chamber.

The calibration procedure [74, 75] seeks to correct for these effects. For each MDT tube, the calibration algorithms compute the time offset for charge to reach the anode wire (the leading edge of the TDC spectrum), the mean and width of the distribution of charges (via counts measured by a Wilkinson analog-to-digital converter as part of the ASD on each mezzanine card), and the position along the wire measured by the trigger chamber system. Using an iterative process of measuring muon track segments and refitting them to minimize the residuals of track segment fits (called "autocalibration"), the MDT r-t relation can be found with an accuracy up to about 20 μm. The calibration parameters used in offline reconstruction are returned within 36 hours from the end of an LHC fill.

2.4 Expected Performance of the Muon Spectrometer

The measured efficiency and resolution of the MS varies in different regions of acceptance due to differences in geometry, magnetic field bending power, number of stations, and distributions of inactive material spread throughout the detector [76]. Figure 2.15 shows MDT regions in $\eta - \phi$ space, separated by differences in geometry.

The muon momentum resolution depends on several factors, such as chamber misalignment, muon energy-loss fluctuations and multiple scattering (Fig. 2.16). The design resolution of the MS is $\Delta p_T/p_T = 10\%$ for a $p_T = 1$ TeV muon over 5 meters (Fig. 2.17), which corresponds to a 50 μm sagitta precision in both the barrel and

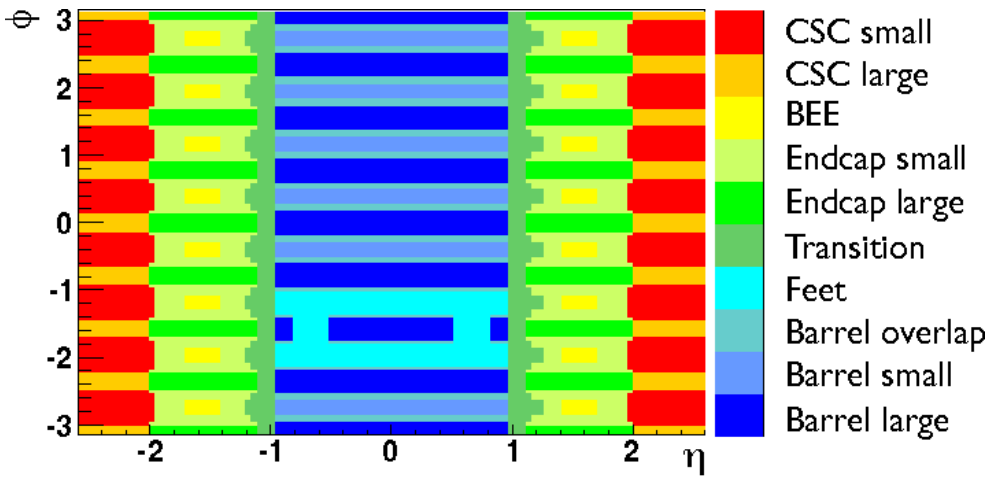

Figure 2.15. Muon spectrometer detector regions.

endcap regions. At high momentum, as the tracks become almost straight, uncertainties in wire resolution and chamber alignment become the dominant contributions to resolution.

Additionally, in order to perform accurate missing E_T measurements and find new particles decaying into muons, the MS needs to reconstruct muons with as high efficiency as possible. For searches involving high-mass dimuons, radiative losses become the dominant energy loss mechanism for muons with p_T above 300 GeV (Fig. 2.18) [44], and the impact of showers in the MS resulting from muons undergoing bremsstrahlung radiation needs to be considered. The presence of showers from bremsstrahlung photons can become an issue for pattern recognition in the MS, as wrongly associated hits from these showers can cause a mis-measurement of track parameters. Extreme showering can often lead to one of two effects: the pattern recognition in the MS fails due to the complexity and extent of the shower and no track is reconstructed; or one or more hits from a shower particle is wrongly associated with the muon track resulting in mis-measured MS track parameters and a failure in the matching between ID and MS tracks. Shower particles causing a mis-measurement of the phi parameter (and thus, an incorrect measurement of the

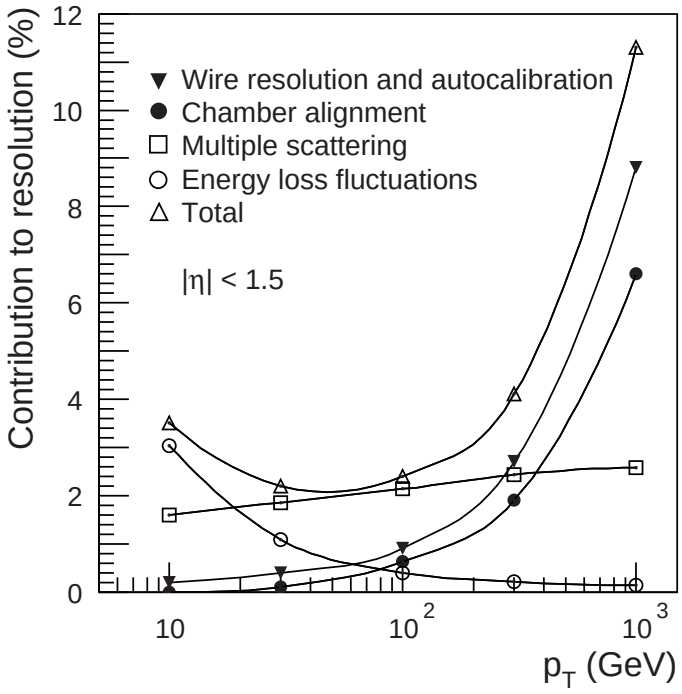

Figure 2.16. Contributions to the MS momentum resolution in the region $|\eta| < 1.5$.

magnetic field integral $\int B \cdot d\ell$) can result in a mis-calculation of the muon momentum, resulting in a degradation in the momentum resolution. These effects can be seen in Fig. 2.19, where the muon reconstruction efficiency and resolution is greatly degraded as a function of the number of hits in a road around a simulated MS track.

2.5 Trigger, Data Acquisition and Data Quality

Data acquisition (DAQ) begins and ends in a period of time called a "run", which can usually last up to around 8 hrs. In each run, combinations of trigger selections based on detector objects (muon, jet, electron, photon, τ and large missing E_T candidates) and p_T/E_T thresholds are defined in a trigger menu.

At design luminosity the bunch crossing rate is 40 MHz, with each event taking about 1.5 MB of space in storage. As most interesting physics processes occur at a much lower frequency, a trigger system is needed in order to select a subset of events passing through the detector while being fast enough to be in time with each

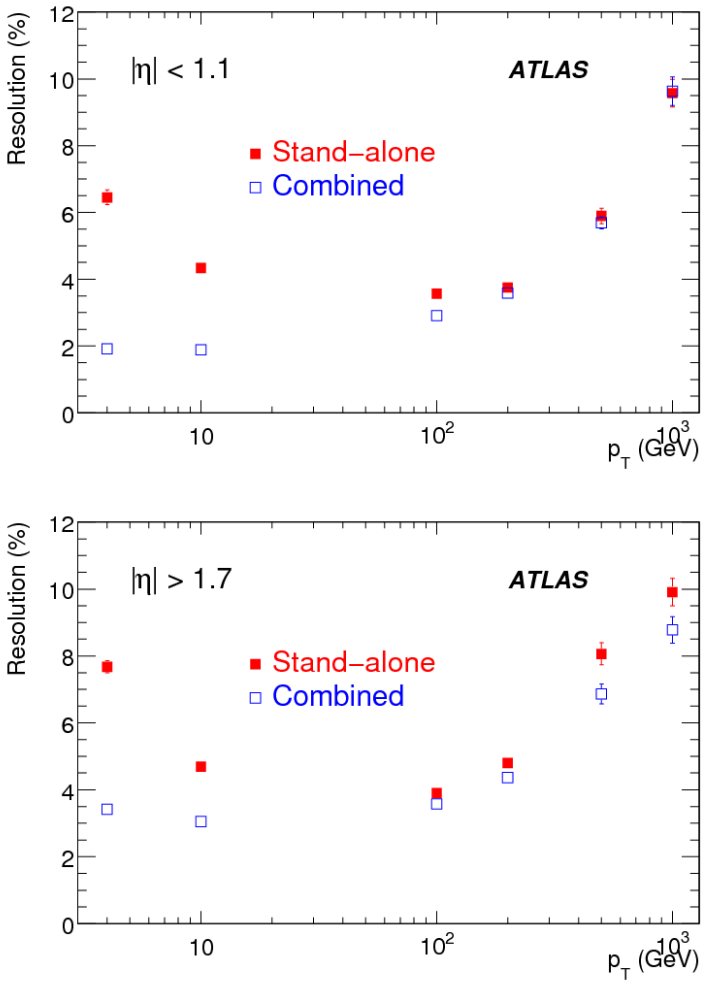

Figure 2.17. Expected relative momentum resolution for MS (standalone) and combined muons in the barrel (top) and endcap (bottom) regions.

bunch crossing. The trigger system in ATLAS accepts events in three levels: level 1 (L1), level 2 (L2) and the event filter (EF). The first is a hardware-based system, and the latter two are software-based known together as the high-level trigger (HLT). Figure 2.20 shows a block diagram of the trigger and data acquisition system in ATLAS.

The accepted rate of events is reduced at each level of the trigger, with each level seeded by the previous. The L1 trigger system accepts events by taking information

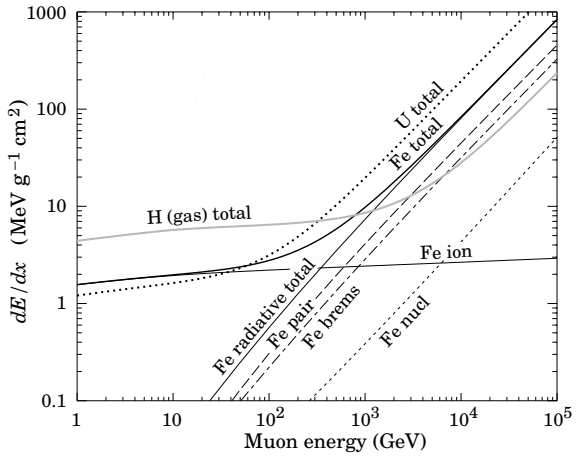

Figure 2.18. Average energy loss for a muon passing through material, as a function of muon energy. Radiative losses start to dominate for muons with energy greater than 300 GeV.

from a subset of detectors coordinated by the central trigger processor (CTP). Regions of interest (RoI) are defined based on simple signatures in the detector. The L1 trigger reduces the rate of events from 40 MHz to 100 kHz before pushing the selected events to the L2 trigger. L2 is a software-based trigger seeded by the RoI defined in L1. All detector information within a RoI is used to select events, further reducing the accept rate from 100 kHz to roughly 3 kHz. Finally, the EF selects events which have been fully built by off-line software algorithms and reduces the accept rate to around 200 to 400 Hz.

Physics event streams, such as the MuonStream, are separated by object signatures and pass events to reconstruction to be used in data analysis. The events contain information based on the predefined trigger menu of each physics stream. For example, an event which has passed `L1_MU6` contains one muon with p_T >6 GeV as determined by the L1 muon trigger. In addition, an express stream is processed quickly to provide detector monitoring and calibration, and a DEBUG stream, as the name implies, contains events which have failed reconstruction for debugging pur-

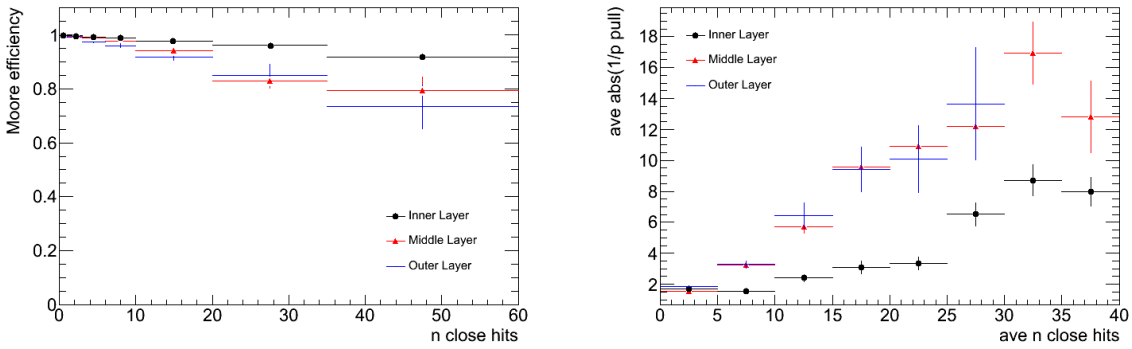

Figure 2.19. Simulated muon spectrometer standalone efficiency (left) and average 1/p residual pull (right) as a function of close MDT hits in the three MS layers.

poses. After having been accepted by the trigger system, the data in each stream is recorded and marked by luminosity blocks (LB), which are subdivisions of the run.

As the LHC increases the instantaneous luminosity, the rate becomes too high for lower p_T threshold triggers to handle. In this case, the trigger needs to be "prescaled"; that is, a subset of events are not passed to the next trigger level and are lost. The trigger prescale conditions may change at the granularity of the LB.

For physics analysis, it is important to ensure that events are selected with the best possible detector conditions. Data is selected by choosing the luminosity blocks in which the detector was capable of reading out (HV, electronics, gas circulation, etc were on and functional). In addition, the data needs to have met some quality criteria which are determined by comparing the data to expected distributions in an online monitoring framework. Luminosity block reference numbers which have passed some quality criteria are stored in a "Good Runs List" (GRL) used in the event selection stage of physics analyses. For example, the dimuon analysis presented in this thesis required that the data come from a GRL containing luminosity blocks which had passed all flags listed in Table 2.1. The definitions of these flags are listed below:

- General: The ATLAS data has been evaluated and approved by the Data Quality group, the currents in the solenoid and toroid magnets are stable (and non-

Table 2.1. Data quality flags required for luminosity blocks in the Good Runs List.

Type	Flag name
General	ATLGL, ATLSOL, ATLTOR, LUMI
Muon Spectrometer	MDTBA, MDTBC, MDTEA, MDTEC, CSCEA, CSCEC, RPCBA, RPCBC, TGCEA, TGCEC
Inner Detector	PIX0, PIXB, PIXEA, PIXEC, SCTB, SCTEA, SCTEC, TRTB, TRTEA, TRTEC, IDGL, IDAL
Trigger	L1MUE, L1MUB, TRMUO
Muon Reconstruction	MSTACO, MMUIDCB

zero), and the luminosity and forward detectors are operational and give reliable luminosity measurements.

- Muon Spectrometer: Each section of the MDT, RPC and TGC chambers must have more than 90% of the system with HV on and be collecting data. There also must be at least 3 of 4 layers taking good quality data in all CSC chambers.

- Inner Detector: The Pixel, SCT and TRT detectors are operating correctly, there are no known problems with the data, software-level tracking is OK and there are no synchronization or timing problems in the ID detector.

- Trigger: Muon triggers in both the barrel and the endcap have been on and running with reasonable efficiency, and there were no timing, consistency, synchronization or data problems.

- Muon Reconstruction: The software algorithms Staco and Muid were running without problems.

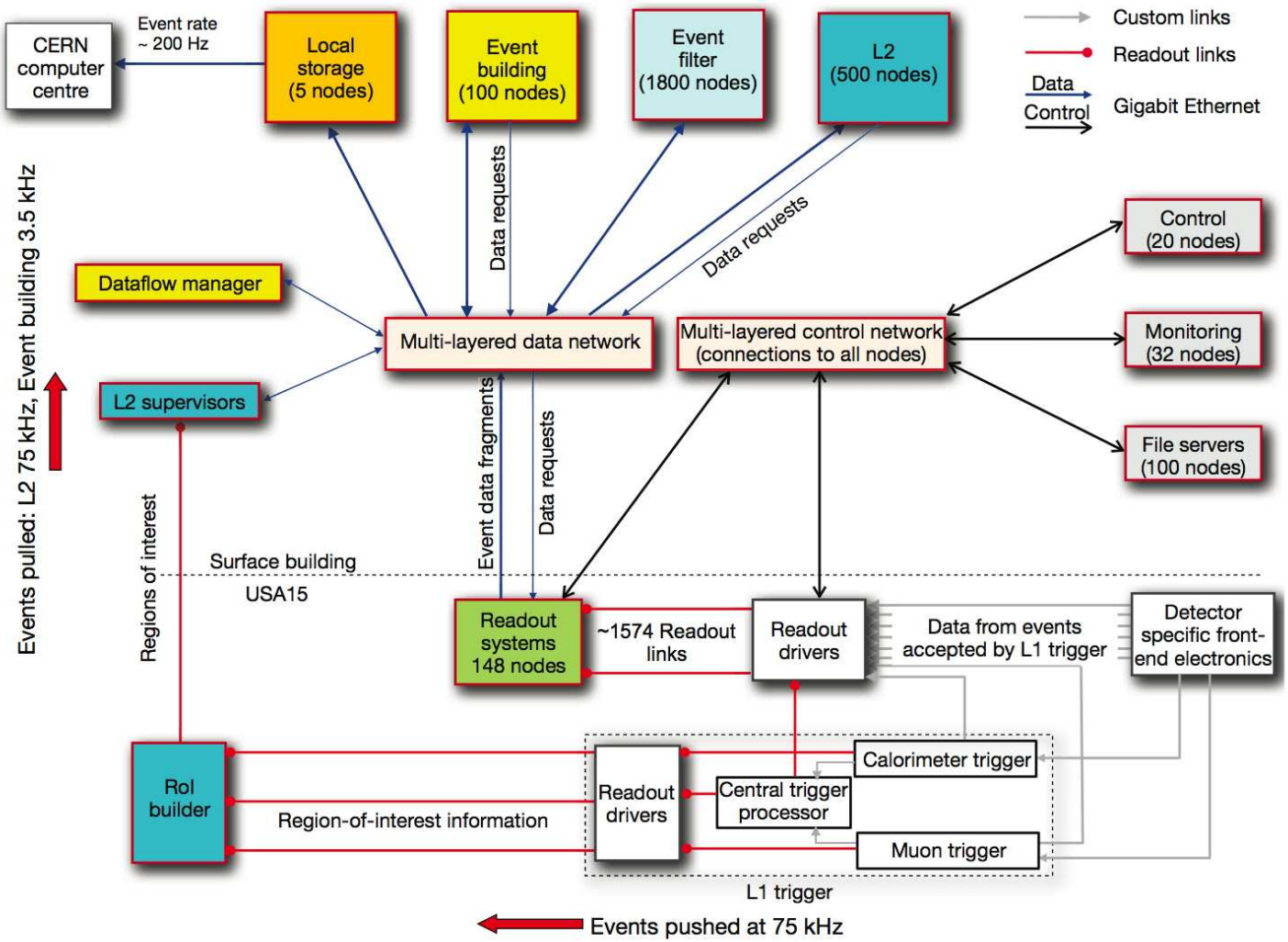

Figure 2.20. Diagram of the ATLAS trigger and data acquisition system.

CHAPTER 3

SIMULATION OF SIGNAL SAMPLES AND DIMUON BACKGROUNDS

The simulation samples used to predict the expected yield of Standard Model physics processes relevant to dimuon signatures are presented in this chapter. Section 3.1 gives details about the SM $Z/\gamma^* \to \mu\mu$ simulation samples, and section 3.2 discusses the signal cross sections and simulated samples used for the contact interaction search. Section 3.3 discusses various non-DY dimuon backgrounds which can occur in pp collisions. The last section introduces other non-collision backgrounds which also need to be considered in the analysis.

All samples were produced at $\sqrt{s} = 7$ TeV center of mass energy via event generators as discussed in section 1.4. After event generation, the response of the ATLAS detector to particles produced in the event was simulated with the GEANT4 [77] toolkit, which uses Monte Carlo techniques to simulate the passage of particles through the detector elements and the response of detector electronics.

As the LHC begins pushing the luminosity envelope, other interactions besides the primary hard scattering can happen in an event. Called "pileup", this can affect the soft QCD particle distributions in the detector. For all samples, the effect of multiple proton-proton collisions in one bunch crossing was modeled by overlaying extra soft QCD events (mainly from proton remnants) over the original hard-scattering event.

3.1 Standard Model $Z/\gamma^* \to \mu\mu$ Production

The main background for a new physics signature involving two muons in the final state is Z/γ^* production with subsequent decay to $\mu^+\mu^-$. Because the SM

dimuons look the same in the detector on an event-by-event basis as they would for a contact interaction signal, the $Z/\gamma^* \to \mu\mu$ contribution is known as an "irreducible" background in the analysis. An advantage in the analysis is that the Z^0 peak can be used as a control region to anchor the invariant mass distribution in the region where there is no contribution from new physics[1]. Thus, it is important to have a good understanding of DY production in ATLAS and to measure the detector response with high precision.

The Z/γ^* events are produced using the PYTHIA (6.421) event generator. This production uses a leading order matrix element calculation of the hard scattering and the MRST2007LO* PDF set, where LO* refers to modified leading-order PDFs which seek to lessen the difference between LO and NLO processes for DY production over a large range of x [78].

In this analysis, the Z/γ^* simulation is produced in two ways: first, as a large inclusive sample with a low generator-level mass-cutoff at $m_{\mu\mu} > 60$ GeV, and second, in a series of eleven mass bins from 75 GeV to 2 TeV (Fig. 3.1). The latter ensures a smooth background spectrum with sufficient statistics in the high mass tail of the DY. Table 3.1 shows the LO cross sections for these processes.

3.2 Simulated Contact Interaction Signal Samples

Simulated samples for the signal contact interaction (CI) processes were used to predict the expected new physics yield and detector response in the signal region defined in the mass range $m_{\mu\mu} > 150$ GeV. As with the Standard Model DY discussed in the previous section, the CI processes were produced with PYTHIA and MRST2007LO* PDF sets. The CI was simultaneously generated with DY production in order to correctly account for the interference term between these two processes, thus the term

[1]This normalization procedure is detailed later in section 6.4.

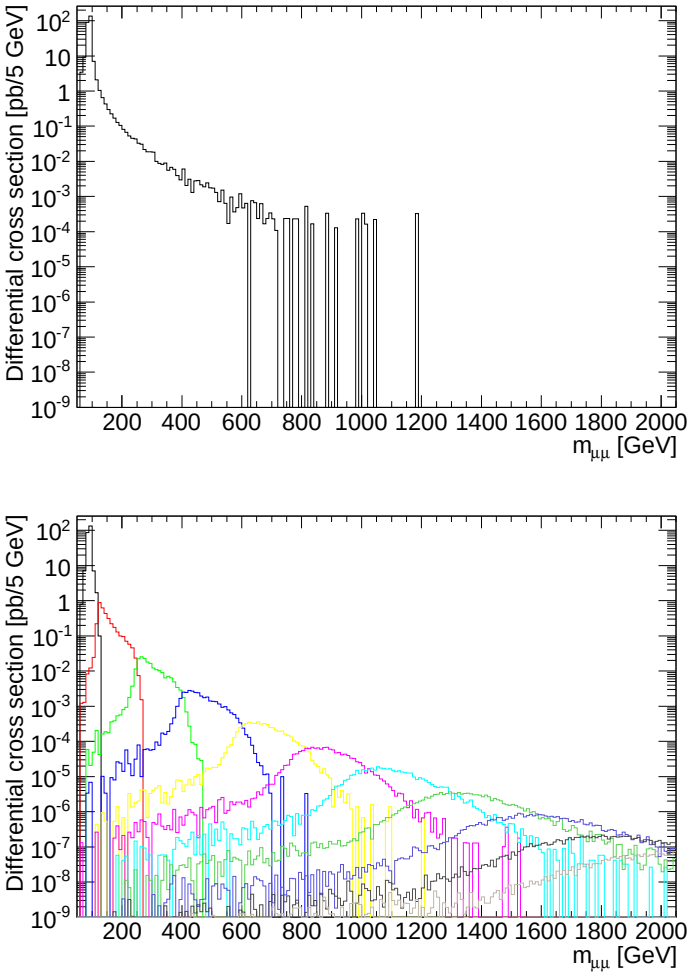

Figure 3.1. Invariant mass after simulation for the inclusive $Z/\gamma^* \rightarrow \mu\mu$ sample (top) and the binned samples (bottom).

"signal samples" as will be used throughout this text refers to DY and CI together. A total of 50,000 events were produced for each of eight benchmark signal samples with various values of the CI scale Λ: four samples with constructive interference (η=-1) and four with destructive interference (η=+1). At the generation stage, events were produced above an invariant mass of 120 GeV to increase the number of events produced in the signal region. An example of python job options used for the PYTHIA

Table 3.1. Leading order cross sections and number of events produced for the $Z/\gamma^* \to \mu\mu$ samples.

Process	σ [pb]	N_{evts} [$\times 10^3$]
$Z/\gamma^* \to \mu\mu$ ($m_{\mu\mu} > 60$ GeV)	855.25	5 000
$Z/\gamma^* \to \mu\mu$ mass bins		
$75 < m_{\mu\mu} < 120$ GeV	817.05	20
$120 < m_{\mu\mu} < 250$ GeV	8.69	20
$250 < m_{\mu\mu} < 400$ GeV	0.414	20
$400 < m_{\mu\mu} < 600$ GeV	0.0675	20
$600 < m_{\mu\mu} < 800$ GeV	0.0112	20
$800 < m_{\mu\mu} < 1000$ GeV	2.73×10^{-3}	20
$1000 < m_{\mu\mu} < 1250$ GeV	9.16×10^{-4}	20
$1250 < m_{\mu\mu} < 1500$ GeV	2.49×10^{-4}	20
$1500 < m_{\mu\mu} < 1750$ GeV	7.69×10^{-5}	20
$1750 < m_{\mu\mu} < 2000$ GeV	2.60×10^{-5}	20
$m_{\mu\mu} > 2000$ GeV	1.53×10^{-5}	20

Table 3.2. Benchmark contact interaction signal Λ values and LO cross sections including DY ($\sigma \times BF(X \to \mu\mu)$) for $m_{\mu\mu}$ >120 GeV with constructive ($\eta = -1$) and destructive ($\eta = +1$) interference.

Λ [TeV]	$\sigma \times BF$ for $\eta = -1$ [pb]	$\sigma \times BF$ for $\eta = +1$ [pb]
2	-	16.94
3	11.69	10.32
4	10.15	9.40
5	9.73	9.18
7	9.41	-
∞ (DY-only)	9.19	

event generation is in the appendix. Table 3.2 shows the leading-order production cross sections for each sample.

As shown in Fig. 1.6, in the limit of $\Lambda \to \infty$, the cross section reduces to the expected DY-only value. Fig. 3.2 shows the true invariant mass distributions of the benchmark signal samples. Here also, the mass distributions tend to the SM value as $\Lambda \to \infty$. The larger invariant mass causes the contact interaction system to be more central in the detector, as can be seen in Fig. 3.3. The presence of new physics also

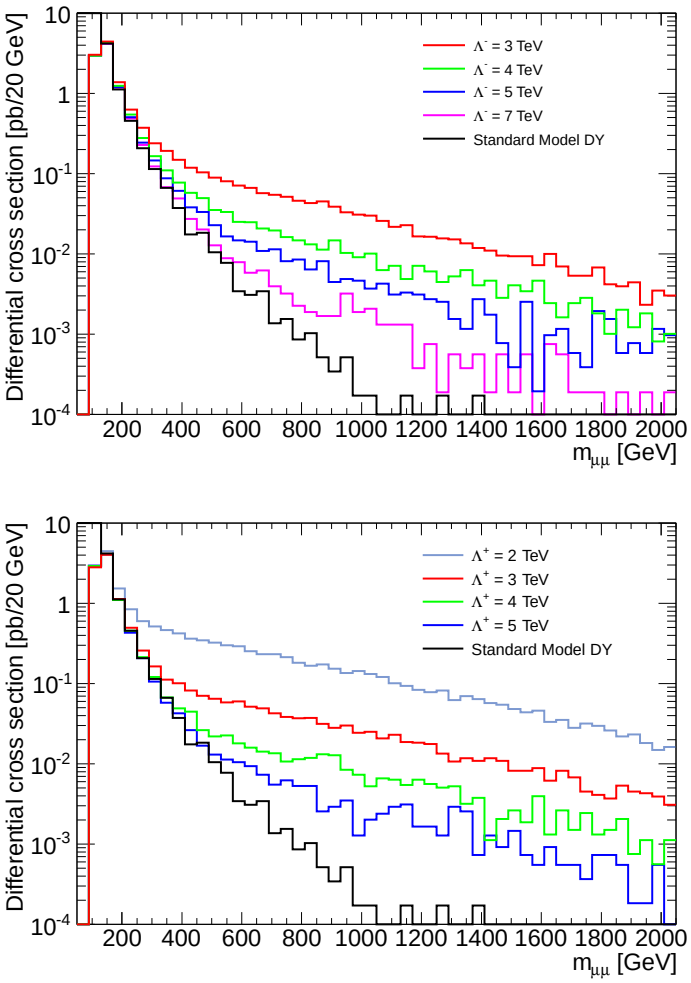

Figure 3.2. True invariant mass of signal samples for constructive (top) and destructive (bottom) interference.

causes the dimuon system to be more boosted in both the transverse and longitudinal directions, shown in Fig. 3.4.

The muon distributions in samples including new physics also show a larger tail in the transverse momentum distribution (Fig. 3.5). There is also a charge asymmetry (Fig 3.6, 3.7) as predicted by the axial-vector form of the Lagrangian. While the neutral current does not maximally violate parity, the effect is still present, and is much more apparent in the new physics process.

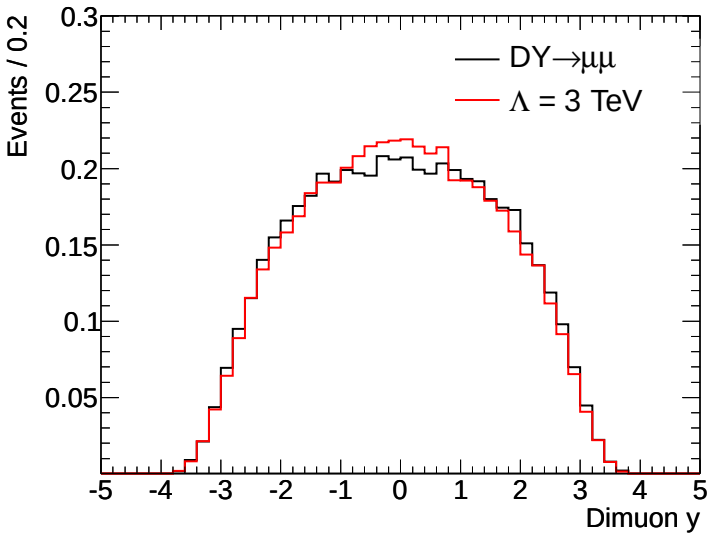

Figure 3.3. Generator level distribution of the dimuon rapidity comparing the Standard Model Drell-Yan with a contact interaction $\Lambda^- = 3$ TeV. Here, the CI distribution is normalized to the SM yield. These events have $m_{\mu\mu} > 120$ GeV.

3.3 Reducible Dimuon Background Processes

The largest non- DY $\rightarrow \mu\mu$ collision backgrounds producing dimuon events are those arising from QCD processes (such as $b\bar{b}$, $c\bar{c}$ and $t\bar{t}$) as well as from other EW processes (such as $W \rightarrow \mu\nu$, $Z \rightarrow \tau\tau$ and diboson production).

The $b\bar{b}$ and $c\bar{c}$ samples were produced with quark-antiquark, quark-gluon and gluon-gluon hard scatters in PYTHIA. The diboson production (which includes W^+W^-, $W^{\pm}Z$ and ZZ processes) was produced using the HERWIG event generator with the MRST2007LO* PDF set, where the matrix element calculation was done to NLO. A $W^{\pm} \rightarrow \mu\nu$ sample was produced with PYTHIA and also used the MRST2007LO* PDF set in the cross section calculation.

The $t\bar{t}$ sample was produced with MC@NLO (3.41) to generate matrix elements with CTEQ6.6 PDFs, JIMMY (4.31) to describe multiple parton interactions and HERWIG (6.510) to describe the remaining underlying event. All backgrounds used are listed in Table 3.3, along with their cross sections.

Table 3.3. Generators and number of events produced for the dominant background samples. The cross sections, the QCD order to which order they were calculated, and the generator filter (if available) are listed.

Process	Generator	Cross section [pb]	N_{evts} ($\times 10^3$)	Notes
$W^{\pm} \to \mu\nu$	PYTHIA	10 454, LO	7 000	
$Z \to \tau\tau$	PYTHIA	855.25, LO	2 000	$\sqrt{s} > 60$ GeV
$c\bar{c}$	PYTHIA	2.84 $\times 10^4$, LO	1 500	15 GeV single μ filter
$b\bar{b}$	PYTHIA	7.39 $\times 10^4$, LO	4 400	15 GeV single μ filter
$t\bar{t}$	MC@NLO	161 ($\times 0.538$), NNLO	200	Single lepton filter
Diboson production	HERWIG			
W^+W^-		44.92 ($\times 0.39$), NLO	25	
$W^{\pm}Z$		17.97 ($\times 0.31$), NLO	25	
ZZ		5.96 ($\times 0.21$), NLO	25	

Examples of dimuon production in these physics processes are shown in Fig 3.8. It should be noted that while the $t\bar{t}$ decay chain has the same form as that of $c\bar{c}$ and $b\bar{b}$, because of the large top mass, the jet and muon decay products are less collinear than for the other heavy-flavor decays. Thus, muons from $t\bar{t}$ decays tend to be isolated in the ID and calorimeters, in contrast to muons originating from $c\bar{c}$ or $b\bar{b}$ decays.

3.4 Background from Cosmic Muons

Lastly, though ATLAS resides ∼200 ft underground and is mostly shielded from cosmic particle interactions in the atmosphere[2], there is still a chance that muons coming from these interactions may reach the detector. If close enough to the interaction point, one cosmic muon can appear in the detector as two muons back-to-back in η and mimic a dimuon signature (see Fig. 3.9). The value of $\eta_{\mu 1} + \eta_{\mu 2}$ (which is ∼0 for these events) can be used as a discriminant to either reject cosmic events or to put an upper bound on their rate in the collision dataset. This will be discussed later in the context of the analysis.

[2]In reality, there are two large access shafts, which leave part of the detector less shielded from cosmic rays.

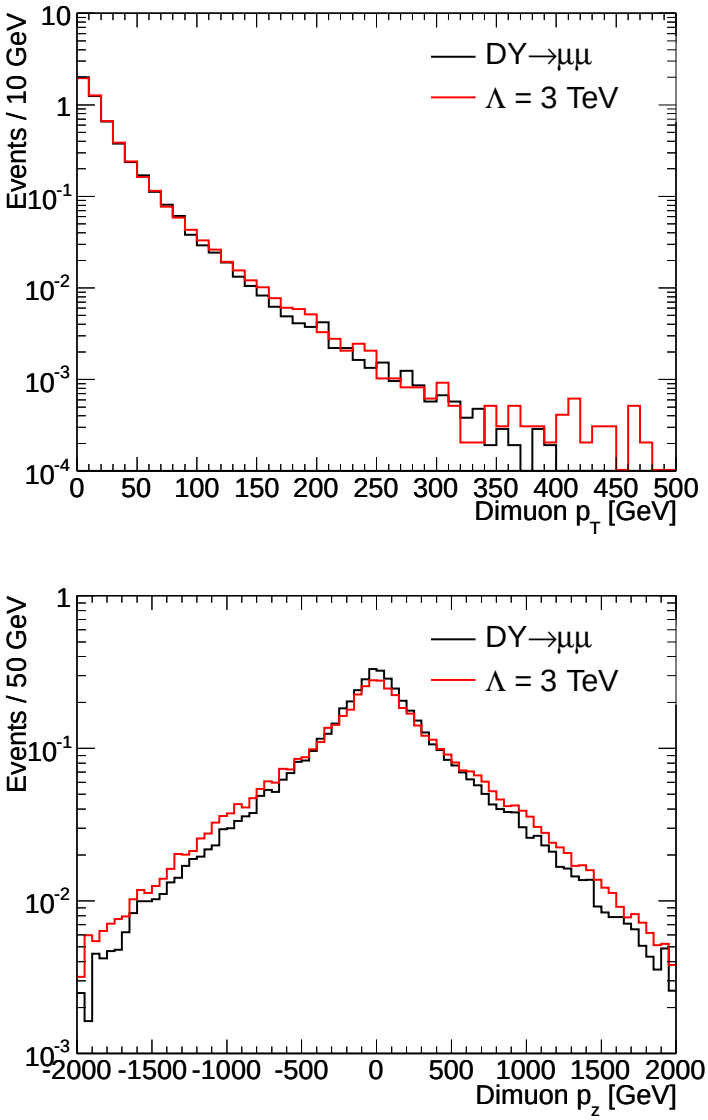

Figure 3.4. Generator level distributions of the dimuon transverse (top) and longitudinal (bottom) momentum comparing the Standard Model Drell-Yan with a contact interaction $\Lambda^- = 3$ TeV. Here, the CI distributions are normalized to the SM yield. These events have $m_{\mu\mu} > 120$ GeV.

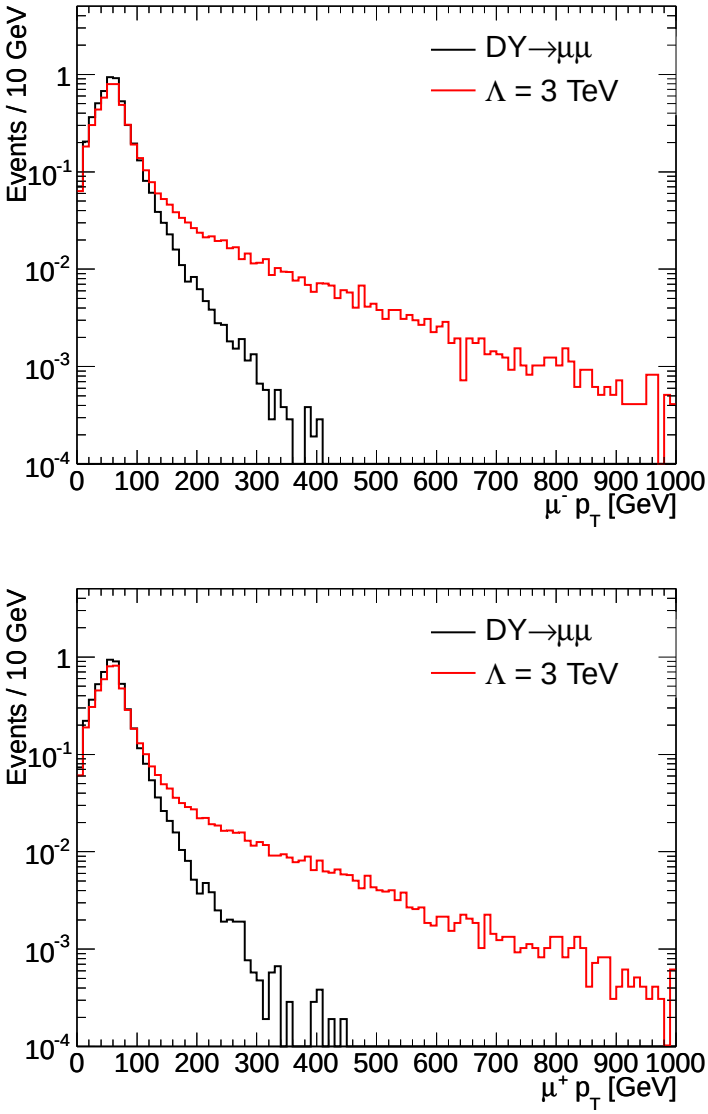

Figure 3.5. Generator level distributions of the muon transverse momentum for negative (top) and positive (bottom) muons, comparing the Standard Model Drell-Yan with a contact interaction $\Lambda^- = 3$ TeV. Here, the CI distributions are normalized to the SM yield. These events have $m_{\mu\mu} > 120$ GeV.

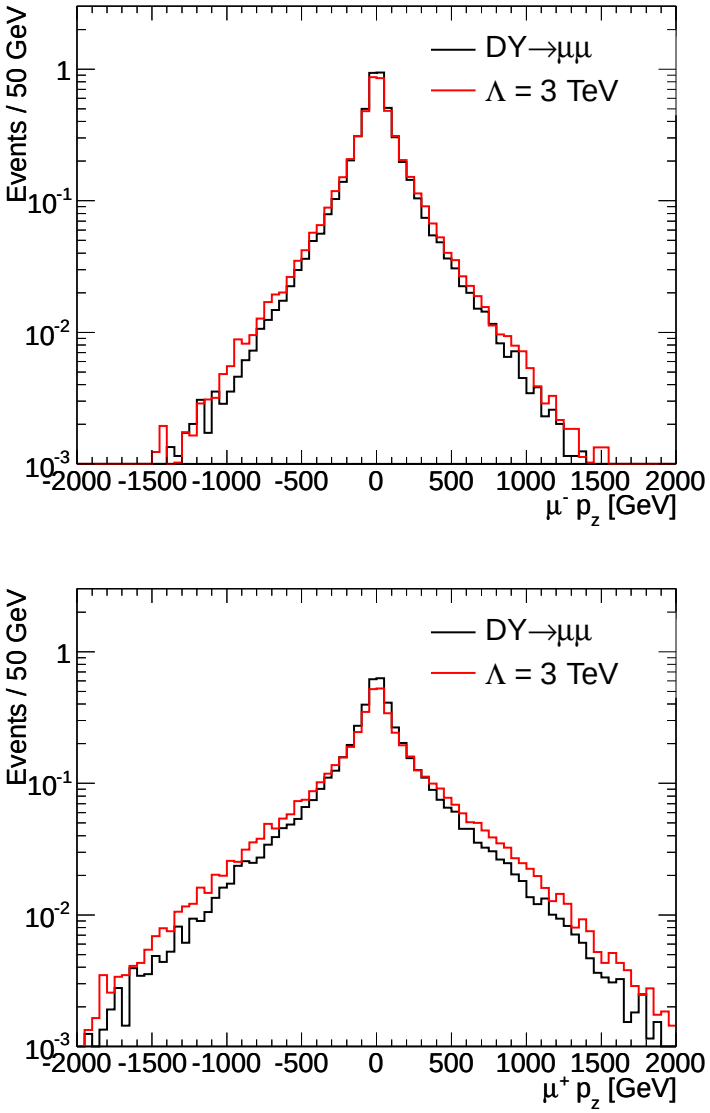

Figure 3.6. Generator level distributions of the muon longitudinal momentum for negative (top) and positive (bottom) muons, comparing the Standard Model Drell-Yan with a contact interaction $\Lambda^- = 3$ TeV. Here, the CI distributions are normalized to the SM yield. These events have $m_{\mu\mu} > 120$ GeV.

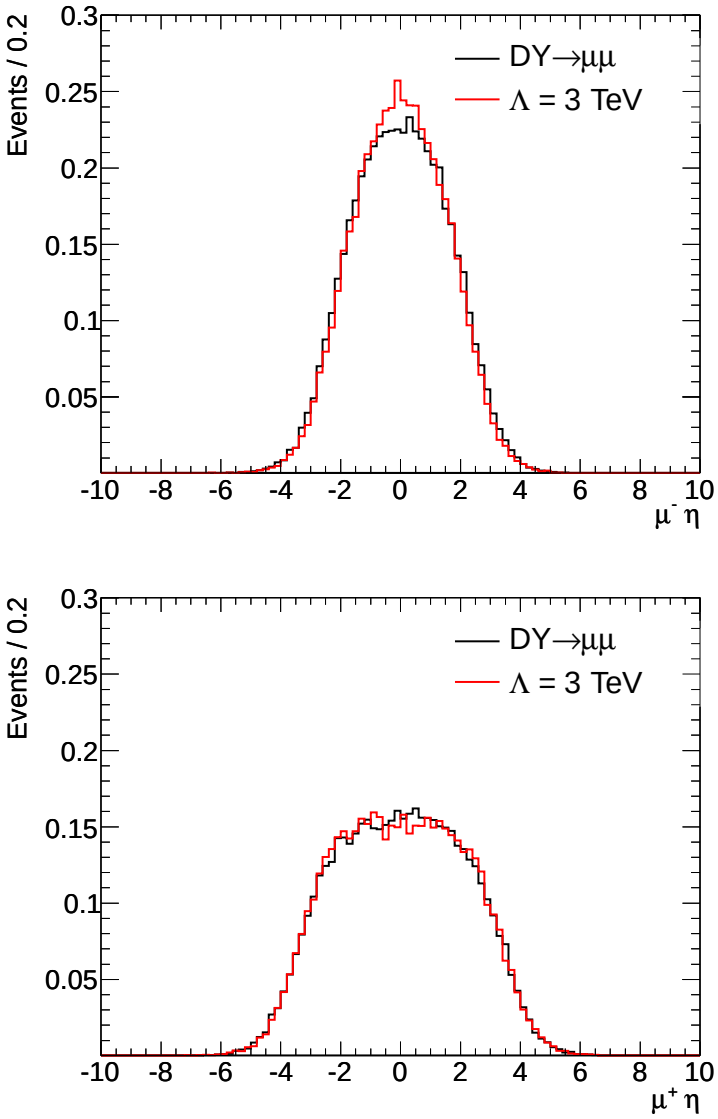

Figure 3.7. Generator level distributions of the muon pseudorapidity for negative (top) and positive (bottom) muons, comparing the Standard Model Drell-Yan with a contact interaction $\Lambda^- = 3$ TeV. Here, the CI distributions are normalized to the SM yield. These events have $m_{\mu\mu} > 120$ GeV.

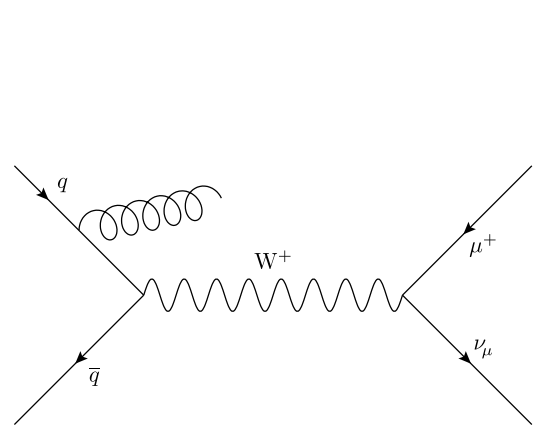

(a) $W \to \mu\nu$ with jet production, where the second muon may be produced in the jet

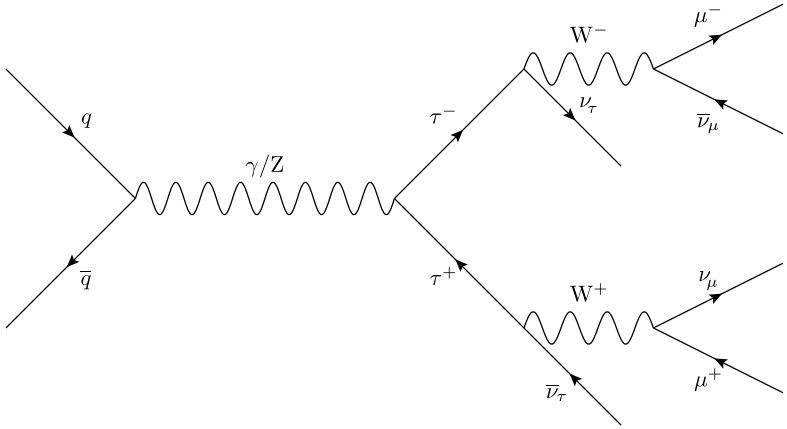

(b) $Z \to \tau^+\tau^- \to \mu^+\mu^-\nu_\tau\bar{\nu}_\tau\nu_\mu\bar{\nu}_\mu$

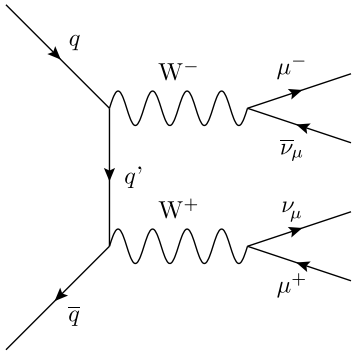

(c) Diboson production

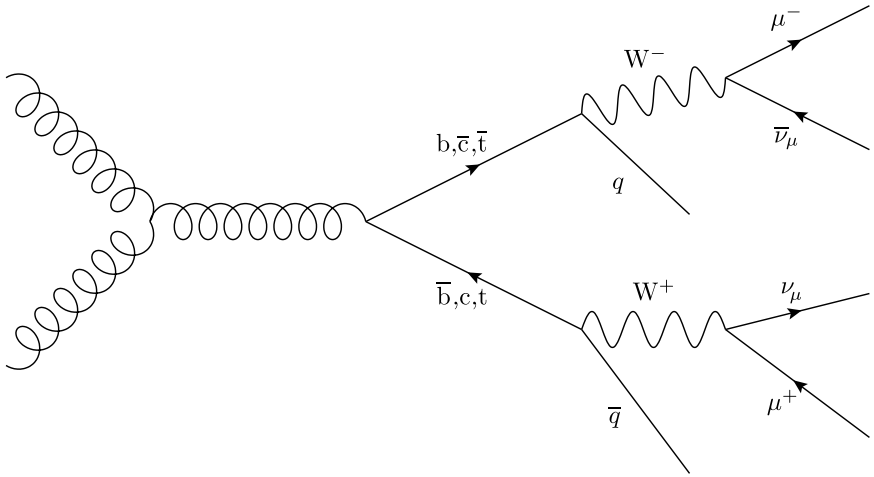

(d) Heavy flavor decays with muons in the final state

Figure 3.8. Examples of dimuon production in various background processes.

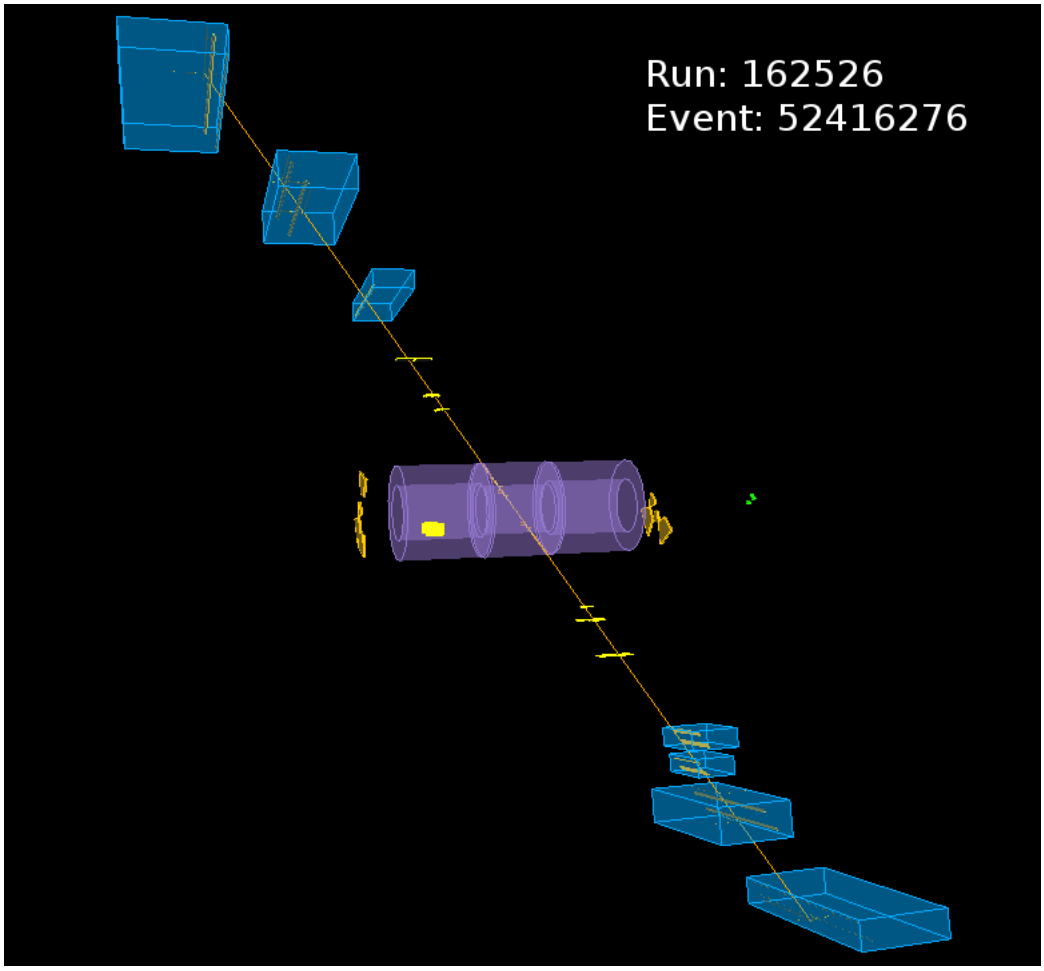

Figure 3.9. Cosmic muon event triggered in ATLAS, passing close to the interaction point in a non-collision event. The first muon in the upper hemisphere has $\eta = -0.63$, $p_T = 177.9$ GeV, and the second muon in the lower hemisphere has $\eta = 0.63$, $p_T = 176.1$ GeV. The combined invariant mass of the two muons is 425.7 GeV.

CHAPTER 4

MEASUREMENT OF THE Z^0 CROSS SECTION IN THE DIMUON CHANNEL WITH 331 nb^{-1}

Rediscovering the Z^0 boson and verifying its consistency with Standard Model expectations at $\sqrt{s} = 7$ TeV was the first step to be undertaken before looking for new physics in the high invariant mass tail of the DY spectrum. Within months after the LHC began delivering collisions, the first $Z^0/\gamma^* \to \mu\mu$ (or as will be denoted from now on, $Z \to \mu\mu$) events were observed in the ATLAS detector and the inclusive production cross section was measured. This chapter describes the $Z \to \mu\mu$ analysis performed with 331 nb^{-1}, and while it is a summary of an analysis described in much greater detail elsewhere [79, 80, 81], it serves as an introduction to high mass dimuons in ATLAS, demonstrates an early understanding of the detector performance as well as sets the stage for results which will be presented in subsequent chapters.

4.1 Properties of the Z^0 Boson

The most precise measurements of the Z^0 boson properties were carried out by the LEP experiments, which measured the mass $m_Z = 91.1876 \pm 0.0021$ GeV and the full Z^0 natural width $\Gamma = 2.4952 \pm 0.0023$ GeV [44, 62]. The Z^0 can decay into all fundamental fermion/antifermion pairs except for the top quark which is too massive. Table 4.1 shows the Z^0 decay channels and corresponding branching fractions (Γ_i/Γ).

The $Z \to \mu\mu$ line shape as a function of center of mass energy of the interaction squared ($\hat{s}$) is given by the following relativistic Breit-Wigner functional form:

$$f(\hat{s}) \propto \frac{1}{(\hat{s} - m_Z) + m_Z^2\Gamma} \quad . \tag{4.1}$$

Table 4.1. Measured Z^0 decay modes and branching fractions. In the Standard Model, the invisible mode is assumed to be decays to neutrinos.

Mode	Γ_i/Γ
$\ell^+\ell^-$	3.37 % (×3)
Invisible	20.0 %
Hadrons	69.9 %
$(u\bar{u} + c\bar{c})/2$	11.6 %
$(d\bar{d} + s\bar{s} + b\bar{b})/3$	15.6 %
$c\bar{c}$	12.0 %
$b\bar{b}$	15.1 %

4.2 Early 2010 Data

Collisions at $\sqrt{s} = 7$ TeV were first seen in ATLAS on March 30th, 2010, with the first $Z \to \mu\mu$ candidate seen on May 10th (Fig. 4.1). The 331 nb^{-1} dataset was split into four main run periods (A, B, C and D) based on different LHC run conditions. The run numbers corresponding to these periods along with the recorded luminosity based on the Level 1 trigger with the lowest un-prescaled momentum threshold ($p_T > 6$ GeV, labeled as `L1_MU6`) are shown in Table 4.2.

4.3 Formulation of the Cross Section

The cross section times branching fraction for the Z^0 decaying into two muons, $BF(Z \to \mu\mu)$, is defined as:

$$\sigma_Z \times BF(Z \to \mu\mu) = \frac{N_{obs} - N_{bg}}{L_{int} A_Z C_Z} \quad , \tag{4.2}$$

Table 4.2. Run periods and corresponding integrated luminosity used for the $Z \to \mu\mu$ analysis.

Run Period	Run Numbers	Luminosity [nb^{-1}]
A and B	152166-155160	8.89
C	155228-156682	8.71
D	158045-159224	313.2
Total		330.6

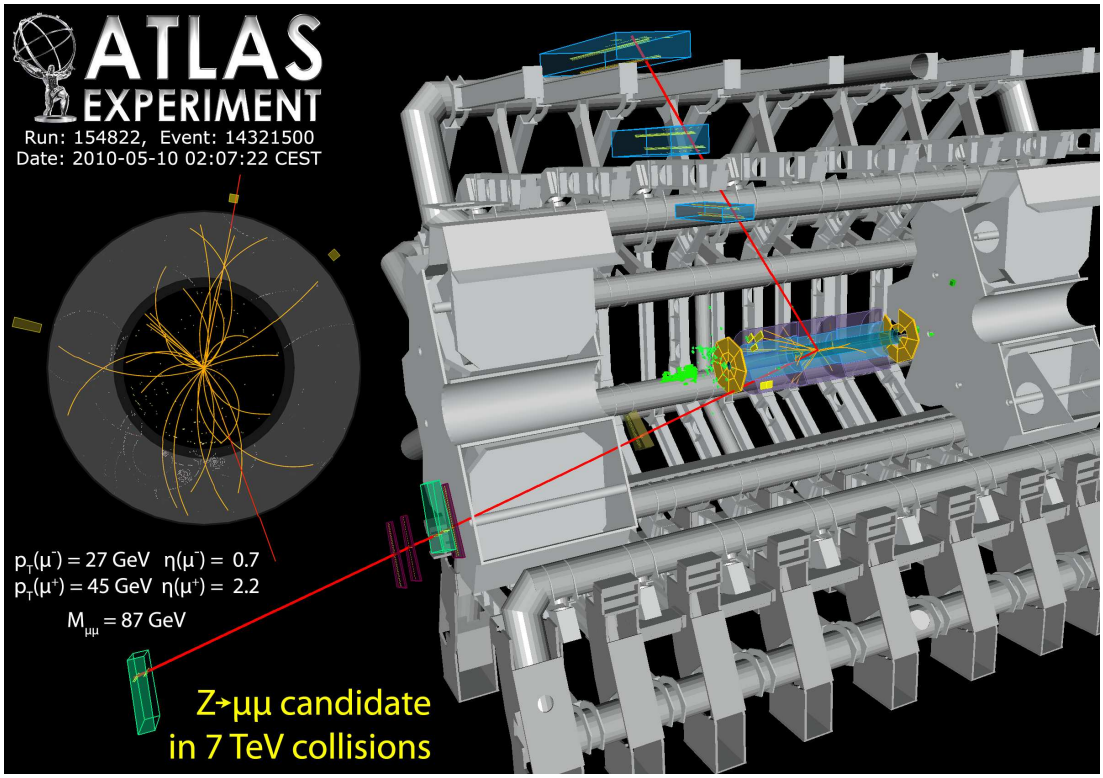

Figure 4.1. Candidate $Z \to \mu\mu$ event recorded on May 10, 2010.

where N_{obs} is the number of $Z \to \mu\mu$ candidate events observed, N_{bg} is the number of expected background events, L_{int} is the integrated luminosity, A_Z is the generator-level acceptance of the fiducial region, and C_Z is the selection and detector-related efficiency within the fiducial region. The following sections detail how each of these components were calculated.

4.4 Candidate Selection

To discriminate $Z \to \mu\mu$ candidates in data from collision and cosmic backgrounds as well as to ensure that muons were chosen with a high level of quality in the event, selection was performed in three stages: event selection, preselection and dimuon selection.

In the event selection stage, a Good Runs List (GRL) was used to select luminosity blocks in data where the ATLAS detector met some predefined quality criteria in the ID and MS (see section 2.5). After being accepted by the `L1_MU6` trigger, the event was required to have at least one primary vertex (PV) with three associated tracks and longitudinal distance from the origin $|z| < 150$ mm. This requirement reduced the background of non-collision events triggered by cosmic muons.

The preselection stage was motivated by having common muon selection with the simultaneous $W^{\pm} \to \mu\nu$ cross section measurement and to reduce the data size further from the large number of triggered collision events. Here, one combined Staco muon with transverse momentum $p_T > 20$ GeV and pseudorapidity $|\eta| < 2.4$ was required. The muon was also required to have $p_T >$10 GeV measured in the MS only, and the difference between the MS- and ID-only p_T measurements $|p_T^{ID} - p_T^{MS}| < 15$ GeV. In addition, to reduce the cosmic ray background further, the longitudinal impact parameter z_0 of the combined muon was required to be within 100 mm of the selected PV in the event (in case there was more than one PV in the event, the vertex with highest sum-p_T of associated tracks was chosen as the leading PV).

The dimuon selection stage required two such muons passing all selection as described above for the preselection stage. In addition, in order to reduce the dominant non-isolated QCD dimuon backgrounds originating from $b\bar{b}$ and $c\bar{c}$ decays, both muons were required to be track-isolated in the ID. Here, a muon was considered "isolated" if the sum-p_T^{ID} in a cone around the muon relative to the muon-p_T was less than 0.2 for a cone size $dR <$0.4. Finally, $Z \to \mu\mu$ candidates were selected if both muons were oppositely charged and the invariant mass of the dimuon system was within the range $66 < m_{\mu\mu} < 116$ GeV to be wider than the resolution of the peak, which was expected to be roughly 5 GeV at the time the analysis was performed. The final selection flow on data is shown in Table 4.3, with 109 $Z \to \mu\mu$ candidates observed.

Table 4.3. Event selection flow on the 330 nb^{-1} data sample. The kinematic selection included all p_T and η selection on the dimuons.

Selection Criteria	Number of Events
GRL	35 756 532
Trigger	5 464 740
Preselection	22 075
2 combined muons	1 879
Kinematic selection	144
Isolation	117
Mass window	$N_{obs} = 109$

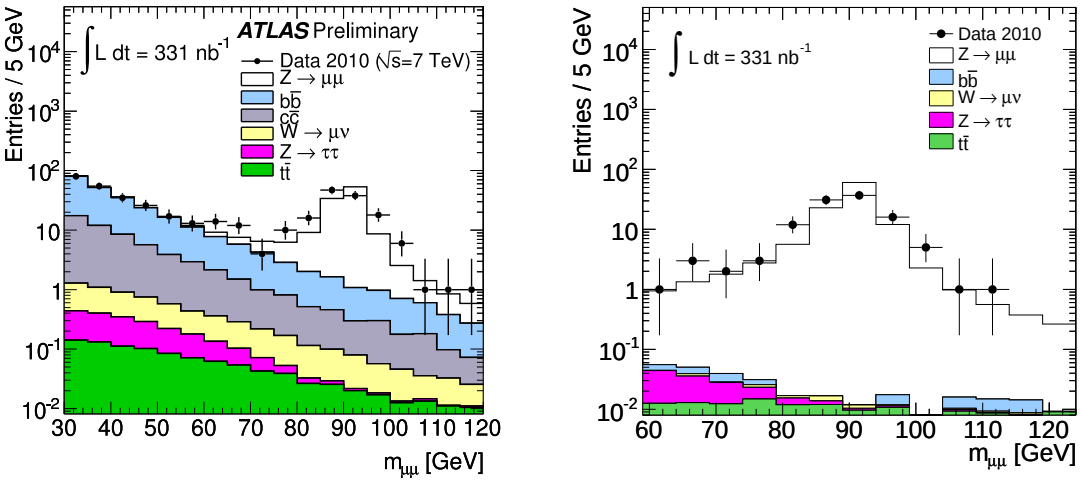

Figure 4.2. Dimuon invariant mass distribution after preselection (left) and after all selection (right).

Figure 4.2 shows the dimuon mass in data compared to simulation after both the preselection stage and the full selection criteria were applied. Fitting the invariant mass peak with a Breit-Wigner function of constant width $\Gamma = 2.4952$ GeV convoluted with a Gaussian of variable width σ to account for the intrinsic $Z \to \mu\mu$ width and resolution, respectively, a mean 89.9 ± 0.6 GeV was found with width $\sigma = 4.57 \pm 0.64$ GeV (Fig. 4.3). The nominal resolution of the $Z \to \mu\mu$ width found by fitting the mass distribution in simulation was $\sigma = 2.11 \pm 0.01$ GeV.

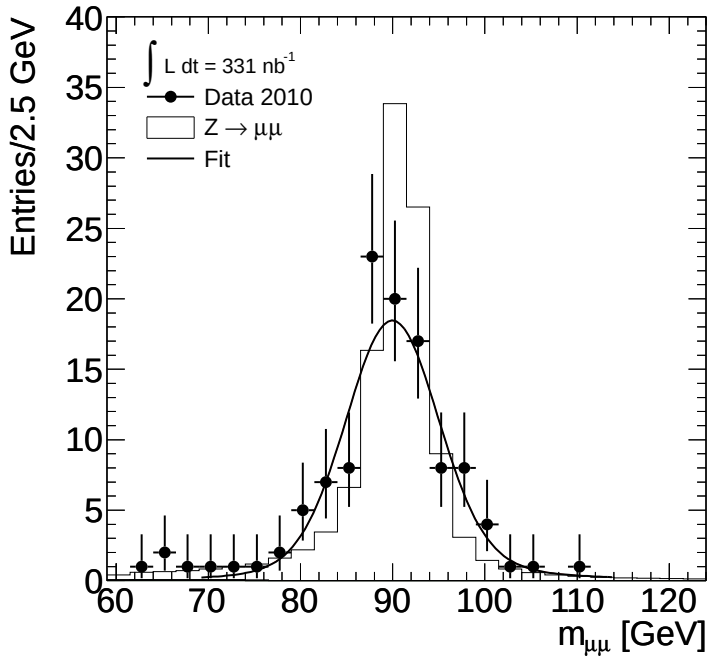

Figure 4.3. Fit to dimuon invariant mass distribution in data after all selection.

4.5 Yield of $Z \to \mu\mu$ Backgrounds

To predict the expected yield of dimuon SM processes, samples were generated and simulated as discussed in Chapter 3. For this analysis, the backgrounds considered include EW processes ($W^{\pm} \to \mu\nu$ and $Z \to \tau\tau$) and heavy flavor (or "QCD") processes ($c\bar{c}$, $b\bar{b}$ and $t\bar{t}$). Having a very small predicted yield, the diboson backgrounds was considered negligible for the 330 nb^{-1} analysis. The contamination from cosmic muons was also considered negligible. Two data-driven methods were used to predict the non-isolated background arising from $b\bar{b}$ and $c\bar{c}$ decays, which are listed below:

- **Reversing the isolation requirement in a mass window at and below the Z^0 peak:** Because muons are expected to be well isolated in the signal region, the so-called "$ABCD$" method can be used to predict the yield of non-isolated backgrounds. In this method, four categories are considered by choosing

two mass regions in which the samples are separated into events with isolated dimuons and events for which the isolation selection is reversed for both muons:

- A: Both muons are isolated and 66< $m_{\mu\mu}$ <116 GeV
- B: Both muons are isolated and 40< $m_{\mu\mu}$ <60 GeV
- C: Both muons have reverse isolation selection and 66< $m_{\mu\mu}$ <116 GeV
- D: Both muons have reverse isolation selection and 40< $m_{\mu\mu}$ <60 GeV

From simulation, the ratio of isolated muons to muons from jets is independent of the invariant mass, and the number of $c\bar{c}$ and $b\bar{b}$ events in the signal region (A) is given by:

$$\frac{A}{C} \approx \frac{B}{D} \quad \rightarrow \quad A \approx \frac{B \times C}{D}.$$

After all selection, the values found were $B = 4$, $C = 3$ and $D = 5$ events, which predicted $A = 2.4 \pm 2.1$ (stat) background events in the signal region.

- **Fitting the invariant mass under the Z^0 peak with an exponential function:** In this method, a compound function is created by adding an exponential function to a Breit-Wigner convoluted with a Gaussian. The exponential extends above and below the signal region (30< $m_{\mu\mu}$ <120 GeV), while the peak function is constrained to the range 66< $m_{\mu\mu}$ <116 GeV. Using the parameters extracted for the exponential after fitting the compound function to the data, the estimated background in the signal region is 0.0074 ± 0.0014 (stat).

In both cases, the background from QCD processes in data was found to be consistent with the simulation prediction within the large statistical errors, and so the background was estimated from simulation for the analysis. The total number of expected background events from simulated events will be summarized later, after other data-driven muon reconstruction and efficiency measurements which were applied to the simulation samples are discussed.

4.6 Acceptance

The acceptance, estimated from simulation, was divided into two components in order to separate it into a generator-level-only part (A_Z) and a part which was comprised of the reconstruction-level acceptance (C_Z).

The truth-level acceptance A_Z is defined as the fraction of generated $Z \to \mu\mu$ events which lay in the fiducial region of the detector; that is, events which had two muons each with p_T^{truth} >20 GeV, $|\eta^{truth}| < 2.4$ and an invariant mass within the region 66< $m_{\mu\mu}^{truth}$ <116 GeV. The value of this acceptance, calculated in PYTHIA before any final-state radiation, was $A_Z = 0.486 \pm 0.014$ (stat).

The second component of the acceptance C_Z is the acceptance of events after all selection within the fiducial region defined for A_Z. The value determined from simulation, folding in trigger and reconstruction efficiency, was found to be $C_Z = 0.788 \pm 0.001$ (stat). However, because the simulation lacked a complete description of the data, corrections to C_Z were made by measuring efficiencies using data-driven methods. The ratio of an efficiency found in data to what was estimated in simulation is called the scale factor (SF) and was derived for the reconstruction and trigger components separately. In the following two sections, the data-driven methods for single-muon efficiencies are described, as well as the propagation of these efficiencies to the two-muon case.

4.6.1 Reconstruction Efficiency Scale Factor

Two methods were used to determine the combined muon reconstruction efficiency in situ for the 331 nb^{-1} measurement. The first and more standard, known as the "tag and probe" method, takes one selected combined muon (tag) and matches it with an oppositely-charged isolated ID track (probe). Using an invariant mass window around the Z^0 peak as a constraint, if there was no second muon in the event found to be associated to a probe ID track, this resulted in a loss of efficiency. While

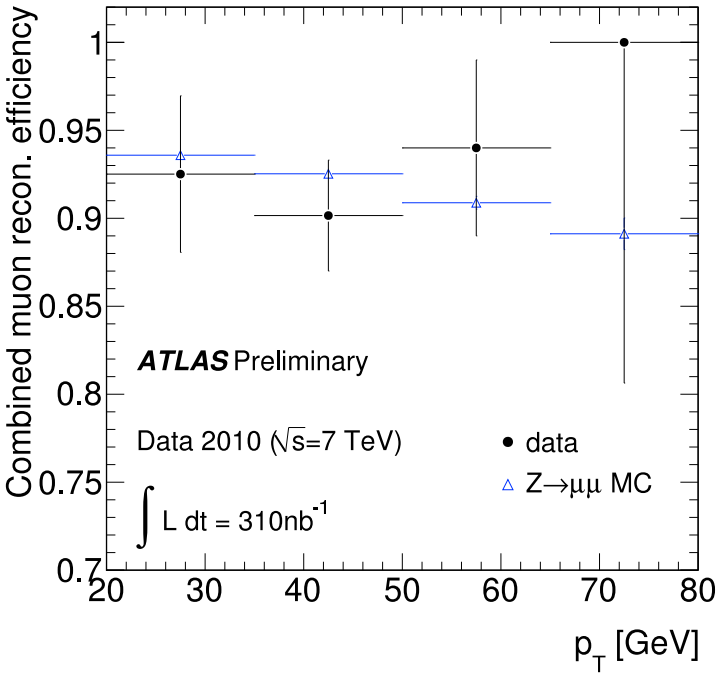

Figure 4.4. Tag and probe efficiency in data and simulation as a function of transverse momentum of the ID probe track.

this method had a relatively small systematic uncertainty mainly due to background contamination under the Z^0 peak, it was extremely statistically limited in $\sim$330 nb^{-1} (see Fig. 4.4). Thus, it was used as a cross check.

A second data-driven measurement of the reconstruction efficiency, called the "MS-hits" method, selected single isolated ID tracks and extrapolated them to the MS. Hits in the MDT chambers near the extrapolated ID track were assigned a significance, defined as the distance between the extrapolated track position and the MDT tube center divided by the sum in quadrature of the extrapolation error and the tube width/$\sqrt{12}$. The latter component encompassed the MDT hit uncertainty. Hits were associated to the track if their significance was less than 3.0. The ID track was chosen if it passed the following selection criteria:

- $p_T > 20$ GeV, $|\eta| < 2.4$, $|z_0| < 10$ mm with respect to primary vertex.

- At least 1 Pixel, 6 SCT and (if within TRT acceptance of $|\eta| < 1.9$) 10 TRT hits.

- At least two MDT layers each with a minimum of associated precision hits (minimum number of associated hits $N_{hits} = 4, 3, 3$ for the inner, middle and outer layers of the MS, respectively). The number of associated hits required in each layer correspond to half the number of expected hits for a muon traversing a given layer.

- Relative track isolation less than 0.2 within a cone size of $dR < 0.4$.

The combined reconstruction efficiency was then calculated by matching a selected ID track to a combined muon within a cone of $dR < 0.4$ around the ID track. The benefit of this second method in which only one muon is required was that there were many more events than for the tag-probe, as the data sample could contain other physics processes such as $W^{\pm} \to \mu\nu$.

However, without the Z^0 peak constraint to ensure that the muons found were "prompt" (coming from the interaction point), muons originating from light hadrons (such as pions and kaons) which decay outside the beam pipe could have contaminated the sample. This appeared as a false loss of efficiency, because the diverging path of the decay muon caused the ID-MS combination to fail while still passing the ID track requirements. To account for this non-prompt muon contamination, a template fitting technique was developed to determine the fraction of events from the initial hard scatter versus those from pion and kaon decays. Templates were created from distributions of hit residuals between the extrapolated ID track and the associated MDT hits. Simulated samples of $W^{\pm} \to \mu\nu$ and pion events were used to model the "prompt"-like and "decay"-like muon behavior in the detector, respectively. The fits of these samples to data are shown in Figure 4.5. The prompt-like fraction in data was found to be 0.793 ± 0.003 for ID track muons and 0.830 ± 0.003 for Staco combined

Table 4.4. Systematic uncertainties on the reconstruction efficiency scale factor calculation (MS-hits method).

Systematic Uncertainty	Value (%)
Non-prompt muon contamination	2.0
ID track efficiency	1.0
Selection stability and bias	0.6
MDT hit efficiency	0.3
Total	2.4

Table 4.5. Single muon reconstruction efficiency found in data and simulation and corresponding reconstruction efficiency scale factor for both the tag-probe and MS-hits method. The efficiency from simulation has negligible errors.

	Tag-probe	MS-hits
Data	0.933 ± 0.022 (stat) $\pm$ 0.013 (sys)	0.994 ± 0.006 (stat) $\pm$ 0.024 (sys)
Simulation	0.924	0.986
Scale Factor	1.010 ± 0.022 (stat) $\pm$ 0.013 (sys)	1.008 ± 0.006 (stat) $\pm$ 0.024 (sys)

muons, where the errors quoted were extracted from the fits. These fractions were used to correct the efficiency found using the MS-hits method.

The systematic uncertainties in this method are summarized in Table 4.4. Here, the largest uncertainty came from the calculation of the non-prompt muon contamination level. Also included were the ID track reconstruction efficiency uncertainty, the stability of the selection and the bias the selection introduced by only selecting ID tracks with hits, and the MDT hit efficiency which was the fraction of faulty MDT tubes that were not able to read out data.

The resulting single muon efficiency for both the MS-hits and the tag-probe methods are shown in Table 4.5. Note that the efficiencies found in data and simulation were different between the two methods. This was expected, as the tag-probe method did not inherently require MDT chambers as the MS-hits method had, and so acceptance gaps in the MS were folded into the tag-probe efficiency. However, both methods found consistent scale factors, which was ultimately the important cross-check.

Since there were two muons in each event, both of which could have been lost due to reconstruction inefficiency, the total dimuon efficiency is the square of the single

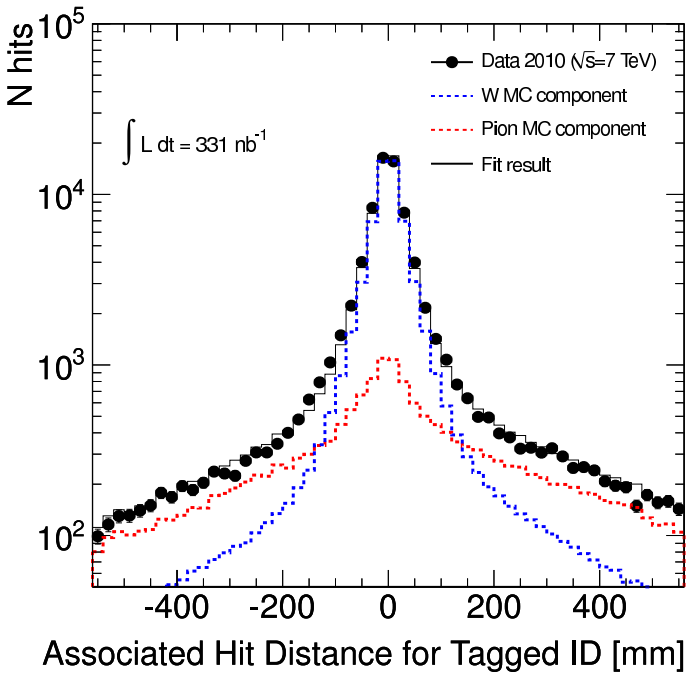

(a) Fit results for selected ID tracks

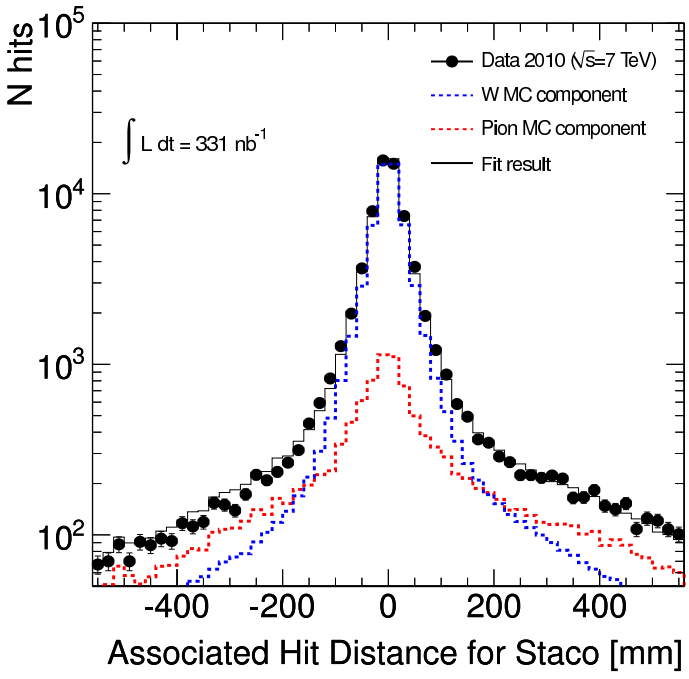

(b) Fit results for Staco muons

Figure 4.5. Results of fitting data hit residuals to prompt muon and decay in flight samples for ID tracks (top) and combined muons (bottom) with $p_T > 20$ GeV.

Table 4.6. Dimuon reconstruction efficiency for data and in simulation and scale factor for both the tag-probe and MS-hits methods.

	Tag-probe	MS-hits
Data	0.870 ± 0.041 (stat) ± 0.024 (sys)	0.988 ± 0.012 (stat) ± 0.048 (sys)
Simulation	0.854	0.972
Scale Factor	1.019 ± 0.041 (stat) ± 0.024 (sys)	1.016 ± 0.012 (stat) ± 0.048 (sys)

muon efficiency:

$$\epsilon_{\mu\mu} = \epsilon_{\mu}^2 \pm \delta\epsilon_{\mu\mu} \ , \quad \text{where} \ \ \delta\epsilon_{\mu\mu} = 2\epsilon_{\mu}\delta\epsilon_{\mu}. \tag{4.3}$$

The final values for the dimuon reconstruction efficiency in data and simulation are listed in Table 4.6.

Because the scale factors for both the tag-probe and MS-hits methods were consistent with each other and consistent with 1, a correction was not applied to C_Z for any reconstruction efficiency simulation-data discrepancy. However, the uncertainties were still used in the final calculation, and since the MS-hits method had a smaller total uncertainty, the final reconstruction scale factor for dimuons was then defined as

$$SF_{reco} \ = \ 1.000 \ \pm \ 0.012 \ \text{(stat)} \ \pm \ 0.048 \ \text{(sys)} \ . \tag{4.4}$$

4.6.2 Trigger Efficiency Scale Factor

The trigger efficiency for `L1_MU6` was determined in data by looking for reconstructed muon events in an orthogonal trigger; that is, another non-muon trigger system in ATLAS which had also saved the event. The orthogonal trigger in this analysis was `L1_J15`, which used calorimeter information to accept events with jets having $E_T > 15$ GeV. This was the lowest-energy un-prescaled jet trigger. Combined muons were then matched to geometric Region of Interests (RoI) above an inclusive p_T threshold. If a RoI not associated to a muon in an event was accepted by `L1_J15`, this resulted in a loss of efficiency.

The events and muons for this study were selected in a very similar way as described in section 4.4. This selection is listed in Table 4.7.

Since the trigger detector technology is different in the barrel (RPC) and the endcap (TGC), the trigger efficiency measurement was divided into regions with $|\eta|$ less than and greater than 1.05 (barrel and endcap, respectively). The efficiencies for single muons to pass a trigger in data and in simulation (using a $W^{\pm} \to \mu\nu$ sample) are given in Table 4.8 for the two detector regions. There was less of a discrepancy between data and simulation in the barrel region, as the simulation samples used for this analysis had included calibration with known RPC timing issues, while the TGC efficiency in the endcaps was optimistic (see Fig. 4.6).

The largest systematic uncertainties in determining the muon trigger efficiency in data were an uncertainty arising from algorithm dependence (Staco required a trigger-hit in reconstruction while Muid did not, and the relative difference in measured efficiency was taken as the uncertainty) and an uncertainty on the p_T threshold chosen. Also included were uncertainties arising from muon-to-RoI matching criteria, the size of the RoI search range, and the difference in $|\eta|$ distributions between muons from $W^{\pm}/Z^0$ decays and those from heavy flavor decays (the latter having a much higher yield in this analysis).

Table 4.7. Event and muon selection for trigger efficiency study.

Event Selection	
Primary Vertex	N_{vtx} with $n_{tracks} \geq 3$
	$\lvert z_{vtx}\rvert < 150$ mm
Trigger	`L1_J15`
Muon Selection	
Muon Selection	Combined muon with
	$p_T > 20$ GeV, $\lvert\eta\rvert < 2.4$
Muon Quality	$p_T^{MS} > 10$ GeV
	$\lvert p_T^{MS} - p_T^{ID}\rvert < 15$ GeV
	$\lvert z_0\rvert < 10$ mm wrt PV

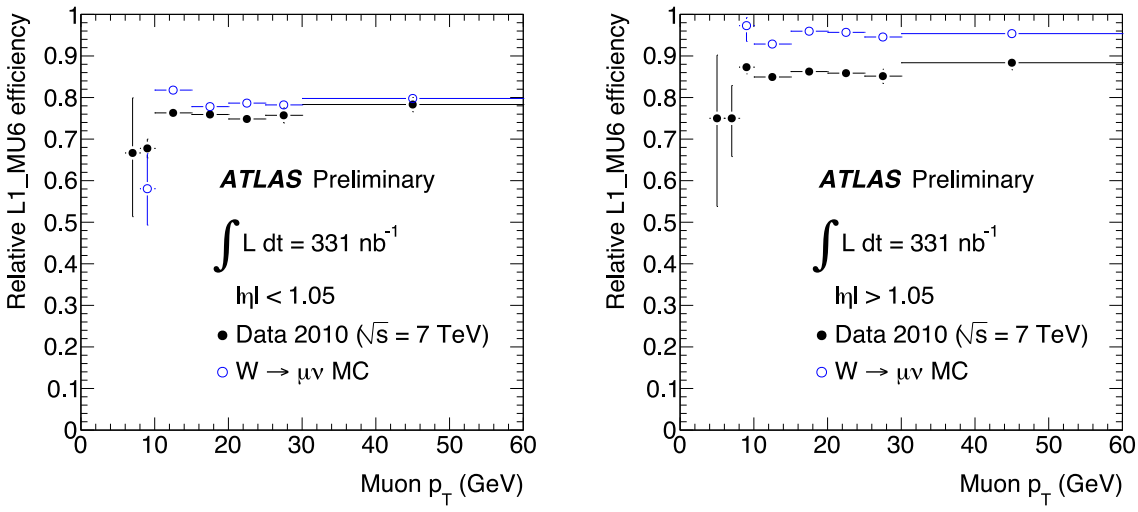

Figure 4.6. L1_MU6 trigger efficiency as a function of muon p_T comparing simulation and data for the barrel (left) and endcap (right) regions.

Because there are two chances for the trigger to accept an event having two muons, the trigger efficiency ($\epsilon_{\mu\mu}$) and uncertainty ($\delta\epsilon_{\mu\mu}$) for a dimuon event is given by:

$$\begin{aligned} \epsilon_{\mu\mu} &= 1-(1-\epsilon_{\mu 1})(1-\epsilon_{\mu 2}), \\ \text{where } \delta\epsilon_{\mu\mu} &= (1-\epsilon_{\mu 1})\delta\epsilon_{\mu 1}+(1-\epsilon_{\mu 2})\delta\epsilon_{\mu 2}\ . \end{aligned} \tag{4.5}$$

Note that the efficiency of the two individual muons ($\epsilon_{\mu 1}$ or $\epsilon_{\mu 2}$) can be different. The efficiency in the barrel and endcap were treated separately, and so dimuon events were split into 3 categories: events where both muons were in the barrel (BB), events with one muon in the barrel and one in the endcap (BE) and events with both muons

Table 4.8. Efficiencies for a single muon to trigger an event in two regions of the detector. The barrel region is covered by RPCs, while the endcap region is covered by TGCs.

	Barrel	Endcap
Data	0.760 ± 0.009 (stat) ± 0.020 (sys)	0.863 ± 0.008 (stat) ± 0.018 (sys)
Simulation	0.792 ± 0.003 (stat)	0.951 ± 0.002 (stat)

Table 4.9. Dimuon muon trigger efficiencies where both muons passed through the barrel, the endcap, or where one muon passed through the barrel and the other through the endcap (BB, EE and BE respectively).

Configuration	Data	Simulation
BB	0.942 ± 0.004 (stat) ± 0.010 (sys)	0.956 ± 0.001 (stat)
EE	0.981 ± 0.002 (stat) ± 0.005 (sys)	0.998 ± 0.000 (stat)
BE	0.967 ± 0.003 (stat) ± 0.007 (sys)	0.990 ± 0.001 (stat)

Table 4.10. Total dimuon trigger efficiency in data and simulation.

	Efficiency
Data	0.963 ± 0.003 (stat) ± 0.006 (sys)
Simulation	0.982 ± 0.001 (stat)

in the endcap (EE). Table 4.9 lists the dimuon efficiencies found in each category after using the values in Table 4.8 as inputs into Eq. (4.5).

The fraction of dimuon events passing all selection *except* for the trigger requirement in each barrel-endcap combination was found from simulation (29%, 23% and 48% for BB, EE and BE, respectively). Each efficiency in Table 4.9 was weighed by the fraction of events found in each category, and the total efficiency in data and simulation is shown in Table 4.10.

Finally, this gave a trigger efficiency scale factor of:

$$SF_{trig} = 0.981 \ \pm \ 0.003 \text{ (stat)} \ \pm \ 0.006 \text{ (sys)} \ . \tag{4.6}$$

4.6.3 Final C_Z Acceptance Value

The systematic uncertainties for the scale factor corrections to C_Z have already been discussed in the previous two sections. To summarize, the values of the dimuon reconstruction and trigger scale factors to correct C_Z were:

$$\text{Reconstruction efficiency SF} = 1.000 \ \pm \ 0.012 \text{ (stat)} \ \pm \ 0.048 \text{ (sys)},$$

$$\text{Trigger efficiency SF} = 0.981 \pm 0.003 \text{ (stat)} \ \pm \ 0.006 \text{ (sys)}.$$

In addition, the impact of data-simulation discrepancies of the muon momentum scale, momentum resolution, and isolation selection also contributed to the overall systematic uncertainty on C_Z. The effect of the muon momentum scale and resolution was found by fitting the shape of the Z^0 peak with a Breit-Wigner function convoluted with a Gaussian resolution distribution in both data and the simulated $Z \to \mu\mu$ samples. In the simulated samples, both the mean (via muon p_T scaling) and the width (via muon p_T smearing) were recalculated with different scale and smearing values. Figure 4.7 shows the mean and width fits to data ($\pm 1\sigma$) overlaid with an interpolation between the different recalculated mean and width values found in the simulated sample. The total range of the mean and width of the Gaussian in simulation after additional scaling and smearing was taken as a systematic uncertainty for the momentum scale and resolution, respectively. The momentum scale uncertainty was found to be 1.0% per muon. The effect of muon resolution was found separately for barrel-barrel, endcap-endcap and barrel-endcap muon pairs, and the single muon resolution was found to be 5% and 9% for muons in the barrel and endcap regions, respectively. The effect of both momentum scale and resolution uncertainties generated an overall uncertainty of 0.7% on C_Z. A 1.0% isolation uncertainty was assigned per muon using a tag-probe approach on isolated and non-isolated muon tracks.

The final value of C_Z after applying these scale factors and including systematic uncertainties was found to be:

$$C_Z = 0.773 \pm 0.043 \text{ (stat+sys)} .$$

4.7 Result

The number of expected events for the dominant backgrounds after selection and after applying the scale factors from the previous section are summarized in Table 4.11. For the $b\bar{b}$ and $c\bar{c}$ backgrounds, a conservative systematic uncertainty corresponding to 100% was applied. All other backgrounds, including $W^{\pm} \to \mu\nu$, $Z \to \tau\tau$

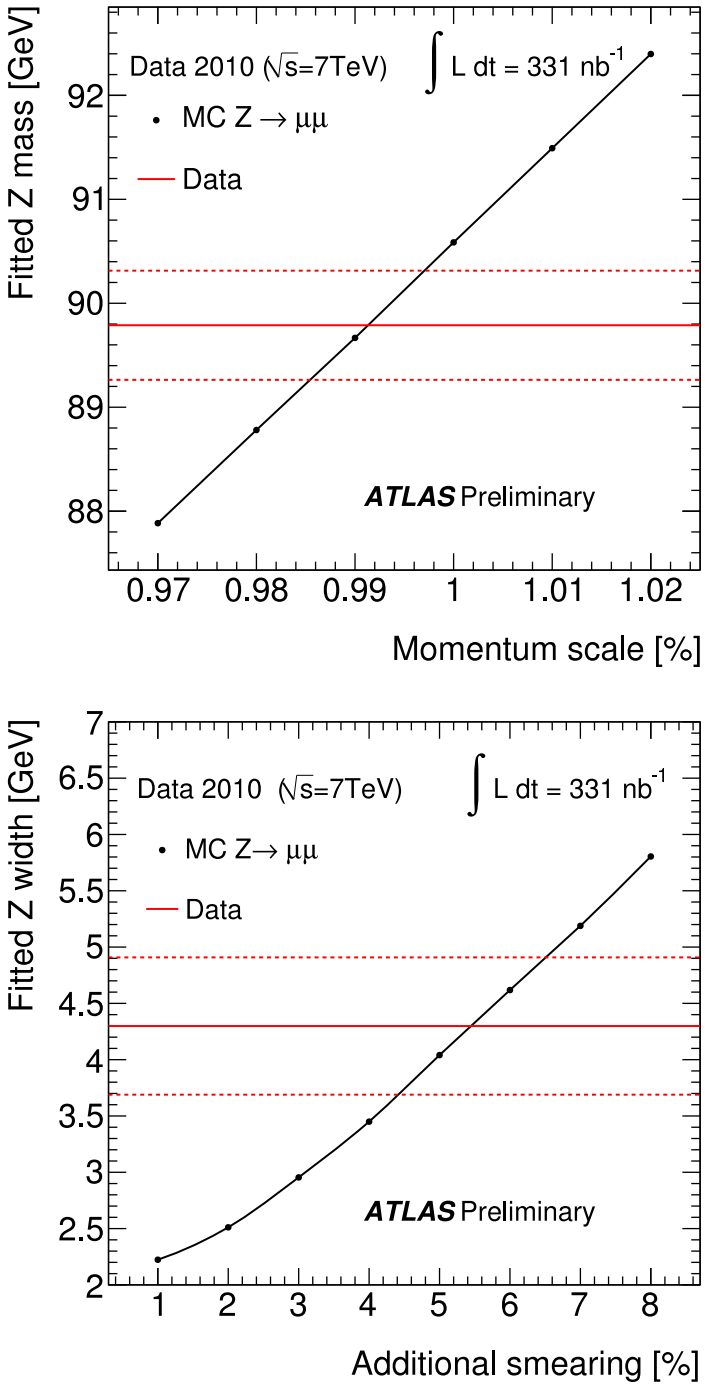

Figure 4.7. Muon momentum scaling (top) and extra smearing (bottom) in simulation for combined muons, shown as a black curve. The central value found in data is represented by a solid red line with the statistical error window bounded by the red dotted lines.

Table 4.11. Number of expected events for background processes normalized to 331 nb^{-1}.

Process	Expected Events
$W^{\pm} \to \mu\nu$	0.013 ± 0.003 (stat) ± 0.001 (sys) ± 0.001 (lumi)
$Z \to \tau\tau$	0.086 ± 0.004 (stat) ± 0.007 (sys) ± 0.010 (lumi)
$t\bar{t}$	0.107 ± 0.004 (stat) ± 0.010 (sys) ± 0.012 (lumi)
$b\bar{b}$, $c\bar{c}$	0.038 ± 0.015 (stat) ± 0.038 (sys) ± 0.004 (lumi)

Table 4.12. Summary of values included in the $Z \to \mu\mu$ cross section measurement.

Luminosity	331 ± 35 nb^{-1}
Events Observed	109
Background Events Expected	0.244 ± 0.016 (stat) ± 0.055 (sys) ± 0.027 (lumi)
Acceptance A_Z	0.486 ± 0.019 (stat+sys)
Correction C_Z (corrected)	0.773 ± 0.043 (stat+sys)

and $t\bar{t}$ decays in the dimuon channel were also predicted from simulation. Systematic uncertainties included a 3% PDF uncertainty for these three processes, a 5% uncertainty on the theoretical cross section for $W^{\pm} \to \mu\nu$ and $Z \to \tau\tau$, and a 6% theoretical uncertainty on the $t\bar{t}$ cross section. The luminosity uncertainty was 11% at the time this analysis was performed [82].

Table 4.12 shows all inputs used in the cross section calculation in Eq. (4.2). The final cross section times branching fraction for the Z^0 boson decay into muons within $66 < M_{\mu\mu} < 116$ GeV was:

$$\sigma_{Z\to\mu\mu} = 0.87 \pm 0.08\ (\text{stat}) \pm 0.06\ (\text{sys}) \pm 0.10\ (\text{lumi})\ \text{nb}. \qquad (4.7)$$

Since the true acceptance had been separated from the selection and detector acceptance, the cross section in the fiducial region was:

$$\sigma^{fid}_{Z\to\mu\mu} = 0.43 \pm 0.04\ (\text{stat}) \pm 0.02\ (\text{sys}) \pm 0.05\ (\text{lumi})\ \text{nb}.$$

This measurement was also performed in the dielectron channel using 316 nb^{-1} of data [81], which found $\sigma_{Z\to ee} = 0.75 \pm 0.09\ (\text{stat}) \pm 0.08\ (\text{sys}) \pm 0.08\ (\text{lumi})$ nb. Combining the muon and electron channels yields an average dilepton cross section of:

$$\sigma_{Z\to ll} = 0.82 \pm 0.06\ (\text{stat}) \pm 0.05\ (\text{sys}) \pm 0.09\ (\text{lumi})\ \text{nb}.$$

The NNLO theoretical prediction of the cross section including the MSTW2008 PDF set was:

$$\sigma^{theory}_{Z\to ll} = 0.96 \pm 0.05\ (\text{sys})\ \text{nb}$$

(see Fig. 4.8). Here, a theoretical systematic uncertainty of 5% was applied, which was estimated using the MSTW2008 NNLO PDF error eigenvectors at the 90% C.L. limit, as well as varying the range of α_s in the range 0.1145 to 0.1176 and the nominal renormalization and factorization scales (both set to m_Z) by a factor of two. Figure 4.9 displays cross sections measured at previous $p\bar{p}$ collider experiments as a function of $\sqrt{s}$, and shows that the ATLAS measurement agrees with the theoretical prediction at $\sqrt{s} = 7$ TeV.

Now that the $Z \to \mu\mu$ cross section has been measured and the first studies of DY production in ATLAS have been performed at $\sqrt{s} = 7$ TeV, we move on to search for new physics in the high-mass tail of the dimuon spectrum. The remaining chapters of this thesis describe the search for $qq\mu\mu$ contact interactions with the full 2010 dataset.

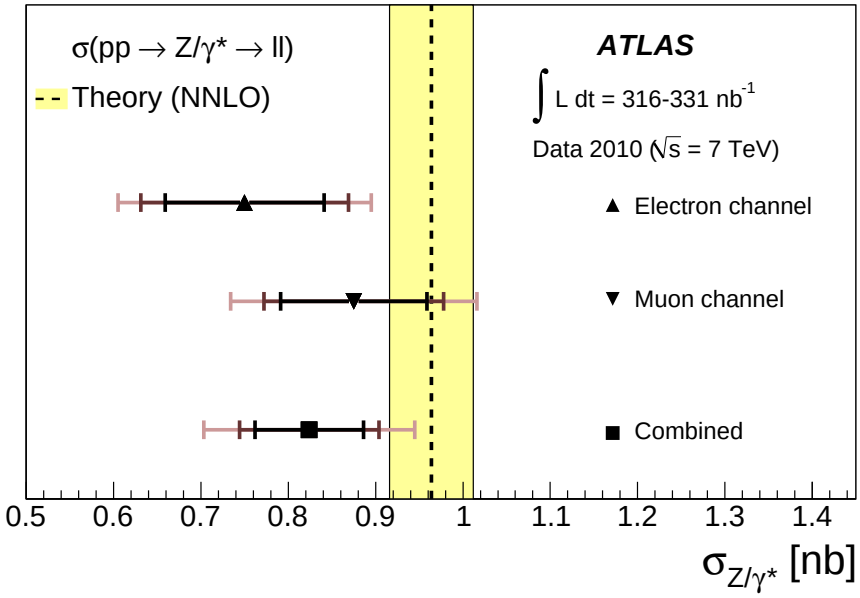

Figure 4.8. $Z \to ll$ cross sections for the electron, muon and the combination compared to the theoretical predictions. The error bars represent the statistical, the statistical plus systematic and the total uncertainty including luminosity. Uncertainties are added in quadrature.

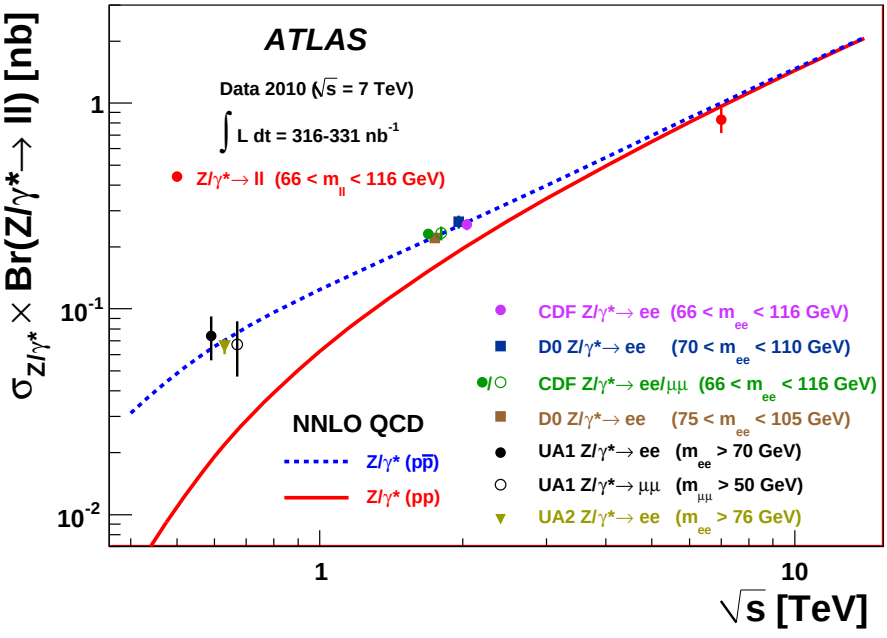

Figure 4.9. $Z \to \mu\mu$ cross section shown as a function of $\sqrt{s}$. The value shown for the ATLAS measurement is the combination of electron and muon channels.

CHAPTER 5

SEARCH FOR CONTACT INTERACTIONS WITH DIMUONS

This chapter describes the data collected in 2010, paying close attention to the first muon performance studies. Corrections made to both signal and background simulated samples are discussed, which account for higher-order processes contributing to the theoretical cross section calculation and better knowledge of the detector performance.

5.1 The 2010 Dataset

The LHC began its $\sqrt{s} = 7$ TeV collision physics program in March 2010, and ended its first pp run in October 2010 in order to switch to heavy ion collisions for the rest of the year. Over 8 months, the LHC delivered a total of 49 pb^{-1} of pp collisions with stable beams, reaching a maximum peak instantaneous luminosity of 2.07×10^{32} cm^{-2} s^{-1} on October 24$^{\text{th}}$. During the 2010 run period, ATLAS recorded a total of 45 pb^{-1} of data with a luminosity uncertainty of 3.4% [83]. Figure 5.1 shows the total integrated luminosity and the instantaneous luminosity in 2010. The contact interaction analysis uses the full 2010 dataset, corresponding to 42 pb^{-1} of data after requiring a GRL containing luminosity blocks with baseline data quality selection as outlined in section 2.5.

Figure 5.2 shows the invariant mass distribution of dimuons in the full 2010 dataset [84]. The J/ψ, Υ and Z^0 particles are shown, reaffirming the Standard Model production at $\sqrt{s} = 7$ TeV.

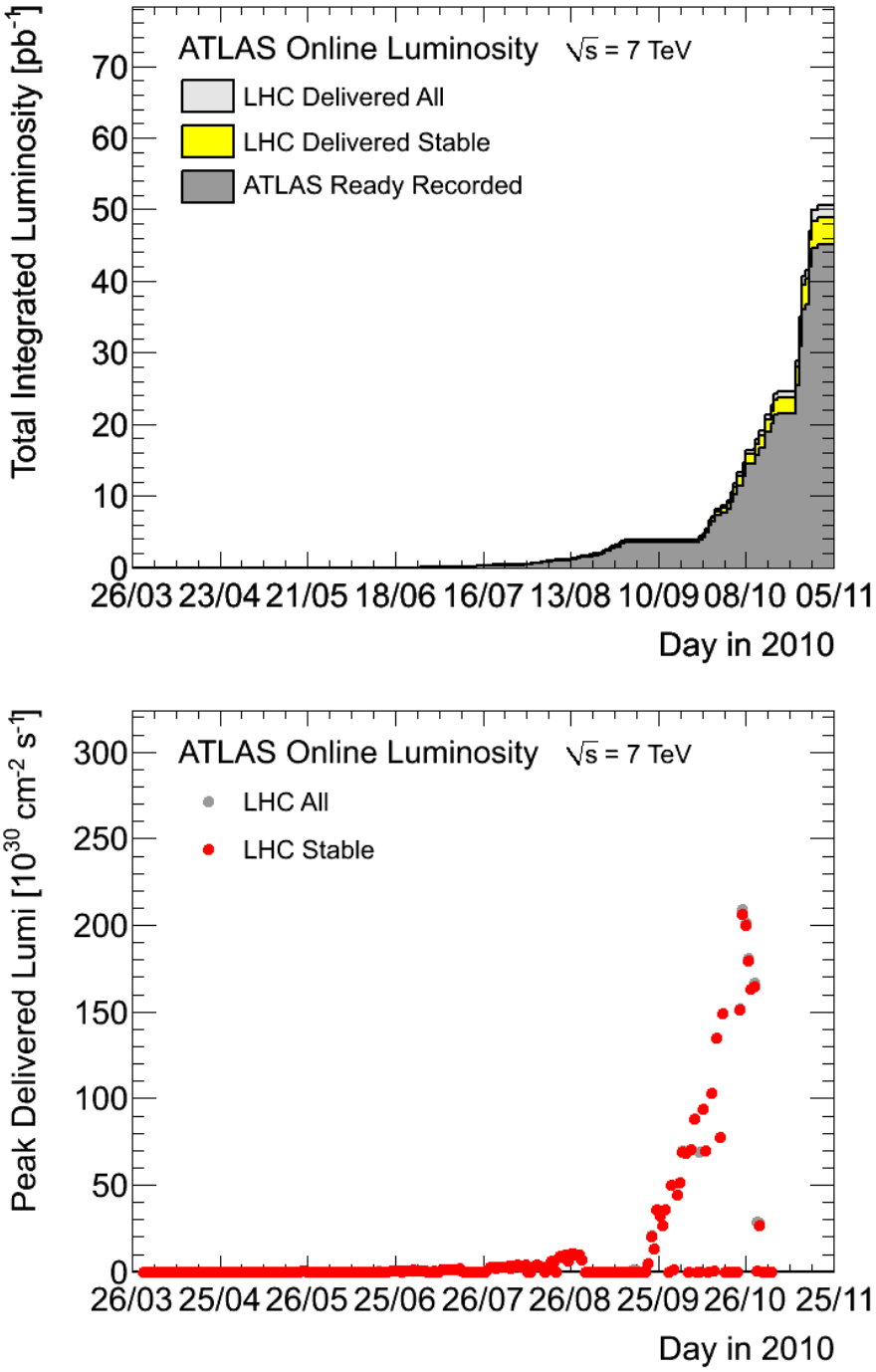

Figure 5.1. Total integrated luminosity (top) and instantaneous luminosity (bottom) of *pp* collisions delivered each day by the LHC in 2010.

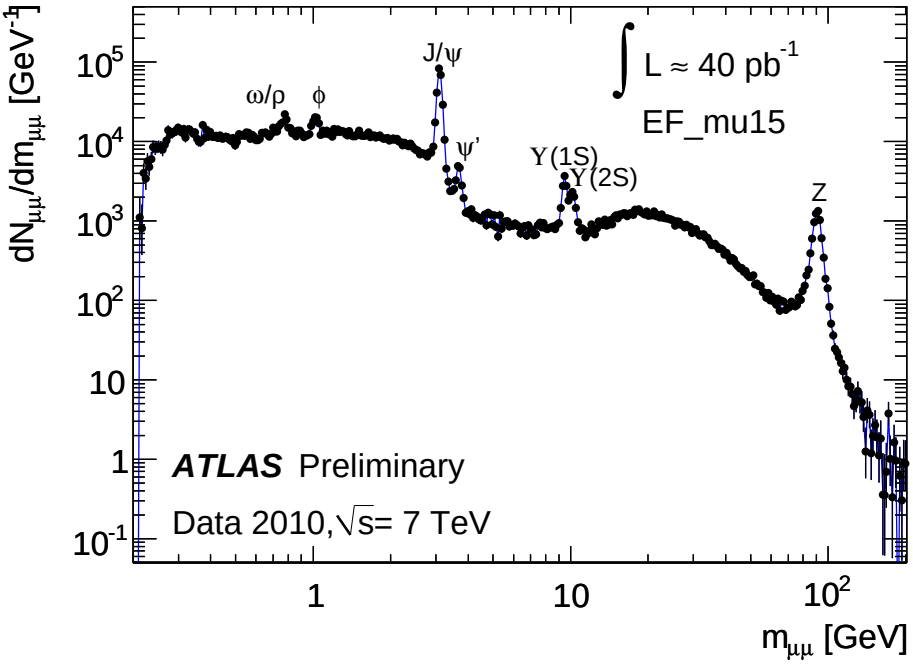

Figure 5.2. Opposite sign dimuon invariant mass in the full 2010 dataset.

The data was reprocessed after calibration, alignment constants and software updates were included based on earlier data analyses. In addition, the $Z \to \mu\mu$ invariant mass distribution was used to determine the performance of the MS. Efficiency and resolution studies, while described in more detail in [76, 85], are summarized below.

5.1.1 Muon Efficiency

Because muons are measured independently in both the ID and MS, the tag and probe method (as introduced in section 4.6.1) was used to measure the efficiency of one detector with respect to the other. The combined muon reconstruction efficiency is measured in regions of $\eta-\phi$ space, corresponding to the detector regions in Fig. 2.15. The combined efficiency is factorisable:

$$\varepsilon_{CB} = \varepsilon_{ID} \times \varepsilon_{MS} \times \varepsilon_{match}, \tag{5.1}$$

where ε_{ID} is the ID reconstruction efficiency, ε_{MS} is the extrapolated MS track reconstruction efficiency and ε_{match} is the matching efficiency between the MS and ID. A combined muon is used for the tag, and the probe can either be a muon ID track if measuring ε_{MS} or ε_{match}, or an extrapolated MS track if measuring ε_{ID}. The efficiency is then the fraction of probes associated to a CB track of the same charge within a cone of $dR < 0.01$ (0.05) for ID (extrapolated MS) track probes, if the invariant mass of the tag/probe pairs is within 10 GeV of the Z^0 mass. The combined efficiency is shown in Fig. 5.3 as a function of p_T and η in both data and simulation. The drop of efficiency at $\eta \simeq 0$ is expected due to the limited MS chamber coverage in that region to make room for power and read-out services.

In momentum, the scale factor ratio of data to simulation remains roughly constant up to ∼100 GeV. Beyond that, an uncertainty needed to be applied to the simulation prediction of efficiency.

5.1.2 Muon Resolution

The simulation describes the performance of a nominally calibrated and aligned ATLAS detector, which corresponds to a 10% momentum resolution at 1 TeV. In the earliest data, however, this is not the case, as can be seen in Fig. 4.3 where the Z^0 peak in data is broader than in simulation.

After the first data was collected with preliminary alignment and calibration constants, a study of momentum resolution was performed by fitting the Z^0 peak. The resolution relative to the muon track momentum is given by:

$$\frac{\sigma(p_T)}{p_T} = \frac{S_0^{MS}}{p_T} \oplus S_1^{MS} \oplus S_2^{MS} p_T, \tag{5.2}$$

where the first term parameterizes the muon energy loss in the calorimeter, the second term parameterizes the multiple scattering term in the MS, and the last term parameterizes the intrinsic resolution due to mis-measurements of the track sagitta.

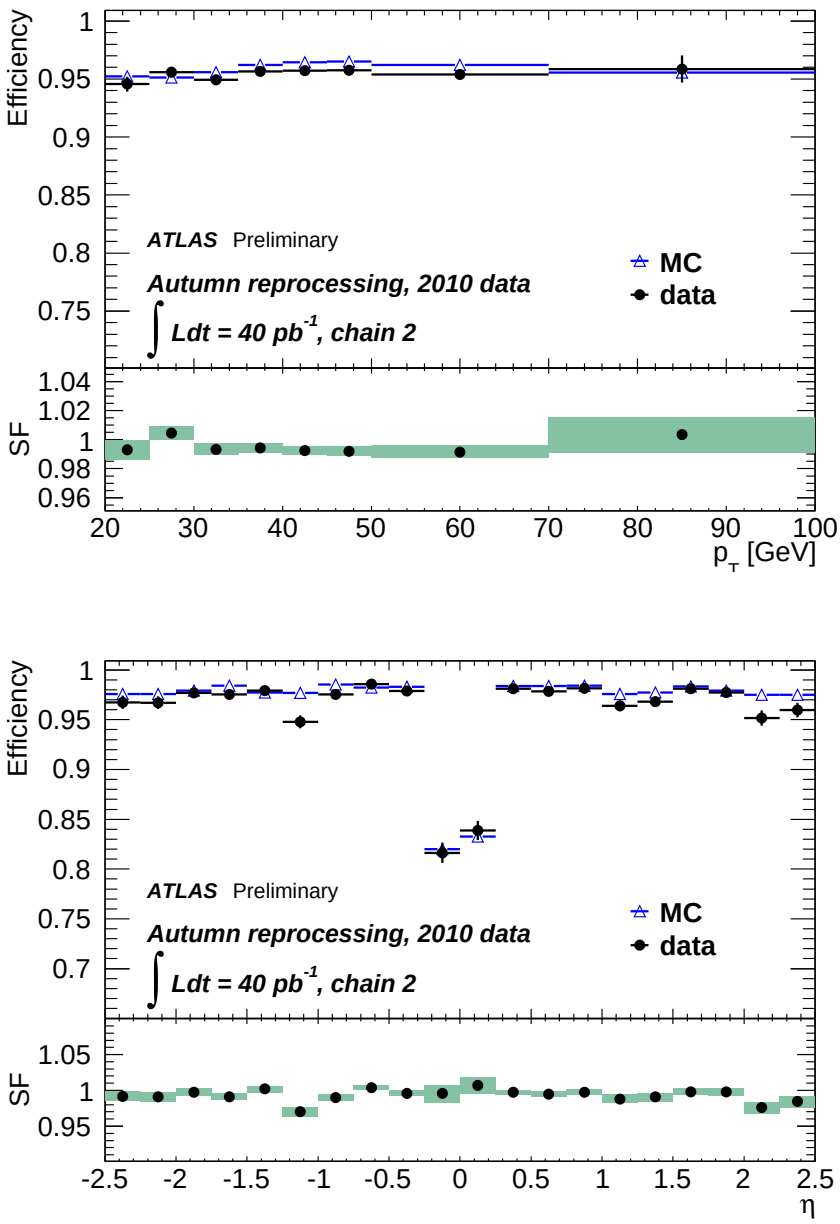

Figure 5.3. Muid combined muon reconstruction efficiency as a function of p_T (top) and η (bottom). Scale factor ratios of data to simulation are shown at the bottom of each figure.

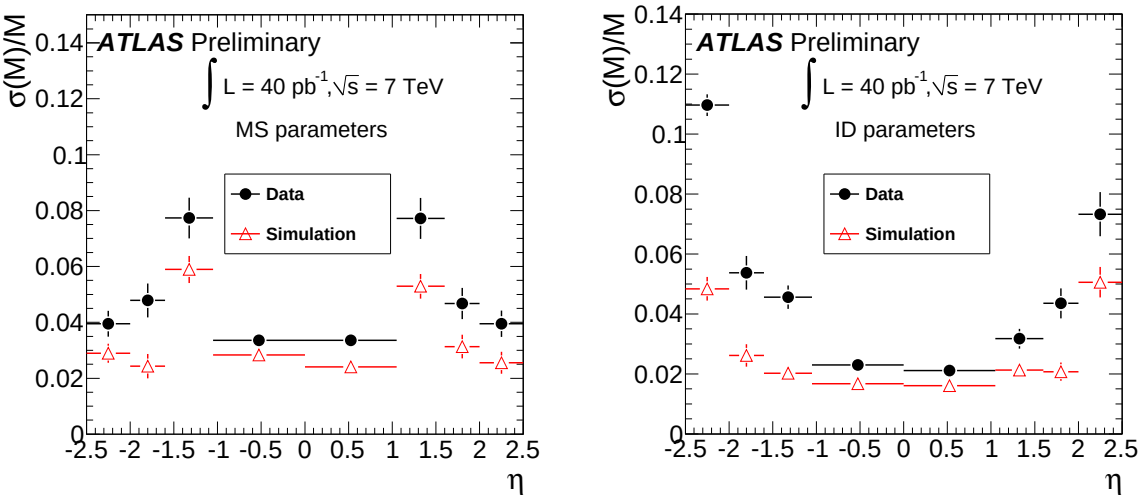

Figure 5.4. Z mass resolution as a function of η for the MS (left) and the ID (right).

Both $Z \to \mu\mu$ and $W^{\pm} \to \mu\nu$ processes were used to measure the muon momentum resolution. The mass resolution from the Z width $\sigma(m_{\mu\mu})$ is shown in Fig. 5.4 for the invariant mass measured in the MS and ID as a function of track η. The discrepancy between data and simulation in the ID resolution had an asymmetry between the A and C sides of the detector. This was determined to be an issue with the ID alignment constants used in the reconstruction, and was fixed in the 2010 data reprocessing [86]. In the MS, the resolution was poorer in the transition region where the magnetic field bending power is weaker.

These discrepancies were also visible in the relative momentum resolution:

$$\rho_{rel} = \frac{p_{ID} - p_{MS}}{p_{ID}}. \tag{5.3}$$

Distributions in four detector regions comparing data with the simulated $W^{\pm} \to \mu\mu$ sample are shown in Fig. 5.5, where the resolution in the pre-aligned and calibrated data is shown to rise as a function of momentum. After performing these studies, the simulation-data agreement improved after the full 2010 reprocessing of the data. Figure 5.6 shows the improvement in the Z^0 peak resolution after the data reprocessing.

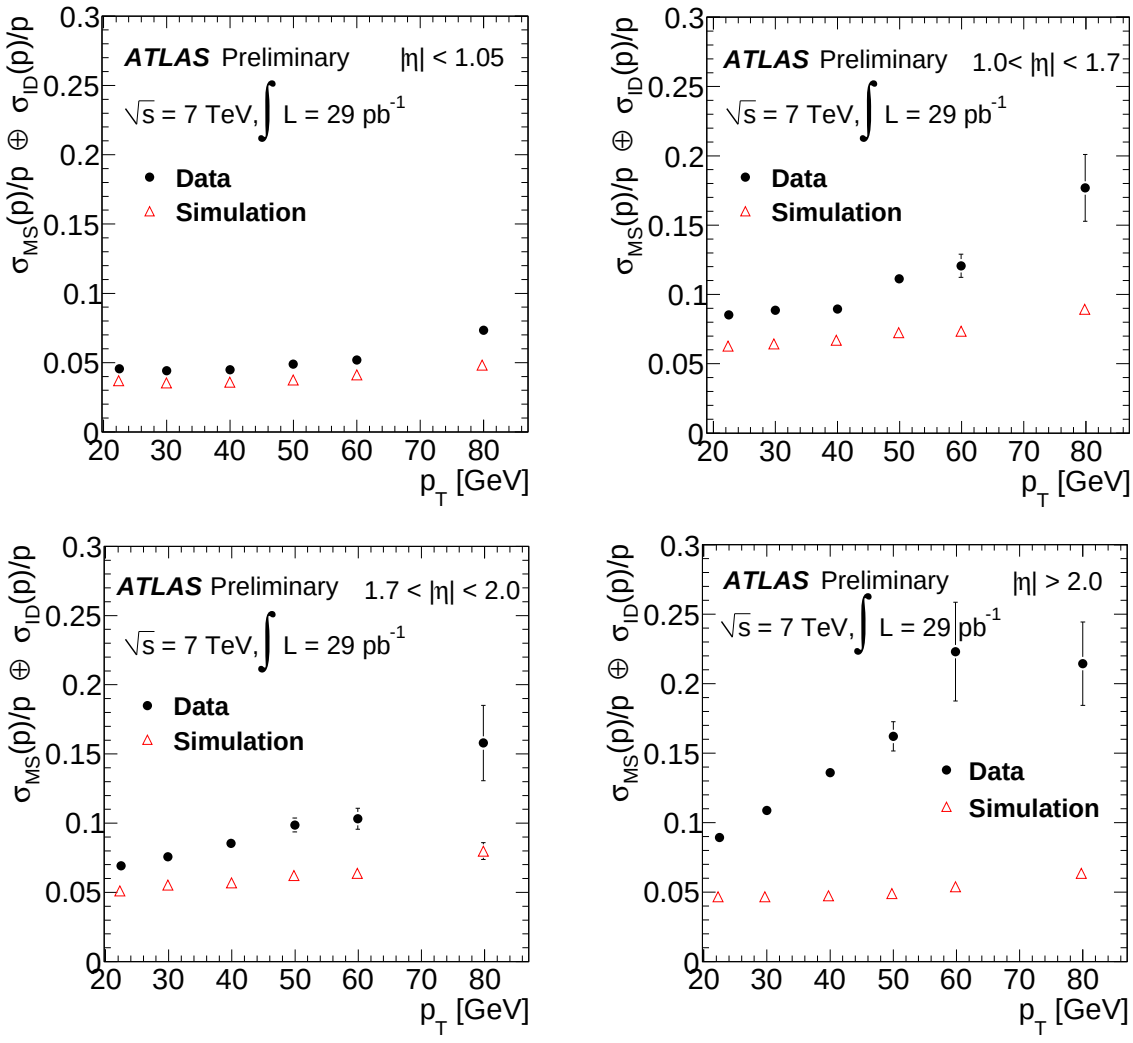

Figure 5.5. Relative resolution ρ_{rel} in the barrel (top left), transition (top right), MDT endcap (bottom left) and CSC (bottom right) regions, comparing the nominal values in simulation to the measured values in data.

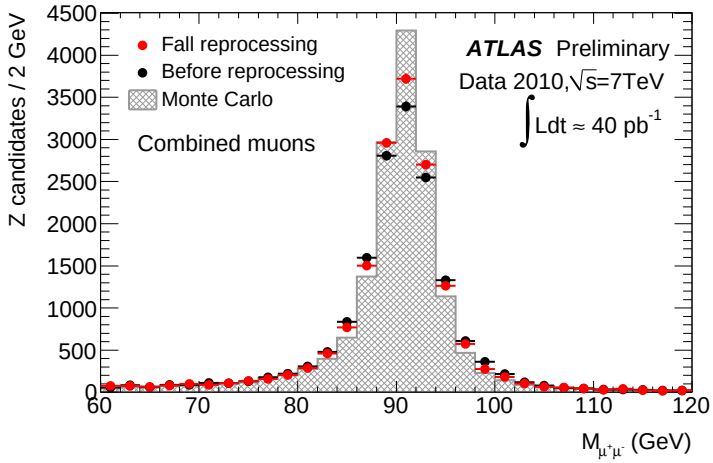

Figure 5.6. Distribution of dimuon invariant mass in data before and after reprocessing, compared to the nominal distribution from simulation.

5.2 Corrections to the Simulated Samples

After the muon reconstruction was studied in data as discussed in the previous section, the information gained about the muon performance was used to correct the simulation distributions in order to form a better agreement with the data. In addition, theoretical corrections were made to account for higher order processes. Both theoretical and detector-related corrections become important when extrapolating to the dimuon high-mass tail, where only simulation can be relied upon to predict the shape of the invariant mass spectrum. The following sections detail the procedures for making these corrections on an event- and muon-level basis.

5.2.1 Theoretical Cross Sections

As previously stated in Chapter 3, the $Z \to \mu\mu$ and CI simulation samples were produced with LO matrix elements and a modified LO PDF set in the production cross section calculation. However, higher-order processes can not only enhance the cross section, but can destructively interfere with the leading order processes as well. Some examples of higher-order diagrams are shown in Fig. 5.7. Taking these higher-order processes into account significantly reduced the theoretical cross section uncertainty.

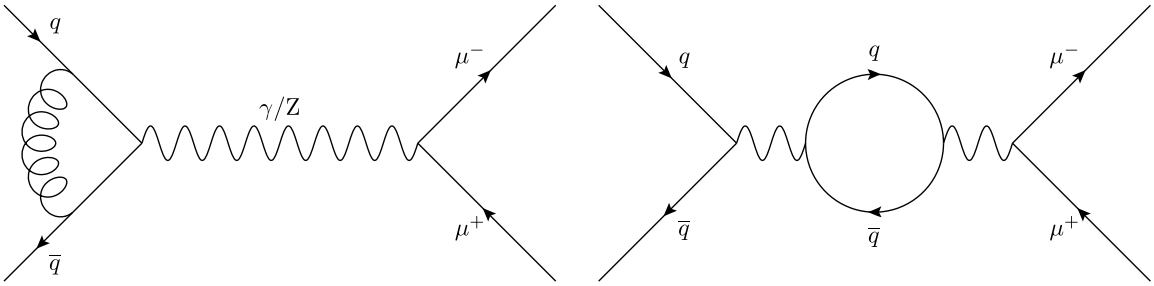

Figure 5.7. Examples of higher order diagrams in DY production. The left is an example of a vertex correction, while the right is an example of a correction to the propagator.

The ratio of the cross section for these higher-order processes up to NNLO to the LO cross section is known as the "K-factor", and was applied as a correction on an event-by-event basis to the DY interaction. The K-factor is defined by taking the ratio of cross sections from the primary hard scattering ($\sigma_{\mathrm{NNLO}}/\sigma_{\mathrm{LO}}$) using the higher order PDF sets.

Higher-order processes were divided into two categories: those involving QCD interactions and those involving EW interactions. QCD processes, such as gluon radiation or quark/gluon loops, are only able to affect the initial-state quarks in DY or DY+CI production. The PDF distributions are also affected by these higher-order QCD processes. The QCD K-factor ($\mathrm{K_{QCD}}$) numerator was determined from PHOZPR [87] for the NNLO matrix element using the MSTW2008NNLO PDF set:

$$K_{\mathrm{QCD}} = \frac{\sigma_{\mathrm{NNLO}} \times \mathrm{PDF}(\textsc{mstw2008nnlo})}{\sigma_{\mathrm{LO}} \times \mathrm{PDF}(\textsc{mrst2007lo*})} \ . \tag{5.4}$$

The K_{QCD} values along with their corresponding uncertainties are shown in Table 5.1, where the uncertainty in the K_{QCD} ratio grows from ~3% at the Z^0 peak to 6% at 1 TeV. Fitting the values as a function of invariant mass, the differential $\mathrm{K_{QCD}}(m_{\mu\mu})$ became:

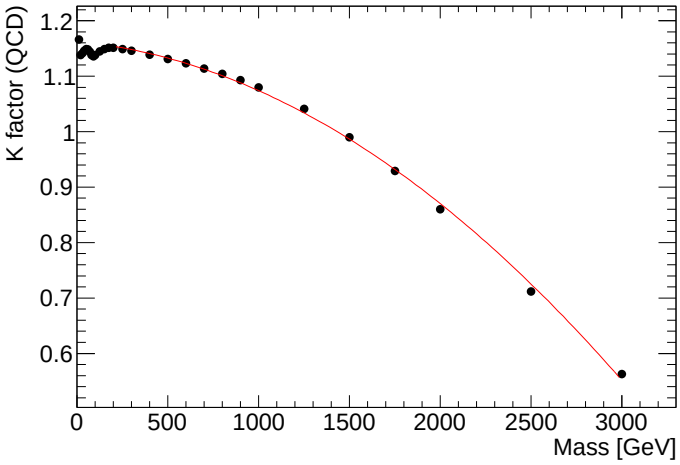

Figure 5.8. Fit to the differential QCD K-factor as a function of true dimuon mass.

$$\mathrm{K_{QCD}}(m_{\mu\mu}) = \begin{cases} 1.16, & \text{for } m_{\mu\mu} \leq 172 \text{ GeV} \\ 1.16 - (3.11 \times 10^{-5}) \times m_{\mu\mu} & \\ \quad - (5.75 \times 10^{-8}) \times (m_{\mu\mu})^2, & \text{for } m_{\mu\mu} > 172 \text{ GeV} \end{cases} \tag{5.5}$$

Electroweak corrections to the DY process for this analysis included contributions from virtual EW loop corrections, initial state photons (either radiation or loops which could have affected the PDF distributions) and final-state photon radiation. The last of these was properly accounted for in simulation using PHOTOS as discussed in section 1.4, so the FSR contribution needed to be excluded from the final EW K-factor ($\mathrm{K_{EW}}$) correction to simulation. To do this, $\mathrm{K_{EW}}$ was determined from two ratios:

$$\mathrm{K_{EW}} = \frac{\sigma_{\mathcal{O}(\alpha)} \text{ with full NNLO PDF}}{\sigma_{LO} \text{ with LO}^* \text{ PDF and FSR}} \times \frac{\sigma_{\mathcal{O}(\alpha)} \text{ with ISR only}}{\sigma_{\mathcal{O}(\alpha)} \text{ with full NNLO PDF}}, \tag{5.6}$$

where the first ratio accounted for the virtual EW loop corrections, and the second included the corrections to the proton structure from initial state photons. The $\mathcal{O}(\alpha)$

Table 5.1. The NNLO differential production cross section, along with the $K_{\rm QCD}$ values and the uncertainties in the $K_{\rm QCD}$ ratio due to NNLO PDF uncertainties at 90% C.L.

$M_{\ell\ell}$ [GeV]	$M_{\ell\ell}^2 \frac{{\rm d}\sigma_{\rm NNLO}}{{\rm d}M_{\ell\ell}^2}$ [nb]	$\frac{\sigma_{\rm NNLO}}{\sigma_{\rm LO}}$	Δ_r [%]
	MSTW	MSTW/MRST	PDF uncert.
	2008NNLO	2008NNLO/2007LO*	90% C.L.
10	0.465E+01	1.166	9.3
20	0.917E+00	1.138	4.5
30	0.327E+00	1.142	3.7
40	0.154E+00	1.146	3.5
50	0.884E-01	1.149	3.4
60	0.633E-01	1.148	3.3
70	0.665E-01	1.144	3.3
80	0.155E+00	1.138	3.3
91.12	0.113E+02	1.136	3.3
100	0.236E+00	1.138	3.2
125	0.207E-01	1.145	3.2
150	0.784E-02	1.149	3.1
175	0.405E-02	1.151	3.2
200	0.239E-02	1.151	3.2
250	0.104E-02	1.149	3.3
300	0.528E-03	1.146	3.4
400	0.179E-03	1.139	3.6
500	0.750E-04	1.131	3.9
600	0.357E-04	1.123	4.1
700	0.185E-04	1.114	4.4
800	0.101E-04	1.104	4.6
900	0.582E-05	1.093	5.0
1000	0.346E-05	1.080	5.4
1250	0.105E-05	1.041	6.7
1500	0.353E-06	0.990	8.8
1750	0.127E-06	0.929	11.6
2000	0.473E-07	0.860	15.3
2500	0.687E-08	0.712	24.8
3000	0.949E-09	0.563	35.4

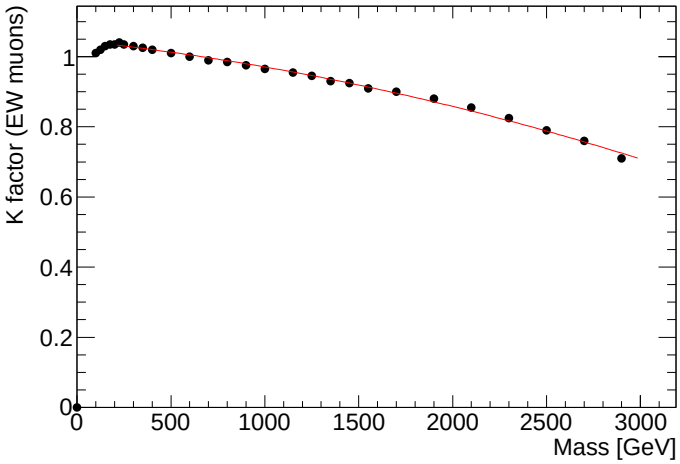

Figure 5.9. Fit to the differential electroweak K-factor as a function of true dimuon mass.

EW correction values were found using the HORACE event generator. Figure 5.9 shows the fit to the differential $\mathrm{K_{EW}}(m_{\mu\mu})$, which resulted in the following differential electroweak correction:

$$\mathrm{K_{EW}}(m_{\mu\mu}) = \begin{cases} 0.977 + (3.4 \times 10^{-4}) \times m_{\mu\mu}, & \text{for } m_{\mu\mu} \leq 172 \text{ GeV} \\ 1.04 - (5.60 \times 10^{-5}) \times m_{\mu\mu} & \\ \quad - (1.88 \times 10^{-8}) \times (m_{\mu\mu})^2, & \text{for } m_{\mu\mu} > 172 \text{ GeV} \end{cases} \tag{5.7}$$

Both the $\mathrm{K_{QCD}}$ and $\mathrm{K_{EW}}$ factors were applied multiplicatively to the DY simulation samples on an event by event basis. Each event was weighed as a function of the true invariant mass of the primary DY interaction.

A special procedure was used for the contact interaction signal samples which included both the leading-order DY component as well as the interference and pure CI terms. Assuming the new physics interaction is a colorless process, higher-order QCD corrections only affect the initial quarks/antiquarks, allowing $\mathrm{K_{QCD}}$ to be applied to the signal samples in the same manner as for the DY sample. In contrast, it was not

necessary to apply K_{EW} to the pure contact interaction, because any higher-order corrections to the propagator are encoded in the scale Λ. However, the difference in yield for the DY-only component of the signal simulation sample still needed to be taken into account, as it could not be separated from the pure BSM part of the sample. To do this, the number of DY-only events was found as a function of mass before (N_{DY}) and after (N'_{DY}) the K_{EW} factor was applied to the $Z \to \mu\mu$ sample. The difference in yield with and without K_{EW} applied to DY ($N'_{DY} - N_{DY}$) was then added to the invariant mass spectrum of the signal sample. This resulted in an overall shift in the number of events corresponding to higher-order corrections to the DY-only component of the signal samples.

None of the other non-DY backgrounds received K-factor corrections. The $t\bar{t}$ sample was scaled with the calculated NNLO cross section, and the diboson samples were scaled with the calculated NLO cross sections, as shown in Table 3.3. The number of expected events after selection was consistent with 0 in the mass distribution above $m_{\mu\mu} > 110$ GeV for all other backgrounds, as will be shown in the next chapter.

5.2.2 Pileup

As mentioned in Chapter 3, ATLAS has produced simulation samples including extra "pileup" collisions which occur in greater numbers as the LHC increases its instantaneous luminosity. However, the distribution of number of reconstructed vertices (N_{vtx}) in these samples did not exactly match the distribution in data. To correct for this, the procedure described below was followed:

- The N_{vtx} distribution was found in both data and simulation for events which were accepted by the muon trigger and passed the GRL requirements (section 2.5). These vertices were also required to have three or more tracks and longitudinal distance from the detector origin $|z|$ <200 mm.

Table 5.2. Event weights for different numbers of pileup vertices. No correction was made for $N_{vtx} > 9$.

N vertices	1	2	3	4	5	6	7	8	9
Weight	1.7955	1.2259	0.8834	0.6890	0.5686	0.4945	0.4511	0.4583	0.4513

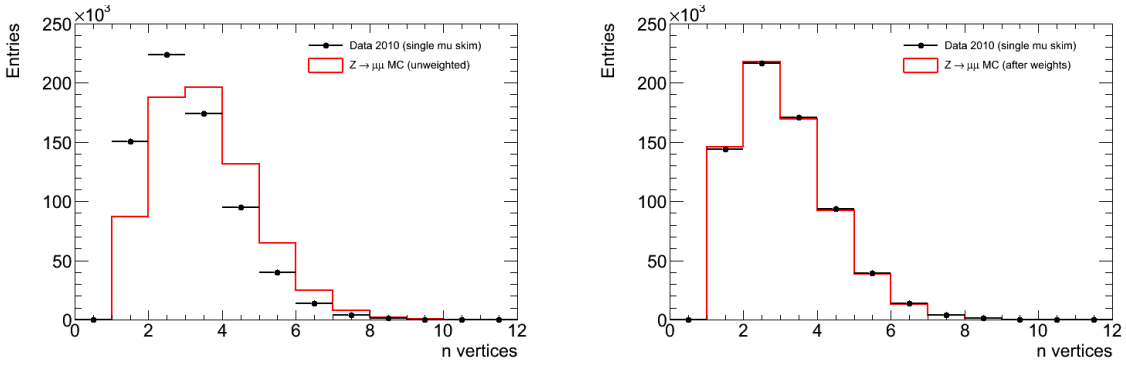

Figure 5.10. Distributions of the number of vertices per event before (left) and after (right) reweighing simulation events to data.

- Next, the N_{vtx} distribution in simulation was normalized to the data, and the ratio of data to simulation was calculated to get a set of event weights as a function of N_{vtx}.

- Finally, these weights were applied on an event-by-event basis to all signal and background samples.

Figure 5.10 compares the N_{vtx} distribution in simulation before normalization to the full 2010 dataset and after the sample had been reweighed. Table 5.2 shows the weights found as a function of N_{vtx}.

5.2.3 Muon Momentum Resolution

Even with the first pass of reprocessing with new calibration and alignment constants, the data had not reached the nominal resolution described in section 2.4. Instead, the muon momentum in simulation needed to be corrected in order to be in

better agreement with the measured resolution in data. This was done by fitting a series of simulation templates to both the Z^0 peak width and mean. The difference in resolution observed in data to the nominal value for a single muon is related to Eq. (5.2) and can be expressed in the form[1]:

$$\Delta\frac{q}{p_T} \;=\; \Delta S_1^{MS}\; g_1\; \frac{q}{p_T} \;+\; \Delta S_2^{MS}\; g_2, \tag{5.8}$$

where ΔS_1^{MS} is the difference in momentum scale from the nominal value, ΔS_2^{MS} is the difference from the nominal value of the intrinsic resolution of the curvature of the muon, q is the charge of the muon and g_1 and g_2 are normally-distributed random numbers with mean = 0 and width = 1. At low momentum, the first term dominates the resolution and the dimensionless value $\Delta S_1^{MS} = 0.02$ was found by letting S_1^{MS} in Eq. (5.2) be a free parameter in the fit of the Z^0 peak.

At higher momentum, however, the S_2^{MS} term becomes more important as the sagitta becomes smaller, and misaligned muon chambers are the largest contribution to this factor. In order to get a handle on S_2^{MS} from data, the relative alignment between overlapping large and small sector chambers was studied using stand-alone muon tracks. The difference in sagitta measurements as a function of ΔS_2^{MS} is given by:

$$\Delta s \simeq \frac{0.3}{8} \cdot B \cdot L^2 \cdot \Delta S_2^{MS} \times 10^3 \;\; [\mu\text{m}], \tag{5.9}$$

where B is the magnetic field intensity measured in Tesla, L is the track length measured in meters and ΔS_2^{MS} is measured in TeV^{-1}.

The alignment was relatively similar in the barrel and endcap regions up to $|\eta| < 2.0$. In the CSC region, the effect was larger due to larger uncertainties in

[1]The term in Eq. (5.2) parameterizing the energy loss in the calorimeter is very small at high muon momentum compared to the other sources of error, thus it was neglected [88].

Table 5.3. Extra smearing needed in addition to the nominal resolution already imposed in the simulation.

Region	Δs [μm]	ΔS_2^{MS} [TeV^{-1}]
$\lvert\eta\rvert < 2.0$	100 ± 20	0.18 ± 0.04
$\lvert\eta\rvert > 2.0$	500 ± 200	0.70 ± 0.20

the alignment. The Δs measurements and corresponding ΔS_2^{MS} parameters in these two regions are summarized in Table 5.3.

Using the values of ΔS_1^{MS} and ΔS_2^{MS} as input to Eq. (5.8), the inverse momentum of each muon in simulation was smeared by $\Delta(q/p_T)$, which also allowed for the sign of the charge of the muon to flip. Figure 5.11 shows the Z^0 peak in data with both muons in the barrel-barrel, endcap-endcap and CSC-CSC regions, along with the fitted simulation. After the resolution correction, the simulation is in much better agreement with the data in each of these regions.

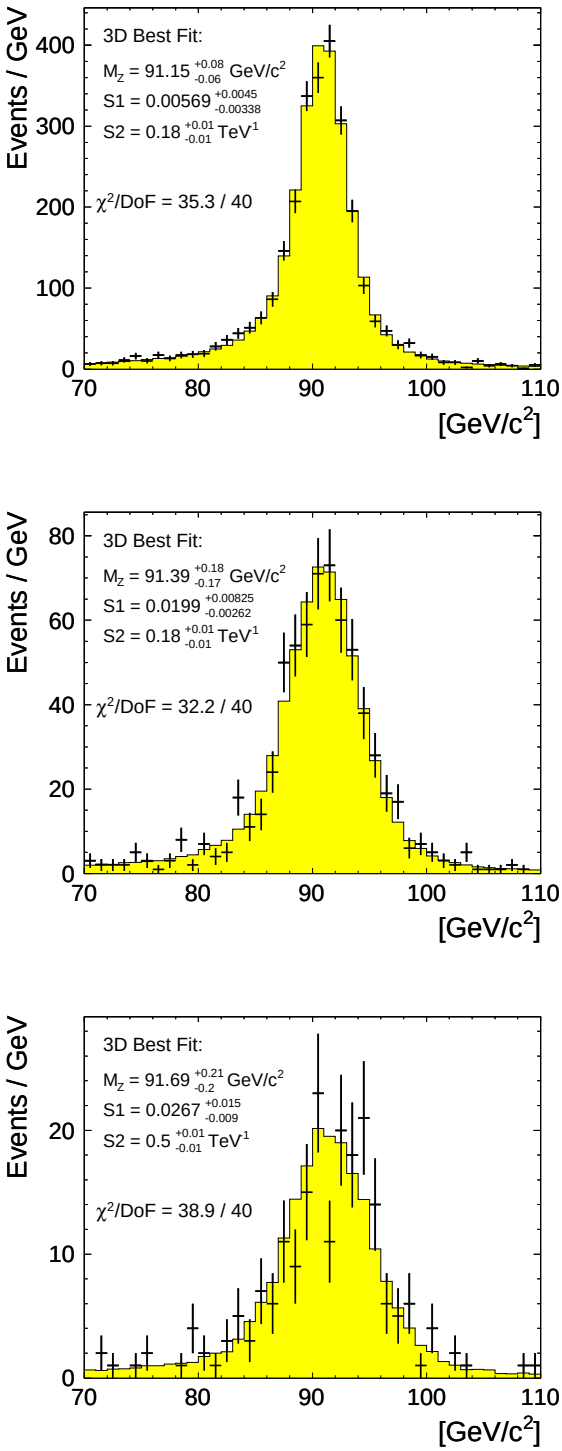

Figure 5.11. Mass distributions around the Z^0 peak comparing data to simulation, where the simulation has been fitted with the form of Eq. (5.2) for barrel-barrel (top), endcap-endcap (middle) and CSC-CSC (bottom) dimuons.

CHAPTER 6

EVENT SELECTION

The selection detailed in section 4.4 for the $Z \to \mu\mu$ cross section measurement formed the basis of the event and muon selection used in the contact interaction analysis. However, there were several special requirements made for this study due to the higher muon momentum range relevant to the search for contact interactions. Minimizing poorly-reconstructed muons and reducing the momentum resolution uncertainty of these high-p_T muons were priorities in choosing the selection, as mismeasurements could cause lower mass events to appear as an excess in the tail of the mass spectrum and mimic a contact-interaction-like signal. Sections 6.1 and 6.2 describe the event preselection and muon selection in detail. An estimation of cosmic-ray muon contamination after all selection is shown in section 6.3. Finally, the procedure to normalize the invariant mass spectrum in simulation to data is demonstrated in section 6.4.

6.1 Event Preselection

Similarly to the $Z \to \mu\mu$ cross section measurement presented in Chapter 4, the data were selected with the best possible detector conditions by requiring luminosity blocks to belong to a Good Runs List (GRL). As all simulation samples were produced with nominal running conditions, the GRL selection criterion was applied only to data.

Because this analysis searches for new physics in the high-p_T regime and all potential signal events need to be studied, the lowest unprescaled trigger threshold was

Table 6.1. Trigger requirement and integrated luminosity (after GRL) for each run period. Here, L1 and EF refer to the Level 1 and event filter trigger levels, respectively. The single muon triggers are denoted with their corresponding momentum threshold. The Muid algorithm was used in the event filter trigger layer, unless denoted by MG which indicates that the MuGirl algorithm was used. The EF triggers have been seeded by L1_MU0, except for "tight" EF triggers which have been seeded by L1_MU10.

Run Period	Run Numbers	Trigger	Luminosity [pb^{-1}]
A – $E3$	152166 - 160879	L1_MU10	0.78
$E4$ – $G4$	160899 - 165818	EF_mu10 or EF_mu10_MG	6.02
$G5$ – $I1$	165821 - 167576	EF_mu13 or EF_mu13_MG	15.80
$I1$ – $I2$	167607 - 167844	EF_mu13_tight or EF_mu13_MG_tight	19.08
Total			41.68

used for every run period, starting with L1_MU10 for periods A through $E3$. The full trigger requirements are listed in Table 6.1 for the run periods in 2010. Since there was no prescaling in simulation, L1_MU10 was used for all samples in order to take the acceptance of the trigger system into account.

Finally, to ensure a collision event occurred and to reduce the contamination from non-physics backgrounds (such as cosmic-ray muons) in our sample, one primary vertex (PV) having a longitudinal distance (z_{vtx}) less than 200 mm from the center of the detector was required. The latter requirement is looser than the range used in the Z cross section measurement after further studies were done on the z_{vtx} distribution with the full 2010 dataset (see Fig. 6.1).

The invariant mass of all combined muon pairs after this event preselection is shown in Fig 6.2. Here, there is still a large contamination from QCD backgrounds, which affects the data-simulation agreement as the shape of the mass distribution of these backgrounds is not yet well understood at $\sqrt{s} = 7$ TeV. Also, even with corrected simulation, the discrepancy in the tail of the dimuon mass distribution demands the need for tighter muon quality selection.

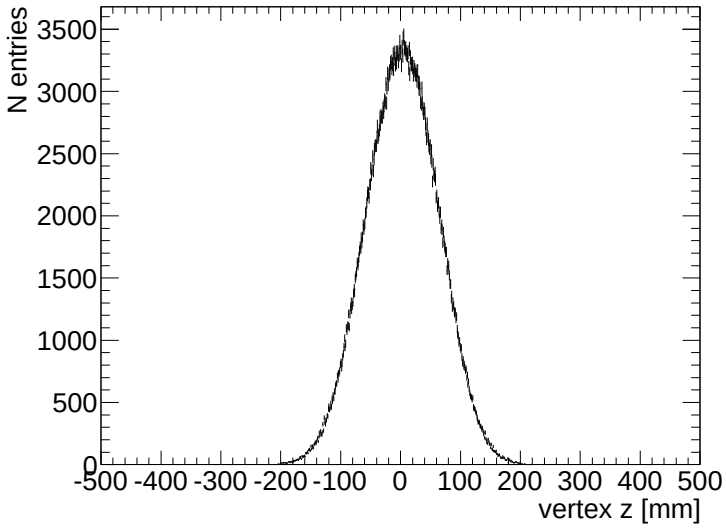

Figure 6.1. Longitudinal distance from the origin of the primary vertex in collision events.

6.2 Muon Selection

In this analysis, Muid combined muons were used. In order to reduce the background of other non-DY physics processes, two muons were required per event, each passing the following selection criteria:

- Combined $p_T > 25$ GeV.
- $|\eta| < 2.4$ to be within the acceptance of the trigger system.
- Longitudinal distance $|z_0| < 1$ mm and transverse distance $|d_0| < 0.2$ mm with respect to the primary vertex to reduce the contamination from cosmic muons and heavy-flavor decays (see Fig. 6.3).
- To further reduce the non-DY backgrounds where dimuons are produced within jets, a track-based isolation requirement is made relative to the muon p_T. In this case, the p_T sum of all inner detector tracks (minus the muon p_T) in a cone

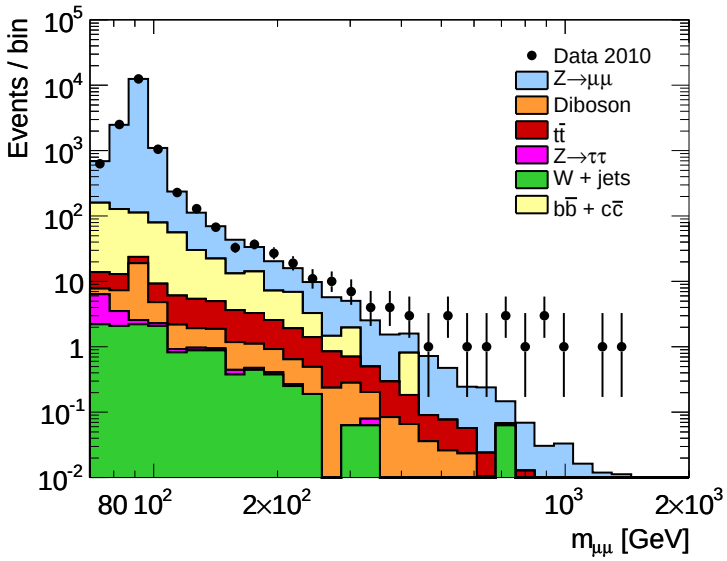

Figure 6.2. Invariant mass of two combined muons after event preselection.

of $dR < 0.3$ around the muon is calculated and the ratio of this sum to the muon p_T is required to be less than 0.05 (Fig. 6.4).

In addition, muons were required to satisfy the following criteria to ensure the best possible quality tracks:

- Inner detector requirements:
  - At least one B-layer hit in the Pixel detector, if one was expected (if the track either passed through a region where there was no B-layer or if there was a dead B-layer sensor, then this criterion was skipped).
  - At least 2 hits in the Pixel detector (taking into account known dead sensors as for the B-layer).
  - At least 6 hits in the SCT detector (taking into account known dead sensors as for the B-layer).
  - No more than one missing hit on the track in either the Pixel or SCT detector.

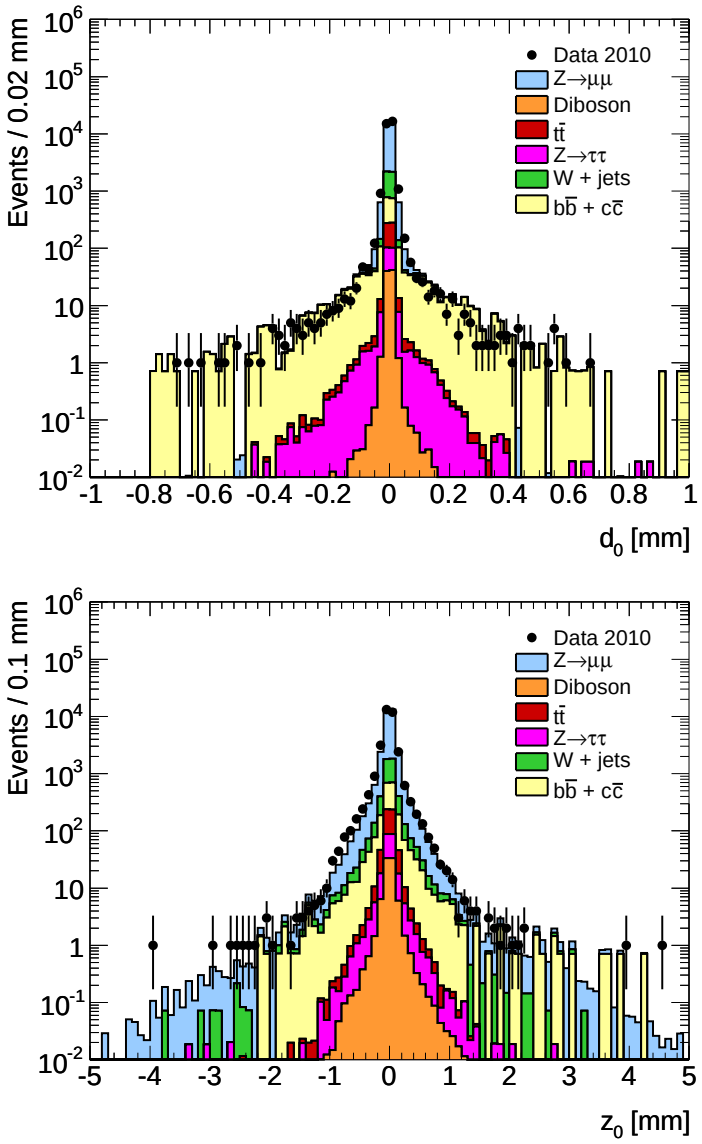

Figure 6.3. Muon transverse (top) and longitudinal (bottom) distance from the primary vertex with all other muon selection criteria applied except that on the variable shown. Here, the number of events in simulation has been normalized to the data.

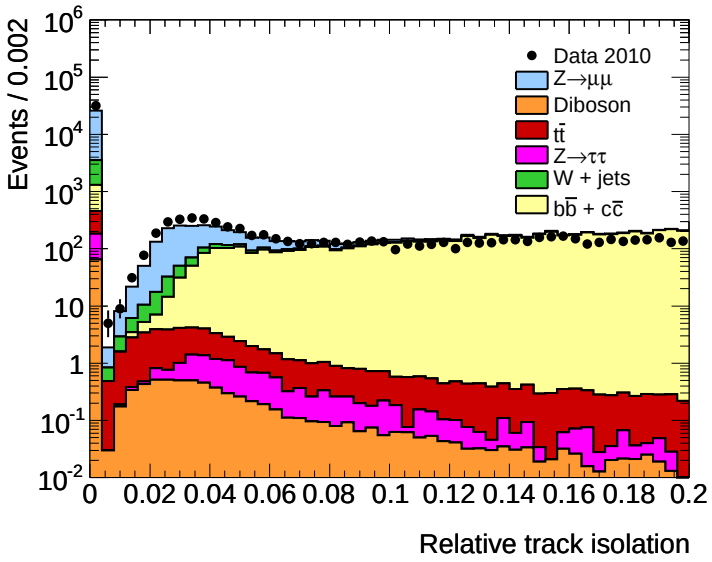

Figure 6.4. Distribution of relative track isolation for single muons after all other selection criteria were applied. Here, the number of events in simulation has been normalized to the data.

  - Within the acceptance of the TRT detector ($|\eta| < 1.9$) at least TRT 5 hits were required, where the number of associated off-track hits ("outliers") was less than 90% of the total number of on-track and outlier TRT hits. At the edge of the TRT acceptance and beyond ($|\eta| > 1.9$), tracks were accepted if the total number of TRT hits was less than 5. Otherwise, the same rule for $n \geq 5$ hits above is required.

- Because the magnetic field is not uniform in ϕ (Fig. 2.9), knowing the muon position in the bending (or precision) plane was not enough to ensure a correct momentum measurement. Thus, the muon track was required to have at least one non-precision hit in the MS (ϕ-hit) which is measured in either the trigger chambers (RPC or TGC) or in the CSCs.

- The best momentum measurement was made when a muon passed through at least 3 MS stations, as the track sagitta could be properly measured. Each

muon was required to have at least 3 precision hits in the inner, middle and outer stations. Figure 6.5 shows the distribution of hits in the inner, middle and outer precision stations and Fig. 6.6 shows the number of precision stations traversed by single muons in the sample. Figure 6.7 shows the single muon momentum distributions for tracks with less than 3 stations compared to those with 3 or more stations. It is clear that the data-simulation agreement is better in the tail of the distribution for the latter case.

- Muons were poorly measured in the MS barrel and endcap chamber overlap region as the relative alignment between them was not well known. Thus, muon tracks were required to cross only barrel or only endcap MS stations. The measurement was also worse where chambers were known to be poorly aligned with respect to the rest of the detector (BEE, EE, BIS7 and BIS8 chambers were not aligned in the 2010 data). Muons in these regions and chambers were vetoed.

Finally, both muons were required to be of opposite charge.

After all selection criteria were applied, a sample of 7743 dimuon events with mass $m_{\mu\mu} > 70$ GeV was found in the dataset.

Table 6.2 shows the relative selection efficiency for the simulated signal and background samples. After requiring two combined muons with kinematic cuts p_T >20 GeV and $|\eta|$ <2.4, the largest selection efficiency drop for the simulated $Z \to \mu\mu$ sample was due to the MS hits criteria, which included the three MDT station and ϕ-layer requirements. The W with jets background was mainly reduced by requiring two combined muons with p_T >20 GeV, as the second muon coming from the jet was much softer. The isolation requirement reduced this background further, and was the main background reduction for higher-momentum muons from $b\bar{b}$ and $c\bar{c}$ decays. The $t\bar{t}$ and diboson contributions to the non-DY background remained the largest after all selection.

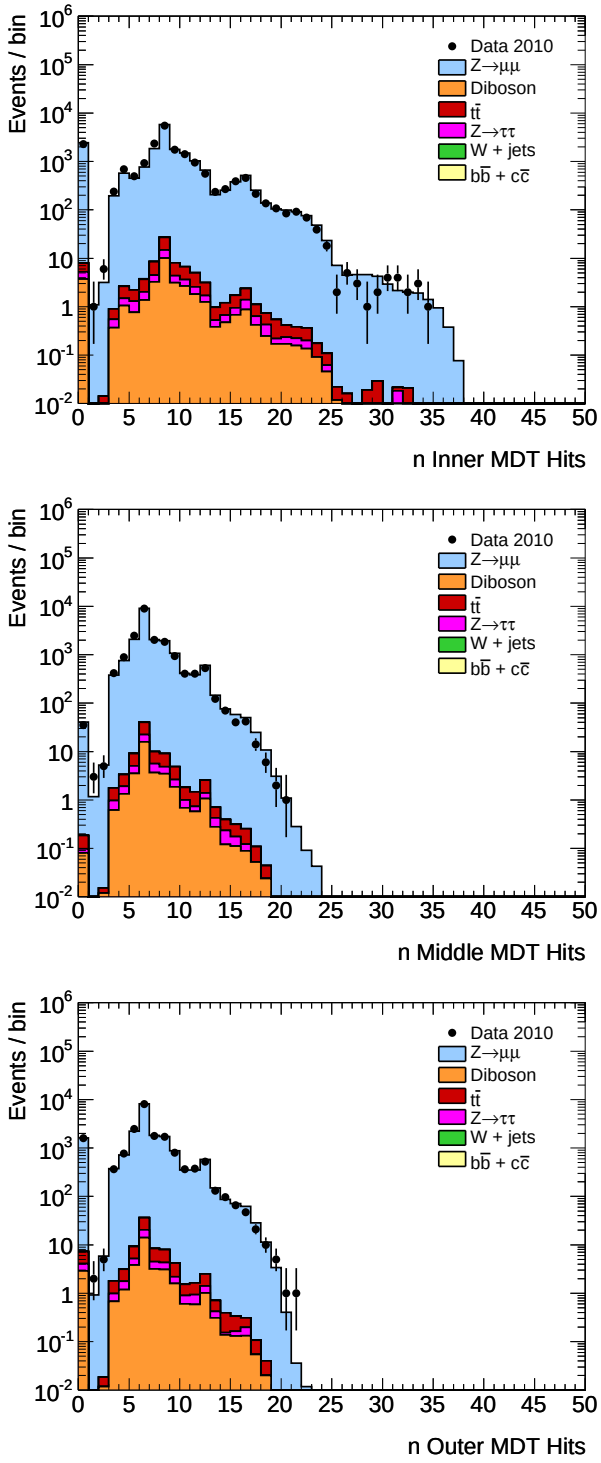

Figure 6.5. Distributions of precision hits in the inner, middle and outer stations (top, middle and bottom, respectively) after all other muon selection.

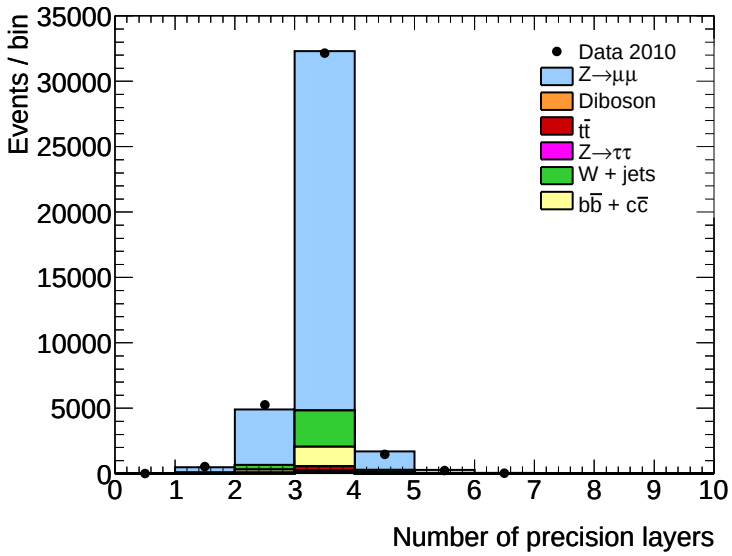

Figure 6.6. Number of MDT stations traversed by a muon which has passed all other selection. Here, the number of events in simulation has been normalized to the data.

Table 6.3 shows the number of events in data that satisfied the successive stages of selection, starting from a smaller dataset of events which had passed the event selection and contained at least two combined muons. Similarly to the simulated $Z \rightarrow \mu\mu$ sample, the largest drop in selection efficiency in data after kinematic selection criteria occurred with the MS hits requirement.

Fig. 6.8 provides a representation of the selection flow on the background samples in comparison to the data after event selection.

6.3 Cosmic Muon Background Estimation

Events with two muons back-to-back in η (or $\Sigma\eta_i = \eta_{\mu 1} + \eta_{\mu 2} \simeq 0$) were studied in order to determine the rate of cosmic muons in the 2010 dataset. Selecting events with two combined muons, each with p_T >25 GeV, $|\eta| < 2.4$ and muon quality selection as described in Section 6.2, the distributions of $\Sigma\eta_i$ were considered for three cases:

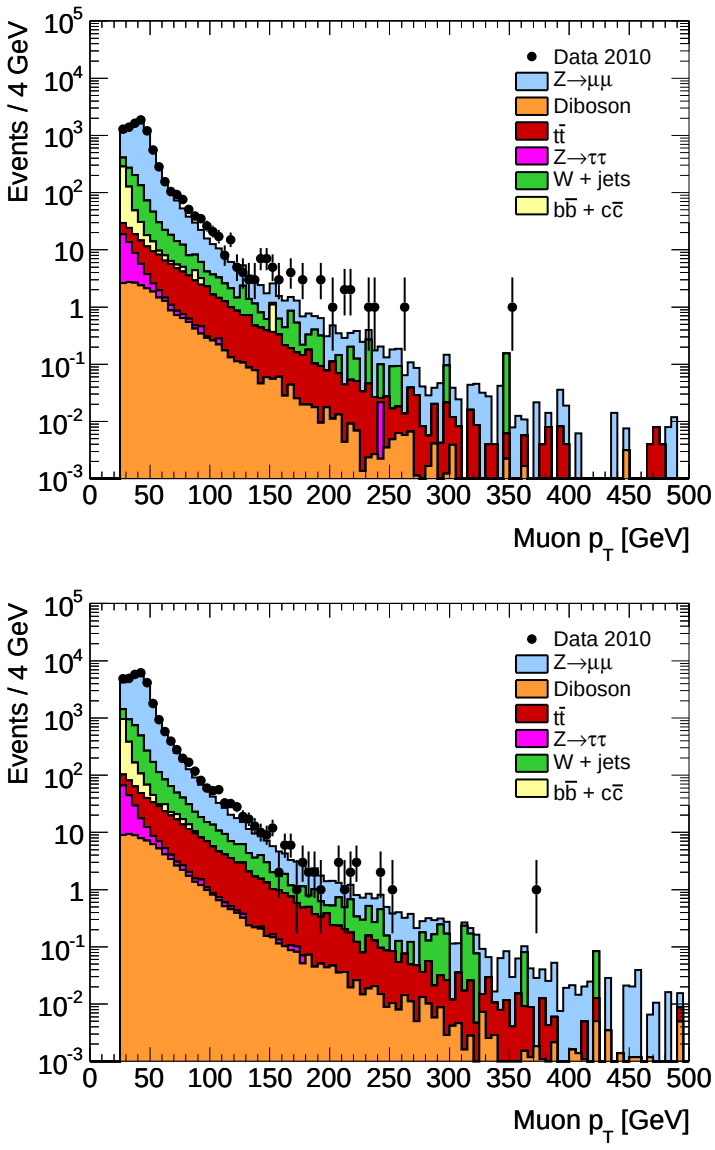

Figure 6.7. Single muon momentum distributions for tracks with less than three stations (top) and for tracks with three or more stations (bottom). Here, the number of events in simulation has been normalized to the data.

Table 6.2. Relative and absolute selection flow for the background simulation samples. Here, the MS hits requirement includes the MDT layers and ϕ hit selection criteria. Recall that some samples were produced with kinematic cuts at the generator level (see Chapter 3). These values are without any corrections applied to simulation.

Selection	$Z \to \mu\mu$		$W \to \mu\nu$		$Z \to \tau\tau$	
Criteria	Rel. %	Abs. %	Rel. %	Abs. %	Rel. %	Abs. %
`L1_MU6`	83.87	83.87	60.63	60.63	14.39	14.39
Vertex	99.63	83.56	99.56	60.36	99.67	14.34
2 Muid CB muons	63.12	52.74	1.78	1.07	10.14	1.45
$\lvert\eta\rvert < 2.4$	93.24	49.18	90.23	0.97	93.63	1.36
$p_T > 20$ GeV	76.00	37.87	0.28	<0.01	3.44	0.05
ID hits	97.42	36.89	92.40	<0.01	96.34	0.05
MS hits	59.90	22.10	62.66	<0.01	59.55	0.03
$\lvert d_0\rvert$ <0.2 mm	99.97	22.09	93.94	<0.01	96.44	0.03
$\lvert z_0\rvert$ <1 mm	99.65	22.01	76.34	<0.01	99.03	0.03
Isolation	94.48	20.80	4.23	<0.01	91.95	0.02
Opposite Charge	100.00	20.80	100	<0.01	100	0.02
$m_{\mu\mu} > 70$ GeV	98.54	20.50	67	<0.01	37.8	<0.01

Selection	Diboson		$c\bar{c} + b\bar{b}$		$t\bar{t}$	
Criteria	Rel. %	Abs. %	Rel. %	Abs. %	Rel. %	Abs. %
`L1_MU6`	42.74	42.74	81.49	81.49	42.68	42.68
Vertex	99.78	42.65	99.69	81.23	99.74	42.57
2 Muid CB muons	17.11	7.30	12.24	9.94	33.04	14.07
$\lvert\eta\rvert < 2.4$	94.81	6.92	95.84	9.53	97.66	13.73
$p_T > 20$ GeV	43.31	3.00	0.28	0.03	14.01	1.92
ID hits	97.38	2.92	92.20	0.03	96.03	1.85
3 MS stations	60.29	1.76	71.67	0.02	58.89	1.09
$\lvert d_0\rvert$ <0.2 mm	99.77	1.75	60.82	0.01	90.16	0.98
$\lvert z_0\rvert$ <1 mm	99.78	1.75	94.69	0.01	99.16	0.97
Isolation	91.92	1.61	<0.01	<0.01	59.04	0.57
Opposite Charge	99.17	1.60	<0.01	<0.01	99.88	0.57
$m_{\mu\mu} > 70$ GeV	92.29	1.47	<0.01	<0.01	73.38	0.42

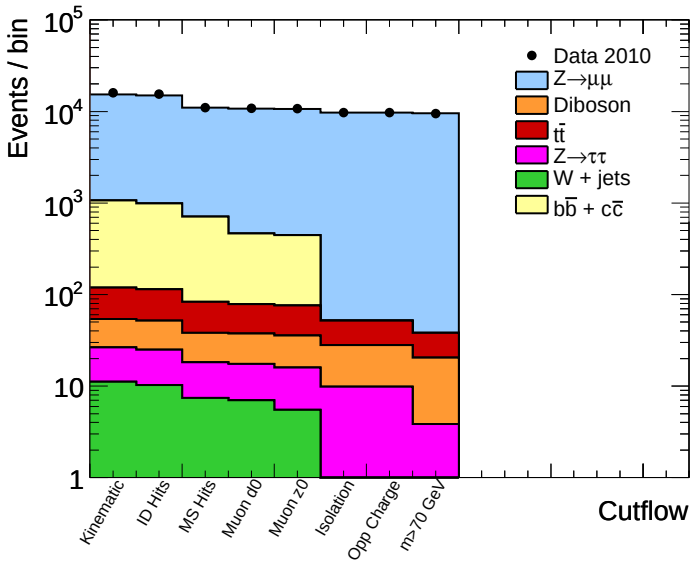

Figure 6.8. Selection flow for background samples compared to data. The criteria listed on the x-axis are required for both muons. Here, the "kinematic" stage includes the p_T and η selection criteria.

1. Events which did not pass either the vertex selection (primary vertex with $|z| < 200$ mm and 3 or more associated ID tracks) or the muon impact parameter selection ($|z_0|$ <1 mm and $|d_0|$ <0.2 mm with respect to primary vertex).

2. Events which passed the vertex selection but not the muon impact parameter selection.

3. Events passing all selection.

In the first two cases, there is a distinct peak at $\Sigma\eta_i \simeq 0$ (Fig. 6.9), indicating cosmic muon contamination. To predict the rate of cosmic events in the data after all selection, a window of $|\Sigma\eta_i|$ <0.002 was chosen based on the distributions of case 1 and case 2, as they were expected to contain only cosmic muons. In this window, there were 3 events after all selection. Since there were 7743 dimuon events in total, this gave an approximate contamination of <0.04% in the data sample. This was a very

Table 6.3. Selection flow for the 2010 MuonStream data.

Selection Criteria	N_{events}
Two muons in data with p_T >20 GeV	541547
GRL	509506
Trigger requirement	509489
Vertex requirement	508622
2 Muid combined muons	63078
$\|\eta\| < 2.4$	60142
$p_T > 20$ GeV	15951
ID hits	15466
MS hits	9035
$\|d_0\|$ <0.2 mm	8845
$\|z_0\|$ <1 mm	8812
Isolation	7965
Opposite Charge	7965
$m_{\mu\mu} > 70$ GeV	7744

small number compared to other backgrounds, and so the cosmic muon contamination was safely neglected in this analysis.

6.4 Normalization to Data

Finally, after all corrections mentioned in Section 5.2 were made to the simulation, the Z^0 peak was used as a control region to normalize the overall invariant distribution of expected backgrounds. The main benefit of doing so was that all mass-independent systematic uncertainties, such as the luminosity uncertainty, canceled in the data-simulation ratio. In simulation, all background processes were scaled to their respective cross sections, added together, and the resulting invariant mass distribution was normalized to the data in the range $70 < m_{\mu\mu} < 110$ GeV. This gave a normalization factor of 38 pb^{-1}. Table 6.4 shows the number of data events as well as the expected number of SM-only events in various mass bins after all selection and normalization. Table 6.5 shows the expected number of events after all selection for each signal process (with non-DY backgrounds added) using the same normalization

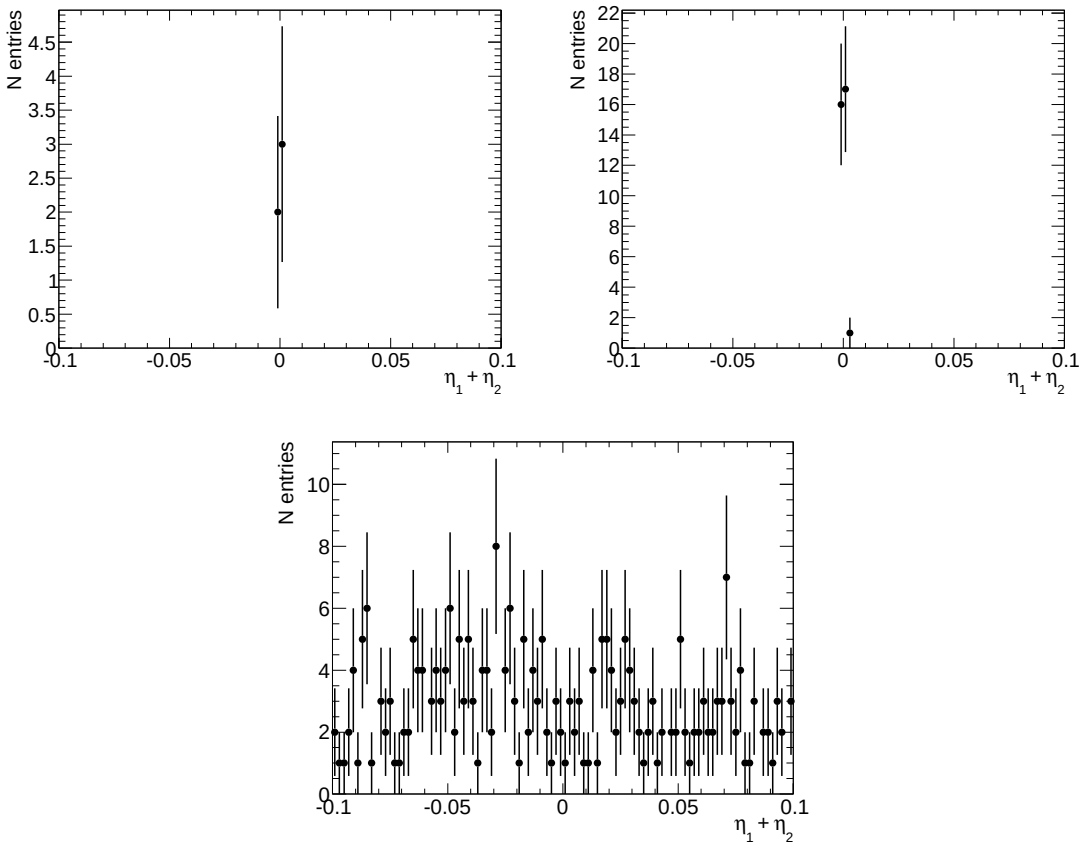

Figure 6.9. Distribution in data of $\Sigma\eta_i$ for cases 1, 2 and 3 (top-left, top-right and bottom, respectively).

scale. In both cases, the error quoted is statistical only. Note that $b\bar{b}$ and $c\bar{c}$ are not listed, as none of the simulated events survived the full selection.

6.5 Kinematic Distributions of Selected Events

Figure 6.10 shows the invariant mass distributions of data and simulation after all selection for the combined muons, extrapolated MS tracks and ID tracks. The MS distribution has a couple of excess events in the tail, likely due to misaligned chambers. The agreement with simulation was recovered in the fit of the combined muons. Figures 6.11-6.13 show muon kinematic distributions of p_T, η and ϕ, where the data agrees well with the simulation. The acceptance gap at $|\eta| \simeq 0$ and $|\eta| \simeq 1.4$

Table 6.4. Expected number of events in the dimuon channel after normalization to observed data in the 70-110 GeV range. The errors quoted are statistical only.

Mass (GeV)	70-110	110-130	130-150	150-170	170-200	200-240
DY	7547 ± 7	98.4 ± 0.8	33.4 ± 0.5	17.2 ± 0.3	12.8 ± 0.3	7.8 ± 0.2
$t\bar{t}$	6.0 ± 0.2	2.4 ± 0.1	1.7 ± 0.1	1.24 ± 0.04	1.22 ± 0.03	1.03 ± 0.03
Diboson	10.1 ± 0.1	0.8 ± 0.1	0.56 ± 0.04	0.48 ± 0.04	0.41 ± 0.03	0.28 ± 0.03
W+jets	0.14 ± 0.08	< 0.05	< 0.05	< 0.05	< 0.05	< 0.05
Total	7563 ± 7	101.6 ± 0.8	35.7 ± 0.5	18.9 ± 0.3	14.4 ± 0.3	9.1 ± 0.2
Data	7563	101	41	11	11	7

Mass (GeV)	240-300	300-400	400-550	550-800	800-1200	1200-2000
DY	5.05 ± 0.11	2.49 ± 0.04	0.99 ± 0.01	0.29 ± 0.01	0.06 ± 0.01	< 0.05
$t\bar{t}$	0.73 ± 0.02	0.37 ± 0.01	0.11 ± 0.01	< 0.05	< 0.05	< 0.05
Diboson	0.24 ± 0.02	0.16 ± 0.02	0.06 ± 0.01	< 0.05	< 0.05	< 0.05
W+jets	< 0.05	< 0.05	< 0.05	< 0.05	< 0.05	< 0.05
Total	6.02 ± 0.11	3.03 ± 0.05	1.16 ± 0.02	0.33 ± 0.01	0.07 ± 0.01	< 0.05
Data	6	2	0	1	0	0

is clearly visible and is well represented by the simulation. The structure in ϕ of the large and small MS sectors along with the feet region are also shown to have good agreement between data and simulation. Finally, Fig. 6.14 shows the invariant mass distribution along with three contact interaction samples for comparison.

Table 6.5. Expected number of events in the presence of new physics for various contact interaction scales with constructive (Λ^-) and destructive (Λ^+) interference. The errors quoted are statistical only.

Mass (GeV)	150-170	170-200	200-240	240-300	300-400
$\Lambda^- = 3$ TeV	19.14 ± 0.46	15.73 ± 0.41	11.22 ± 0.35	8.47 ± 0.30	7.89 ± 0.30
$\Lambda^- = 4$ TeV	18.79 ± 0.43	14.27 ± 0.37	10.01 ± 0.31	6.54 ± 0.24	5.04 ± 0.22
$\Lambda^- = 5$ TeV	17.44 ± 0.39	14.25 ± 0.36	9.40 ± 0.29	6.17 ± 0.24	4.33 ± 0.20
$\Lambda^- = 7$ TeV	17.32 ± 0.39	13.84 ± 0.35	9.26 ± 0.28	6.30 ± 0.23	3.26 ± 0.17
$\Lambda^+ = 2$ TeV	21.64 ± 0.59	19.31 ± 0.55	15.80 ± 0.50	15.22 ± 0.50	21.23 ± 0.60
$\Lambda^+ = 3$ TeV	18.59 ± 0.43	15.18 ± 0.39	10.05 ± 0.31	7.19 ± 0.26	5.45 ± 0.23
$\Lambda^+ = 4$ TeV	18.16 ± 0.40	14.29 ± 0.35	8.81 ± 0.27	6.05 ± 0.23	3.62 ± 0.18
$\Lambda^+ = 5$ TeV	18.48 ± 0.40	13.62 ± 0.34	8.84 ± 0.27	5.44 ± 0.21	2.91 ± 0.15

Mass (GeV)	400-550	550-800	800-1200	1200-2000
$\Lambda^- = 3$ TeV	6.01 ± 0.26	6.50 ± 0.27	5.11 ± 0.24	2.97 ± 0.17
$\Lambda^- = 4$ TeV	3.03 ± 0.17	2.27 ± 0.15	1.45 ± 0.12	1.08 ± 0.09
$\Lambda^- = 5$ TeV	1.95 ± 0.13	1.29 ± 0.11	0.72 ± 0.08	0.36 ± 0.055
$\Lambda^- = 7$ TeV	1.26 ± 0.10	0.58 ± 0.07	0.21 ± 0.04	0.11 ± 0.031
$\Lambda^+ = 2$ TeV	21.60 ± 0.60	25.46 ± 0.64	21.41 ± 0.58	15.05 ± 0.46
$\Lambda^+ = 3$ TeV	4.59 ± 0.21	5.27 ± 0.23	4.29 ± 0.20	3.07 ± 0.17
$\Lambda^+ = 4$ TeV	2.10 ± 0.14	1.59 ± 0.12	1.52 ± 0.12	0.84 ± 0.08
$\Lambda^+ = 5$ TeV	1.61 ± 0.12	0.88 ± 0.09	0.53 ± 0.07	0.28 ± 0.05

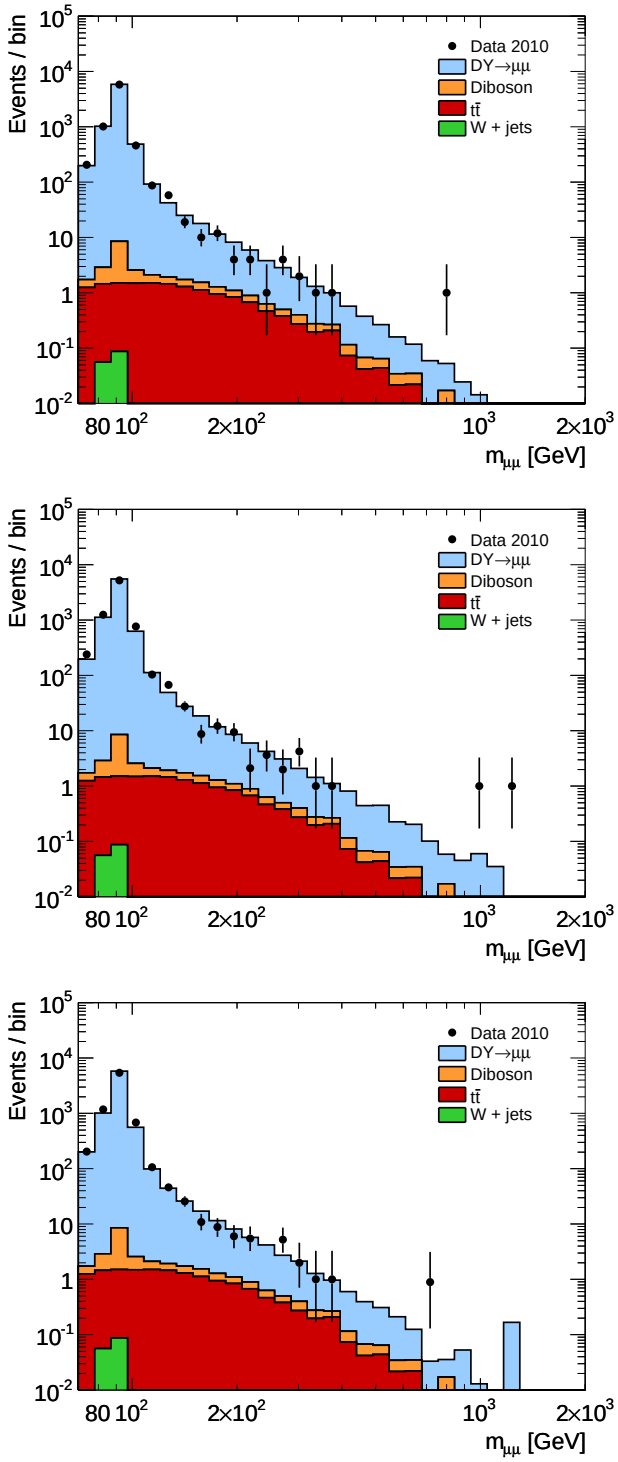

Figure 6.10. Dimuon invariant mass after all selection and simulation corrections for combined muons (top), MS extrapolated muons (middle) and ID tracks (bottom).

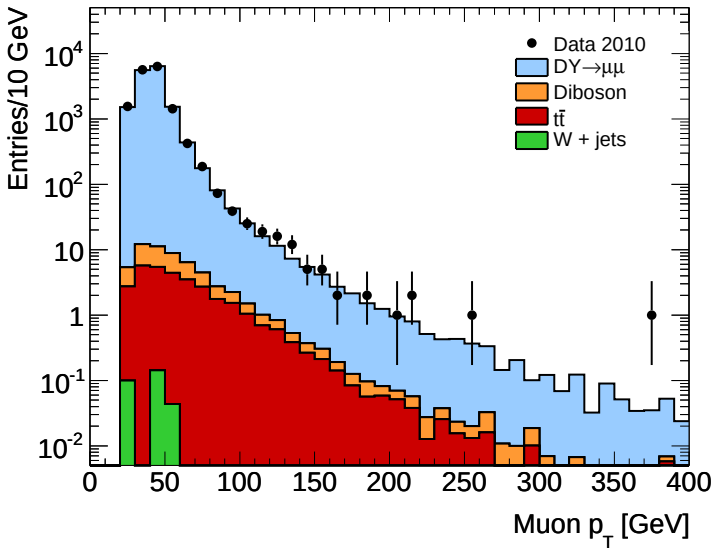

Figure 6.11. Muon momentum of both muons per event after all selection. Here, DY includes both $Z \to \mu\mu$ and $Z \to \tau\tau$ processes.

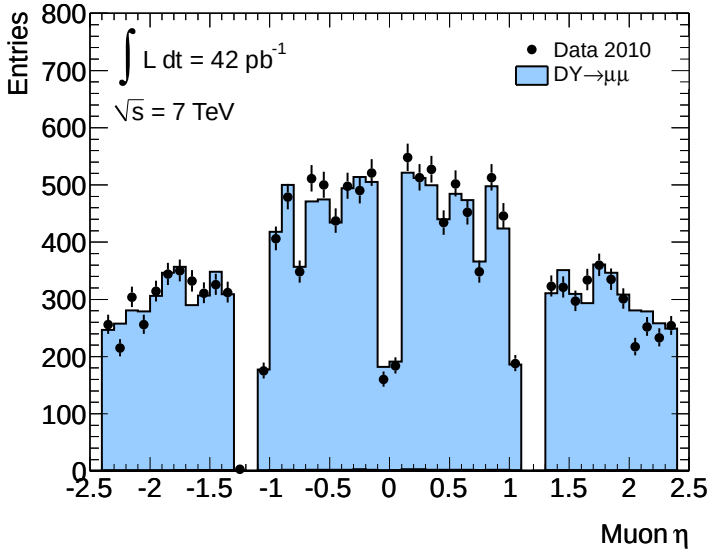

Figure 6.12. Muon η distribution after all selection. Non-DY backgrounds are included but are obscured by the dominant DY background, which includes both $Z \to \mu\mu$ and $Z \to \tau\tau$ processes.

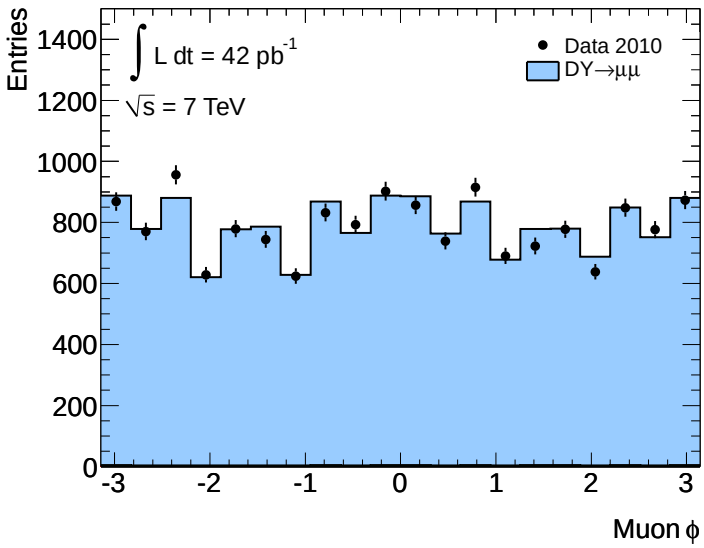

Figure 6.13. Muon ϕ distribution after all selection. Non-DY backgrounds are included but are obscured by the dominant DY background, which includes both $Z \to \mu\mu$ and $Z \to \tau\tau$ processes.

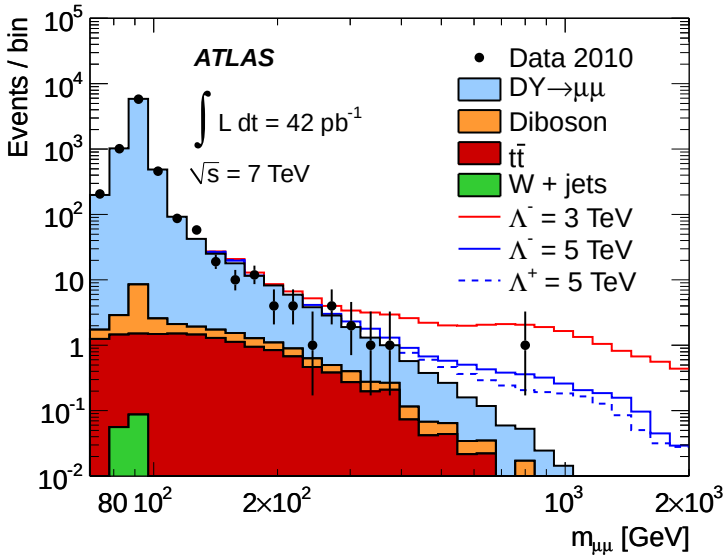

Figure 6.14. Dimuon invariant mass after all selection and simulation corrections. Here, DY includes both $Z \to \mu\mu$ and $Z \to \tau\tau$ processes. Examples of three benchmark values of contact interactions are shown.

CHAPTER 7

STATISTICAL ANALYSIS

After all simulation corrections, event selection and normalization to data, a search for contact interactions was performed in the high-mass tail of the dimuon spectrum. This chapter introduces Bayesian statistics, outlines the procedure for determining the consistency of data with the predicted SM yield in the signal region, and in lieu of a discovery of new physics, provides the general tools to set a limit using a Bayesian technique.

7.1 Bayes' Theorem

In general, Bayes' Theorem [89] states that the conditional (or "posterior") probability of A given B is:

$$\mathcal{P}(A|B) = \frac{\mathcal{L}(B|A)P(A)}{P(B)} \quad . \tag{7.1}$$

Here, $P(A)$ is the prior probability independent of $P(B)$, and $\mathcal{L}(B|A)$ is known as the conditional probability or "likelihood" of B given A. Because the integral of the posterior must equal one, $P(B)$ is taken as a normalization constant and can be rewritten as $\int \mathcal{L}(B|A)P(A)dA$.

When searching for new physics in a simple event counting example, A is the number of events of the new physics of interest, represented by μ, and B is the number of observed events represented by an integer number n. The parameter μ itself can be decomposed into signal (s) and background (b) components, as well as

depend on "nuisance" parameters (ν) which are not directly measured (for example muon resolution, efficiency, etc.):

$$\mu = s(\theta, \nu) + b(\nu). \tag{7.2}$$

Here, θ is a parameter characterizing the new physics on which the limit is set.

With this definition, the likelihood is conventionally distributed according to a Poisson function giving the probability to observe n events if the number of expected events is μ:

$$\mathcal{L}(n|\theta, \nu) = \frac{\mu^n e^{-\mu}}{n!} \quad . \tag{7.3}$$

This can be expanded to include N_k independent measurements or channels (or as will be shown later, N_k mass bins) by taking the product of the Poisson distributions:

$$\mathcal{L}(n|\theta, \nu) = \prod_{k=1}^{N_k} \frac{\mu_k^{n_k} e^{-\mu_k}}{n_k!} \quad . \tag{7.4}$$

The Poisson distribution can be approximated with a Gaussian function for sufficiently large number of observed events in a given channel k ($n_k \geq 40$).

According to Eq. (7.1), the posterior probability density function (PPDF) of the parameter θ given n and ν can be written as:

$$\mathcal{P}(\theta \mid n, \nu) = \frac{1}{Z}\mathcal{L}(n \mid \theta, \nu)P(\theta, \nu), \tag{7.5}$$

where Z normalizes the PPDF. As is, the prior probability function $P(\theta, \nu)$ depends on θ and the nuisance parameters ν. These nuisance parameters may be marginalized

by convolving each Poisson probability with a Gaussian-distributed prior probability function. For one particular channel k, the likelihood becomes:

$$\mathcal{L}(\bar{n} \mid \theta) = \frac{1}{C} \int \frac{(\mu')^n e^{-\mu'}}{n!} e^{-\frac{(\nu-\nu')^2}{2\sigma_\nu^2}} d\nu' \quad . \tag{7.6}$$

where $\bar{n}$ is the expected number of events after marginalization and C is a normalization constant to be incorporated with Z from Eq. (7.5). Note that the parameter μ' can depend on ν as shown in Eq. (7.2). The PPDF then becomes:

$$\mathcal{P}(\theta \mid \bar{n}) = \frac{1}{Z} \mathcal{L}(\bar{n} \mid \theta) P(\theta) \ . \tag{7.7}$$

Finally, the 95% credibility interval limit is then found by integrating over the PPDF and solving for θ_{lim}:

$$\int_0^{\theta_{lim}} \mathcal{P}(\theta' \mid \bar{n}) d\theta' = 0.95. \tag{7.8}$$

7.2 Consistency Check of Data with SM

One way to visually check whether or not there is an excess of events present in the data sample is to draw the integral from $m_{\mu\mu} \to \infty$ as a function of $m_{\mu\mu}$ (Fig. 7.1). No excess is observed relative to the SM expectation.

In order to quantify this agreement, a binned log-likelihood ($-ln(\mathcal{L})$) test between the data and the expected number of events from SM-only processes is constructed. Equation (7.4) can be written using $n_k \equiv$ number of events observed in data in a given invariant mass bin k and $\mu_k \equiv N_k^{exp}(\theta, \nu_k)$, the number of expected events in each mass bin for the SM-only hypothesis. The expected number of events was calculated in $k = 9$ invariant mass bins with limits $m_{\mu\mu}$ = 150, 170, 200, 240, 300, 400, 550, 800, 1200 and 2000 GeV (Fig. 7.2). The negative log-likelihood between the total number of events observed in data and SM-expected events in each mass bin was found to be

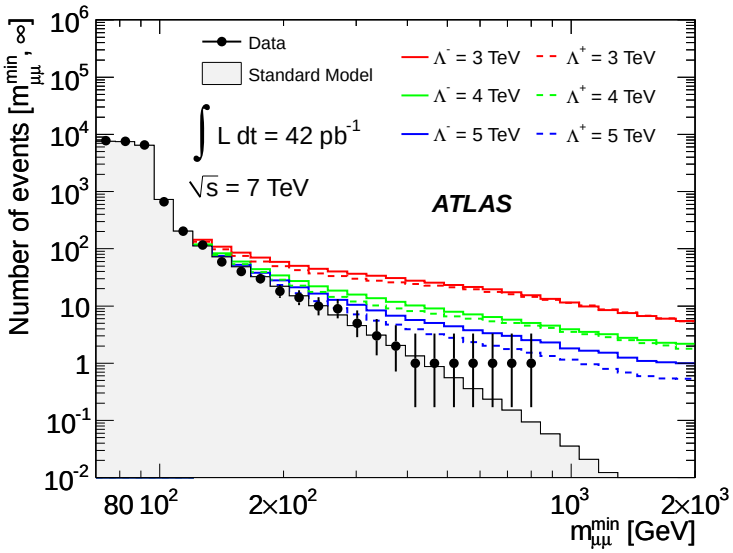

Figure 7.1. Integral of $m_{\mu\mu} \rightarrow \infty$ as a function of $m_{\mu\mu}$ for data, SM-only, and various contact interaction samples.

10.7. Pseudo-experiments were performed to determine $-ln(\mathcal{L})$ between the nominal SM and statistical fluctuations, where the number of expected SM events in each mass bin were fluctuated independently by a random Poisson-distributed amount. Figure 7.3 shows the resulting distribution after 100k pseudo-experiments, with an arrow indicating the $-ln(\mathcal{L})$ value found in data. The probability (or "p-value") that the data had not fluctuated to a value significantly different than the SM expectation was determined by taking the fraction of events in the pseudo-experiment distribution from the observed value to infinity relative to the total number of pseudo-experiments. Generally, a good agreement between data and the SM-only hypothesis is found if the p-value is at least 5%. In the analysis performed with the 2010 dataset, a p-value of 56% was found, thus showing consistency with the SM.

7.3 Bayesian Limit Setting Procedure

As the presence of new physics in the data had been ruled out, a binned Bayesian counting method was used in order to set a limit on the contact interaction scale Λ.

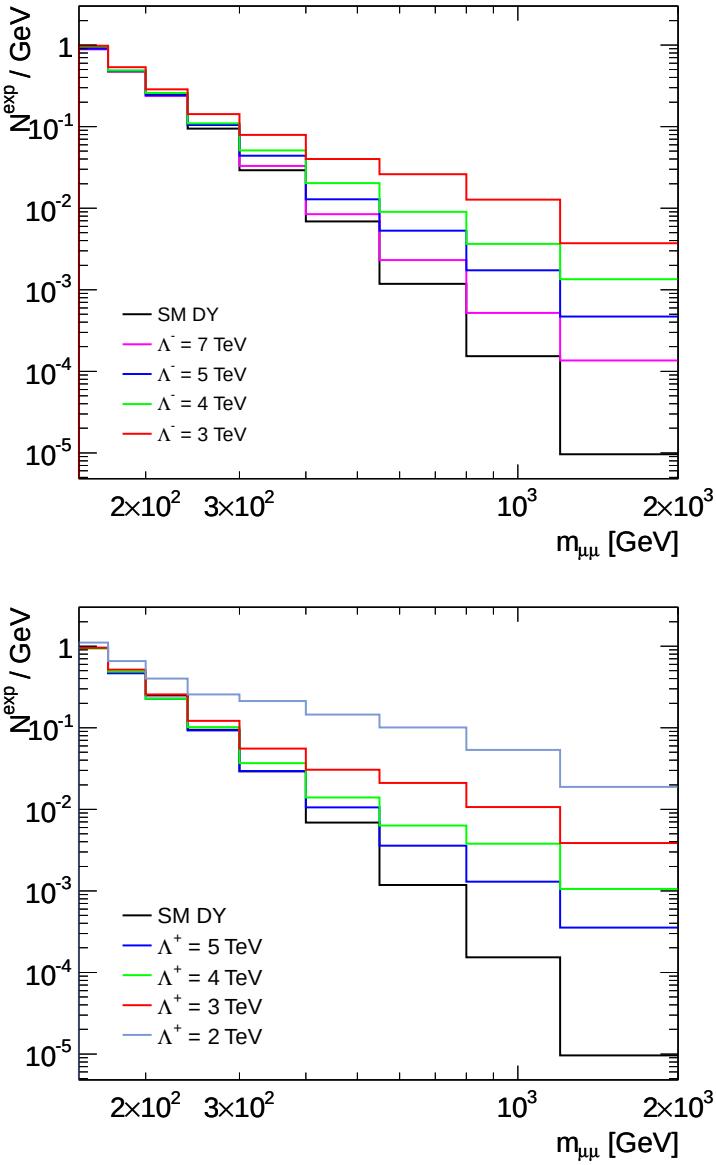

Figure 7.2. Number of expected events as a function of invariant mass for constructive (top) and destructive (bottom) interference models, normalized by the bin width.

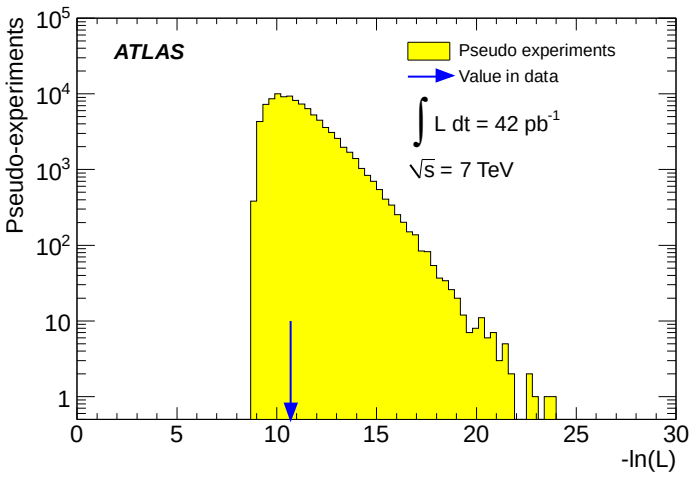

Figure 7.3. Negative log-likelihood distribution resulting from pseudo-experiments with fluctuations on the number of expected SM-only events. The value in data was found to be 10.7, with p-value = 56%.

7.3.1 Choice of Prior

The prior in Eq. (7.5) can be factored as $P(\theta, \nu) = P(\theta)P(\nu)$. Ideally, $P(\theta)$ should be chosen to be flat in the observable parameter θ. There are two Λ-dependent contributions to the cross section in Eq. (1.19). The interference which goes as $1/\Lambda^2$ is maximum when the DY contribution to the yield is equal to that of the new physics contribution. As $\Lambda \to \infty$ and the mass distribution approaches the DY-only shape, this term becomes more dominant, especially in mid-mass ranges. The other pure contact interaction term has a $1/\Lambda^4$ dependence, and is dominant in the very high mass tail where DY$\to$0. It also plays a larger role for $\Lambda \to 0$ as the new physics becomes more accessible at low q^2. Both of these terms in the cross section are mass dependent, and because the Λ value is not know a priori, neither term significantly dominates over the other in all of $\Lambda - m_{\mu\mu}$ phase space. Thus, the priors $\theta = 1/\Lambda^2$ and $\theta = 1/\Lambda^4$ are both considered. It should be noted, however, that $1/\Lambda^2$ is the prior most often chosen for CI searches, as the cross section has a quadratic dependence on $1/\Lambda^2$.

$P(\nu)$ is taken as a set of normalized Gaussian distributions with width $dN_k^{exp}(\Lambda)$ representing the effect of systematic uncertainties to be discussed later in the text. The posterior dependence on ν is numerically integrated out by sampling from $P(\nu)$ in each mass bin 50,000 times (enough to cover the Gaussian-distributed systematics phase space).

7.3.2 Analysis Method

More values of N_k^{exp} than what were calculated in the 8 benchmark simulation samples were needed in order to construct the PPDF. The number of expected events in each mass bin as a function of the prior θ was fit according to the quadratic form of the cross section, and the number of expected events was extracted as a function of the two priors.

$$N_k^{exp}(\Lambda) = c_0^k + \frac{c_1^k}{\Lambda^2} + \frac{c_2^k}{\Lambda^4} = \begin{cases} c_0^k + c_1^k \cdot \theta + c_2^k \cdot \theta^2, & \text{for } \theta = 1/\Lambda^2 \\ c_0^k + c_1^k \cdot \sqrt{\theta} + c_2^k \cdot \theta, & \text{for } \theta = 1/\Lambda^4 \end{cases} \tag{7.9}$$

These fits for both constructive and destructive interference are shown in Fig. 7.4. Note that the SM-only value corresponding to $\Lambda \to \infty$ was used in the fit as well. The likelihood was then calculated as a function of θ:

$$\mathcal{L}(\bar{n}|\theta) = \prod_{k=1}^{nbins} \frac{N_k^{exp}(\Lambda)^{n_k} \cdot e^{-N_k^{exp}(\Lambda)}}{n_k!} \quad . \tag{7.10}$$

Numerically, 50,000 steps in θ were taken. When finding the expected limit, n_k is the number of SM-only events calculated from simulation in each mass bin. For the observed limit, n_k is the number of events in data in each mass bin. Figure 7.5 shows the expected PPDF distribution for a SM-only sample as well as what the expected distribution would look like if there had been the presence of new physics with a contact interaction scale $\Lambda^- = 5$ TeV.

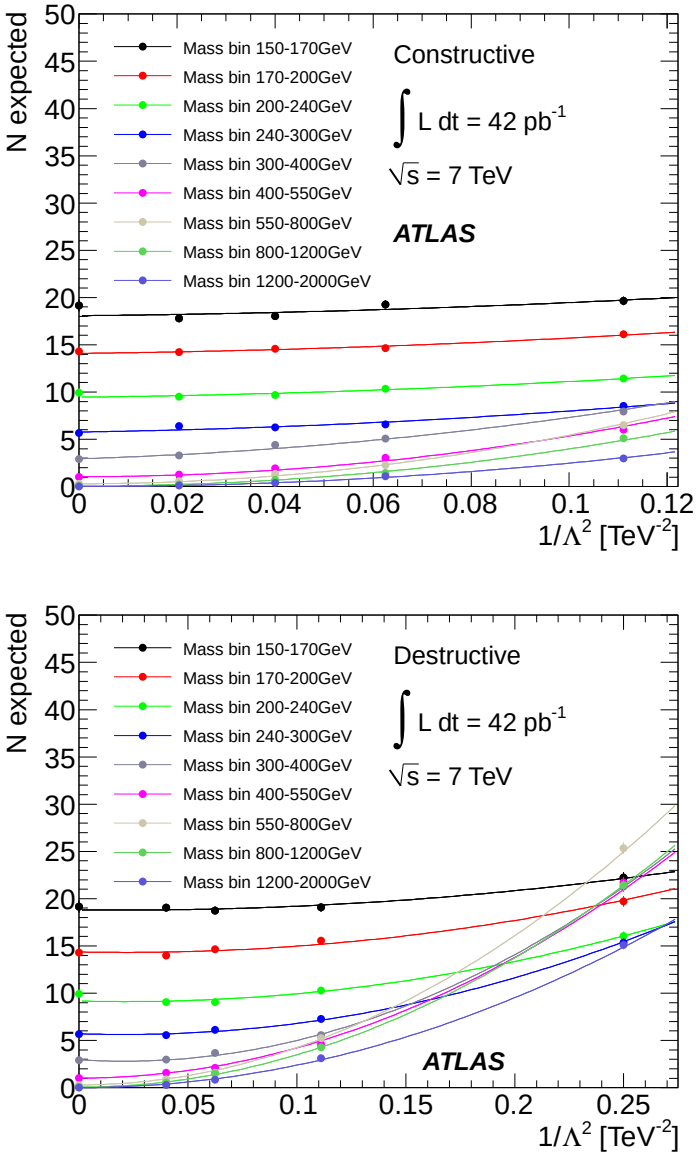

Figure 7.4. Quadratic fits in each mass bin for the constructive (top) and destructive (bottom) interference models as a function of $1/\Lambda^2$, with benchmark Λ values shown as points.

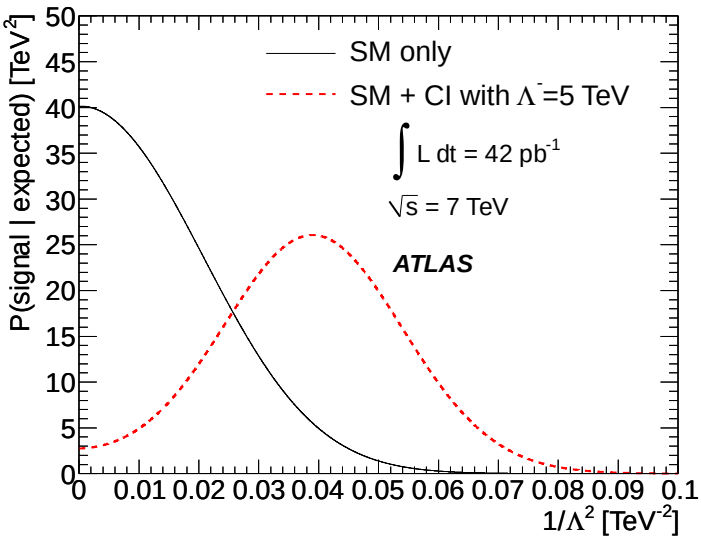

Figure 7.5. The expected PPDF from simulation for data consistent with the SM and in the presence of new physics at $\Lambda^- = 5$ TeV.

The procedure for folding the systematic uncertainties into the limit calculation will be discussed in the next chapter.

CHAPTER 8

SYSTEMATIC UNCERTAINTIES

This chapter discusses the theoretical and experimental systematic uncertainties associated to the analysis and demonstrates how these uncertainties were incorporated into the limit calculation.

8.1 Description of Systematic Uncertainties

Simulation was needed to predict the expected kinematic distributions and event yield in the high-mass DY tail, however, due to limited knowledge of these distributions with respect to what was present in data, systematic uncertainties in N_{exp} needed to be applied. These uncertainties were not expected to affect the limit calculation substantially for two main reasons: first, the largest limiting factor in the calculation was due to the small number of events in the signal region ($m_{\mu\mu}$ >150 GeV) which were subject to large Poisson fluctuations, and second, the dependence on mass of any uncertainties factored out after the simulated samples were normalized to the Z^0 peak. This allowed relatively conservative estimates of theoretical and experimental systematic uncertainties to be chosen.

8.1.1 Theoretical Uncertainties

The main mass-dependent theoretical uncertainties came from uncertainties in the proton structure and in the K-factors applied to the DY and signal samples.

- *Parton distribution functions*:

  The DY and CI samples were produced with the MRST2007LO* PDF set (higher-

order corrections to the PDF were accounted for in the K-factors, so relating uncertainties are discussed below). The uncertainty in the parton structure was found by fluctuating 20 parameters that describe the leading-order PDF. These parameters, which can be considered eigenvectors of the PDF space, are orthogonal and were fluctuated independently in both the positive and negative directions. The central value of the MRST2007LO* PDF eigenvectors were not available at the time of this analysis, so the closest LO PDF set, MSTW2008LO (with 90% C.L.), was used. In terms of expected yield, the uncertainty as a function of mass was found to grow from 3% at the Z^0 peak to 6% at $m_{\mu\mu}$ = 1 TeV and 9% at $m_{\mu\mu}$ = 1.5 TeV (see Table 5.1). A cross check using the CTEQ 6.6 [52] PDF set to calculate the cross section was found to have a smaller uncertainty than the conservative estimate mentioned above. The PDF uncertainty was expected to affect the CI signal samples in the same way as for the DY, as the $q\bar{q}$ annihilation process is the same for both.

- *QCD K factor*:

  As discussed in section 5.2.1, PYTHIA was used to calculate the leading order cross sections with MRST2008LO* PDF sets, while PHOZPR was used to calculate the NNLO DY cross section using the MSTW2008NNLO PDF set. In addition, the NLO QCD K-factor calculation was also performed using the MSTW2008NLO PDF set, and the difference between NLO and NNLO calculations was used to estimate the uncertainty on the production cross section. The expected yield was assigned a 3% uncertainty at $m_{\mu\mu} = 1$ TeV growing linearly with mass. Because the QCD corrections only affect the initial quarks in the interaction (the internal process and final state are colorless), the uncertainty on K_{QCD} was expected to affect the CI signal samples in the same way as for the DY samples.

- *Electroweak K factor*:

  Higher order corrections were calculated using HORACE, which accounted for the effect of virtual gauge boson loops. Since real gauge boson emission was not taken into account in this calculation, the production cross section was underestimated by ∼2% at $m_{\mu\mu} = 1$ TeV. Higher order electroweak corrections and contributions of order α_s increased this uncertainty to 3%. The higher-order calculation neglected the running of the coupling constant, which was expected to have an additional 3% effect. The overall uncertainty on K_{EW} was then estimated to be 4.5% at $m_{\mu\mu} = 1$ TeV, growing linearly with mass. Because the electroweak K factor was only applied to DY, and any higher-order electroweak processes were by definition encoded in the scale Λ, this uncertainty was only applied to the DY sample and not the signal samples.

8.1.2 Experimental Uncertainties

The largest mass-dependent instrumental uncertainties were from muon reconstruction efficiency and momentum resolution. The calculation of these uncertainties as a function of $m_{\mu\mu}$ are discussed below.

- *Muon Reconstruction Efficiency*:

  Data driven methods such as the "tag-probe" could not be used to determine the mass-dependence of the muon efficiency, as little data was available in the tail of the distribution. One effect at high-momentum which may not have been modeled properly in simulation was combined reconstruction efficiency degradation due to showers in the MS from catastrophic energy loss, as muons begin to emit bremsstrahlung radiation in this energy regime, as described in section 2.4. A conservative 3% uncertainty at $m_{\mu\mu} = 1$ TeV, was applied to account for this.

- *Muon Resolution*:

  At high momentum, muon tracks are almost straight, and MS chamber misalignment can have a large effect on the muon p_T measurement. Due to the exponentially falling mass spectrum, this uncertainty in muon momentum resolution can cause event migration from low to high dimuon mass. The effect of the momentum resolution uncertainty was assessed by taking the full magnitude of the muon momentum correction to the simulation described in section 5.2.3 as the momentum resolution systematic uncertainty. This was found by fitting the ratio of invariant mass distributions with and without muon momentum corrections with a second order polynomial. The resulting function (with $m_{\mu\mu}$ having units of GeV)

$$dN_{res}(m_{\mu\mu}) = 1.001 - 1.33 \times 10^{-5} \times m_{\mu\mu} + 3.93 \times 10^{-8} \times m_{\mu\mu}^2 \qquad (8.1)$$

  corresponded to an uncertainty in N_{exp} which rose quadratically from 2.7% at $m_{\mu\mu}$ = 1 TeV to 10% at $m_{\mu\mu} = 2$ TeV relative to the Z^0 peak (Fig. 8.1).

8.1.3 Summary of Systematic Uncertainties

The uncertainties in $N_{exp}(m_{\mu\mu})$ are summarized in Table 8.1. With the exception of the muon momentum resolution uncertainty, each of these was taken as a linear function of $m_{\mu\mu}$, determined by using the value at the Z^0 peak and rising to the value obtained at $m_{\mu\mu} = 1$ TeV. The muon momentum resolution uncertainty had a quadratic dependence on mass, as mentioned previously. All of these uncertainties were assumed fully correlated in each mass bin.

The statistical errors quoted in Table 6.5 were used in the quadratic fits shown in Fig. 7.4. By taking these errors in each mass bin as fully correlated in $1/\Lambda^2$, an uncertainty in the N_{exp} extrapolation procedure was included in the systematic

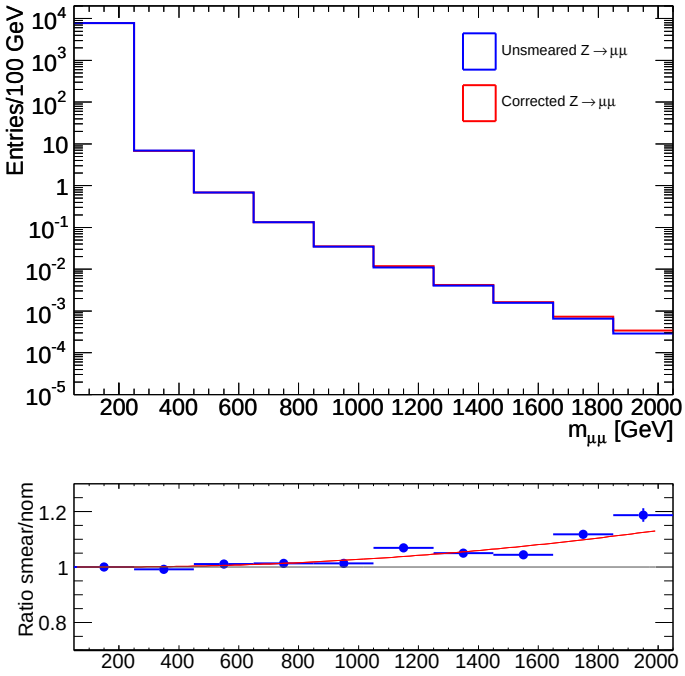

Figure 8.1. DY distributions before and after muon resolution smearing corrections. Though a small effect in the event yield, the ratio between smeared/nominal shows a $\sim 10\%$ difference at 2 TeV.

uncertainty calculation. This conservative estimate was the largest of all systematic uncertainties entering the analysis.

8.2 Marginalizing the Uncertainties in the Limit

During the creation of the invariant mass distributions, the functional form corresponding to each systematic uncertainty was applied individually as an event weight either as a function of true mass (in the case of K factor and PDF uncertainties) or reconstructed mass (in the case of muon efficiency and momentum resolution uncertainties). The functional form $\sigma_i(m_{\mu\mu})$ of the n_{sys} systematic uncertainties[1] was used to calculate asymmetric weights for each uncertainty i: $w_i^+ = 1+\sigma_i$ and $w_i^- = 1-\sigma_i$.

[1]This does not yet include the uncertainty in the N_{exp} extrapolation procedure, as it is not calculated as a function of $m_{\mu\mu}$.

Table 8.1. Systematic uncertainty in N_{exp} at $m_{\mu\mu} = 91$ GeV and at $m_{\mu\mu} = 1$ TeV. All systematics were linearly dependent on mass, with the exception of muon momentum resolution which had a quadratic dependence. The simulation samples on which each of these were applied are shown.

Systematic	at Z^0	at 1 TeV	Signal	DY-only	Other BGs
Trigger and Reconstruction Efficiency	0.3%	3%	✓	✓	✓
Muon momentum resolution	0.01%	2.7%	✓	✓	✓
PDF Uncertainty	3%	6%	✓	✓	
QCD K-factor	0.3%	3%	✓	✓	
EW K-factor	0.4%	4.5%		✓	

Families of $n_{sys} \times 2$ invariant mass distributions (N^i_Λ) were created for each simulation sample after weighing once with w_i^+ and once with w_i^-. Note that not all uncertainties were applied to every sample (as listed in Table 8.1). The difference between N_{exp} and N^i_Λ in k mass bins ($dN^{i,k}_\Lambda$) was calculated for both the full SM-only background and the benchmark signal samples. Taking the larger magnitude of either the up or down fluctuation for $dN^{i,k}_\Lambda$, the values in each mass bin were added in quadrature: $dN^k_\Lambda = (dN^1 \oplus dN^2 \oplus ... \oplus dN^{i+1})^k_\Lambda$. The uncertainty in the N^k_{exp} extrapolation procedure was also included here. Finally dN^k_Λ was fit in each mass bin as a function of $1/\Lambda^2$ to interpolate between the benchmark signal values (Fig. 8.2). This was done in a similar way as for N^k_{exp}, except that the total systematic uncertainty for background only ($1/\Lambda^2 = 0$) was not used in the fit because the systematics for the DY sample were treated differently than for the signal samples. The value of dN^k_Λ at a particular $1/\Lambda^2$ step became the width of the Gaussian prior in Eq. (7.6) in each mass bin.

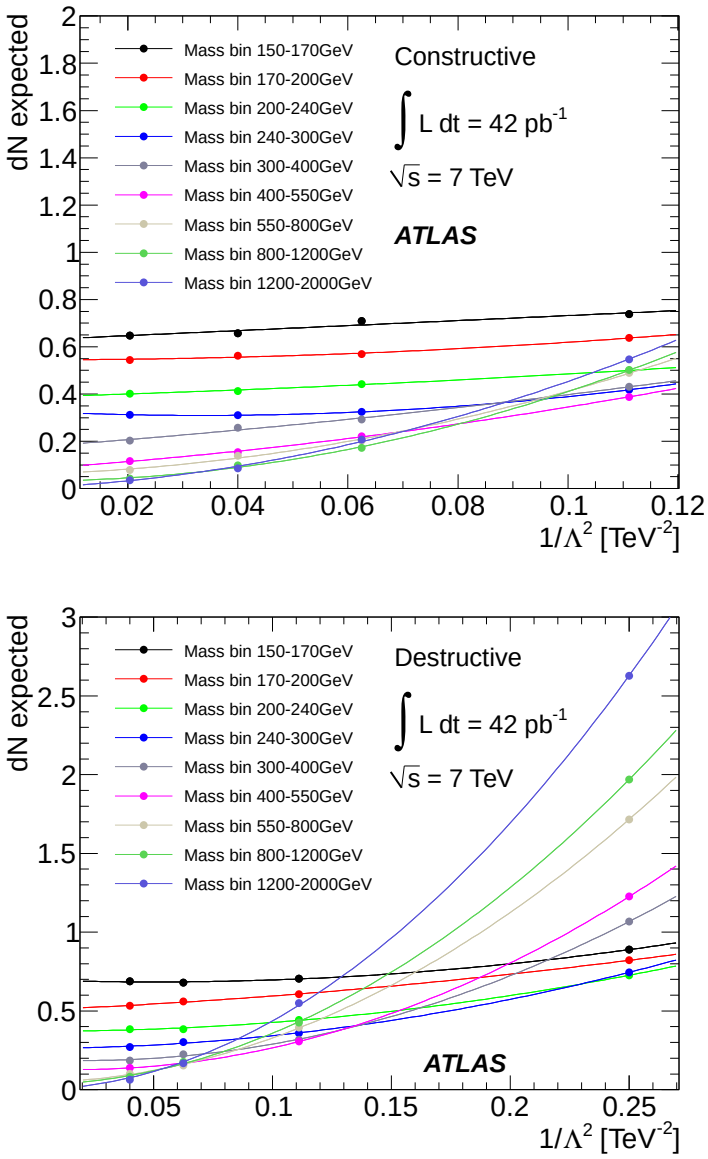

Figure 8.2. Values of dN_Λ^k in each mass bin for the constructive (top) and destructive (bottom) interference models shown as points corresponding to the benchmark signal samples. The second-order polynomial fits to dN_Λ^k as a function of $1/\Lambda^2$ in each mass bin are also shown.

CHAPTER 9

RESULTS AND OUTLOOK

After marginalizing systematic uncertainties as outlined in the previous chapter, the normalized PPDFs were built and the 95% credibility interval limits on the contact interaction scale Λ were found by integrating the PPDFs from $0 \rightarrow \theta_{lim}$. The PPDF distributions for $\theta = 1/\Lambda^2$ are shown in Fig. 9.1 and the distributions for $\theta = 1/\Lambda^4$ are shown in Fig. 9.2, for both the expected limit and the observed limit.

The observed lower limits on the 4-fermion contact interaction $q\,\bar{q} \rightarrow \mu^+\mu^-$ in the LLIM model for both constructive ($\eta = -1$) and destructive ($\eta = +1$) interference using the $1/\Lambda^2$ prior are:

$$\Lambda^- \ > \ 4.9 \text{ TeV (95\% C.L.)},$$
$$\Lambda^+ \ > \ 4.5 \text{ TeV (95\% C.L.)}.$$

These are the best limits to date. Table 9.1 shows the expected and observed limits for both priors considered, and also compares the limits with and without systematic uncertainties included. The observed limit obtained by choosing the $1/\Lambda^4$ prior over the $1/\Lambda^2$ prior is smaller by $\sim$0.3 TeV. The inclusion of systematic uncertainties decreases the limit by $\sim$0.1 TeV.

This analysis was performed with a small fraction of the total data which ATLAS will collect over its lifetime. In the next two years alone, 10 fb^{-1} or more of data are expected to be delivered by the LHC at $\sqrt{s}$ =7 TeV. Figure 9.3 shows the expected lower limits on contact interaction scales as a function of integrated luminosity

Table 9.1. Expected and observed lower limits on Λ with and without systematic uncertainties. The second decimal place is shown to illustrate the change with the addition of systematics.

		Expected Limit (TeV)		Observed Limit (TeV)	
	Prior	Constructive	Destructive	Constructive	Destructive
Without Systematics	Λ^{-2}	5.22	4.86	5.11	4.64
	Λ^{-4}	4.72	4.38	4.72	4.30
Including Systematics	Λ^{-2}	5.14	4.82	4.94	4.50
	Λ^{-4}	4.64	4.33	4.55	4.18

(without systematic uncertainties incorporated). While initially the reach will grow rapidly with the addition of more data, the attainable limit will eventually reach a maximum of roughly 12 TeV, limited by the center of mass energy of the colliding beams. However, more sensitivity to new physics may be gained by including the angular distribution of the dimuon system in the analysis and by performing the analysis in the dielectron channel as well.

In addition to the left-left isoscalar model of quark compositeness presented in this thesis, other models have a similar non-resonant final state structure, such as the large extra dimensions model discussed in section 1.3.2. This and other propagator and coupling forms of quark compositeness models will be studied at ATLAS in the future.

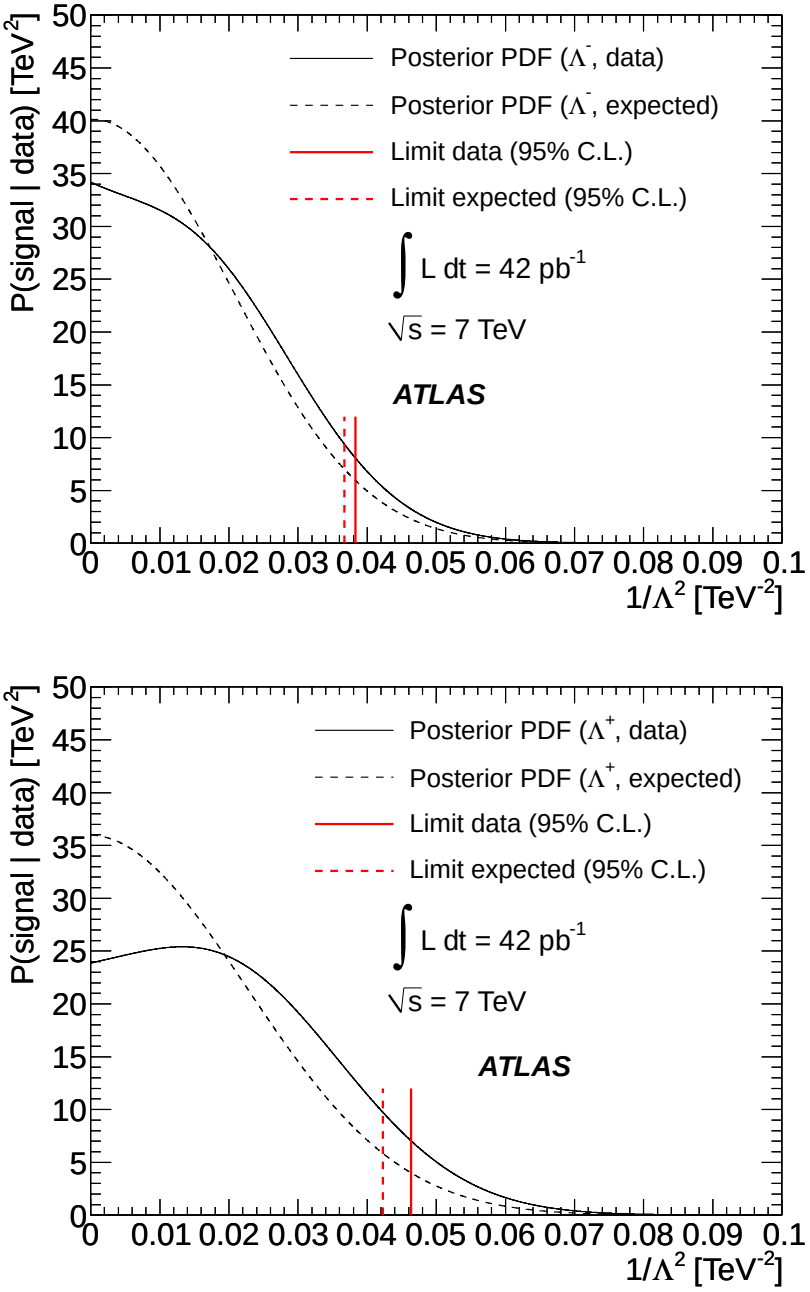

Figure 9.1. Posterior probability distributions with the $1/\Lambda^2$ prior for the expected (dashed line) and observed (solid line) number of events assuming constructive (top) and destructive (bottom) interference.

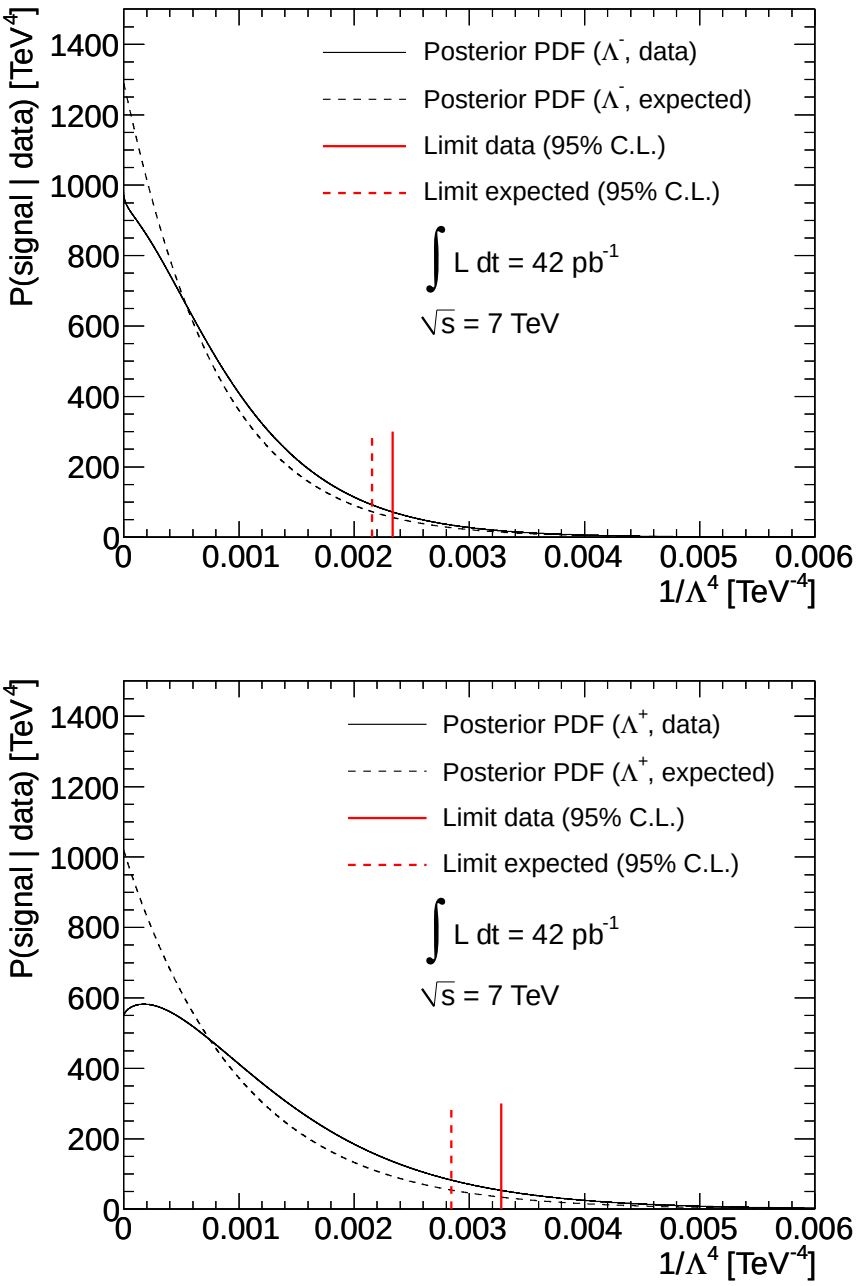

Figure 9.2. Posterior probability distributions with the $1/\Lambda^4$ prior for the expected (dashed line) and observed (solid line) number of events assuming constructive (top) and destructive (bottom) interference.

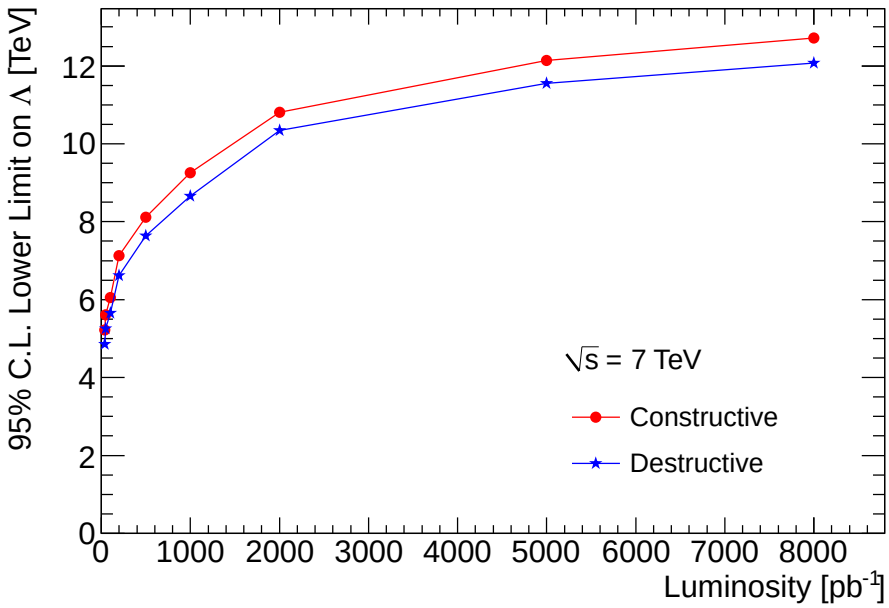

Figure 9.3. Lower limits expected (without systematics) on contact interactions as a function of total integrated luminosity.

CHAPTER 10

CONCLUSIONS

After the LHC began running with 7 TeV collisions in 2010, the ATLAS detector produced its first results with remarkable speed. Beginning with the measurement of the $Z \to \mu\mu$ cross section, high-mass dimuons in ATLAS were studied at $\sqrt{s} = 7$ TeV for the first time, surpassing the energy record previously held by the Tevatron.

Careful assessment of muon spectrometer performance and the selection of high quality muons allowed a search for new physics beyond the Standard Model to be performed with very little data. The left-left isoscalar model of quark compositeness was used as a benchmark search for non-resonant new physics where the energy scale of the new effective interaction can be higher than the hard scattering $\hat{s}$ achievable at the LHC. After performing a Bayesian binned-likelihood analysis, the best limits to date have been found, excluding the contact interaction scale Λ below 4.9 TeV for constructive interference and 4.5 TeV for destructive interference.

As the LHC pushes the energy and luminosity frontiers, ATLAS will continue the hunt for new physics at the electroweak scale and looks forward to discovering the answers to some of Nature's unsolved mysteries.

APPENDIX

CONTACT INTERACTION PYTHIA JOB OPTIONS

The job options used to generate contact interaction events in PYTHIA are shown below for $\Lambda = 2$ TeV, constructive interference:

```
"pysubs msel 0", # Users decay choice.
"pydat1 parj 90 20000", # Turn off FSR (use PHOTOS)
"pydat3 mdcy 15 1 0", # Turn off tau decays.

# turn on anomalous coupling
"pysubs msub 165 1", # via gamma* Z0
"pytcsm itcm 5 2",
"pytcsm rtcm 41 2000.0",
"pytcsm rtcm 42 -1",

"pysubs ckin 1 120.0", # Lower invariant mass.
"pyint2 kfpr 165 1 13", #choose decay into muons
"pypars mstp 32 4"
```

The definitions of flags are shown below:

- `ISUB` defines the following the contact interaction processes:

$$\begin{aligned}
\texttt{165} &= f_i f_i \to f_k f_k \quad (\text{via}\gamma^*/Z^0) \\
\texttt{166} &= f_i f_j \to f_k f_l \quad (\text{via}W^{\pm}) \\
\texttt{381} &= f_i f_j \to f_i f_j \\
\texttt{382} &= f_i \bar{f}_i \to f_k \bar{f}_k
\end{aligned}$$

- Setting a value to `ITCM(5)` turns on the type of model:

  1. Left-left Isoscalar model (u and d quarks only)
  2. Left-left Isoscalar model (all quarks)
  3. Helicity non-conserving model (u and d quarks only)
  4. Helicity non-conserving model (all quarks)

  Here, if `ITCM(5)` is set to `1`, the quark substructure is included only for up and down quarks. If `ITCM(5)=2`, then compositeness terms are included in the interactions between all quarks. If `ITCM(5)=0`, then `ISUB=165` and `ISUB=166` correspond to SM Z production and W production, respectively, and `ISUB=381` and `ISUB=382` correspond to $q_i q_j \to q_i q_j$ and $q_i \bar{q_i} \to q_k \bar{q_k}$, respectively.

- `KFPR(ISUB,1)=13` sets the final state flavor to muons for `ISUB=165, 166`

- `RTCM(41)` sets the scale Λ (in GeV)

- `RTCM(42)` sets the sign of interference (± 1)

- `MSTP(32)=4` is for using the $\hat{s}$ value for the interaction, rather than p_T^2. This is because in PYTHIA, $Z \to \mu\mu$ is a 2→1 interaction while the new coupling is treated as a 2→2 interaction.

BIBLIOGRAPHY

[1] S. D. Drell, and T. M. Yan. Massive lepton-pair production in hadron-hadron collisions at high energies. *Phys. Rev. Lett. 25*, 5 (1970), 316–320.

[2] G. Kane. The dawn of physics beyond the standard model. *Scientific American 288*, 6 (2003), 68–75.

[3] W. Pauli. Open letter to the Radioactivity Group at the Regional Meeting at Tübingen, Zürich, December 4, 1930.

[4] E. Fermi. Versuch einer theorie der β-strahlen / Towards the theory of β-rays. *Z. Phys. 88* (1934), 161.

[5] T. D. Lee, and C. N. Yang. Question of parity conservation in weak interactions. *Phys. Rev. 104*, 1 (1956), 254–258.

[6] C. S. Wu, E. Ambler, R. W. Hayward, D. D. Hoppes, and R. P. Hudson. Experimental test of parity conservation in beta decay. *Phys. Rev. 105*, 4 (1957), 1413–1415.

[7] R. P. Feynman, and M. Gell-Mann. Theory of the fermi interaction. *Phys. Rev. 109*, 1 (1958), 193–198.

[8] J. H. Christenson, J. W. Cronin, V. L. Fitch, and R. Turlay. Evidence for the 2π decay of the $k2$ meson. *Phys. Rev. Lett. 13*, 4 (1964), 138–140.

[9] N. Cabibbo. Unitary symmetry and leptonic decays. *Phys. Rev. Lett. 10*, 12 (1963), 531–533.

[10] S.L. Glashow, J. Iliopoulos, and L. Maiani. Weak interactions with leptonhadron symmetry. *Phys. Rev. D 2*, 1285 (1970).

[11] J.J. Aubert et. al. Experimental observation of a heavy particle j. *Phys. Rev. Lett. 33*, 23 (1974), 1404–1406.

[12] J. Augustin et. al. Discovery of a narrow resonance in $e+e-$ annihilation. *Phys. Rev. Lett. 33*, 23 (1974), 1406–1408.

[13] M. Kobayashi, and T. Maskawa. *Progress of Theoretical Physics 49*, 2 (1972).

[14] K. Nakamura et. al. Review of particles physics: The CKM quark-mixing matrix. *Journal of Physics G 37*, 075021 (2010), 150.

[15] S. A. Bludman. *Nuovo cimento 9*, 433 (1958).

[16] S. L. Glashow. Partial symmetries of weak interactions. *Nucl. Phys. 22* (1961), 579–588.

[17] S. Weinberg. A model of leptons. *Phys. Rev. Lett.*, 19 (1967), 1264–1266.

[18] A. Salam. Weak and electromagnetic interactions. *Elementary Particle Theory, Proceedings Of The Nobel Symposium Held At Lerum, Sweden* (1968), 367–377.

[19] D. Griffiths. *Introduction to Elementary Particles*. 1987.

[20] J. Donoghue, G. Golowich, and B. Holstein. *Dynamics of the Standard Model*. 1992.

[21] G. 't Hooft, and M. Veltman. *Nucl. Phys. B 44*, 1 (1972), 189–213.

[22] F. J. Hasert et. al. Search for elastic muon-neutrino electron scattering. *Phys. Lett. B 46* (1973), 121–124.

[23] F. J. Hasert et. al. Observation of neutrino-like interactions without muon or electron in the gargamelle neutrino experiment. *Phys. Lett. B 46* (1973), 138–140.

[24] G. Arnison et. al. Experimental observation of isolated large transverse energy electrons with associated missing energy at $\sqrt{s} = 540$ GeV. *Phys. Lett. B 122* (1983), 103–116.

[25] M. Banner et. al. Observation of single isolated electrons of high transverse momentum in events with missing transverse energy at the CERN anti-p p collider. *Phys. Lett. B 122* (1983), 476–485.

[26] G. Arnison et. al. Experimental observation of lepton pairs of invariant mass around 95-GeV/c^2 at the CERN SPS collider. *Phys. Lett. B 126* (1983), 398–410.

[27] P. Bagnaia et. al. Evidence for $Z^0 \rightarrow$e+ e- at the CERN anti-p p collider. *Phys. Lett. B 129* (1983), 130–140.

[28] M. L. Perl, and et al. Evidence for anomalous lepton production in $e^+ - e^-$ annihilation. *Phys. Rev. Lett. 35*, 22 (1975), 1489–1492.

[29] S.W. Herb, and et al. Observation of a dimuon resonance at 9.5 GeV in 400-GeV proton-nucleus collisions. *Phys. Rev. Lett. 39*, 5 (1977), 252–255.

[30] F. Abe, and et al. Observation of top quark production in $\bar{p}p$ collisions with the Collider Detector at Fermilab. *Phys. Rev. Lett. 74*, 14 (1995), 2626–2631.

[31] Abachi, S., and et al. Observation of the top quark. *Phys. Rev. Lett. 74*, 14 (1995), 2632–2637.

[32] K. Kodama, and et al. Observation of tau neutrino interactions. *Physics Letters B 504*, 3 (2001), 218–224.

[33] E. Eichten, I. Hinchliffe, K. Lane, and C. Quigg. Supercollider physics. *Rev. Mod. Phys. 56*, 4 (1984), 579–707.

[34] Th. Kaluza, and Sitzungsber. *Preuss. Akad. Wiss Phys. Math. Klassee, 996* (1921).

[35] O. Klein. *Z. F. Physik 37*, 895 (1926).

[36] N. Arkani-Hamed, S. Dimopoulos, and G. Dvali. *Phys. Lett. B 429*, 263 (1998).

[37] A. Gupta, N. Mondal, and S. Raychaudhuri. *e-Print hep-ph/9904234* (1999).

[38] G. Giudice, R. Rattazzi, and J. Wells. *Nucl. Phys. B 544*, 3 (1999).

[39] T. Han, J. Lykken, and R. Zhang. *Phys. Rev. D 59*, 105006 (1999).

[40] J. Hewett. *Phys. Rev. Lett. 82*, 465 (1999).

[41] E. Eichten, K. Lane, and M. Peskin. New tests for quark and lepton substructure. *Phys. Rev. Lett. 50*, 11 (1983), 811–814.

[42] D. Bourilkov. *e-Print hep-ex/0103039* (2001).

[43] D0 and CDF Collaborations, and G. Landsberg. *e-Print hep-ex/0412028* (2004).

[44] Nakamura et al. (Particle Data Group), K. *J. Phys. G 37, 075021* (2010).

[45] R.P. Feynman. *Photon-Hadron Interactions*. 1972.

[46] M. Breidenbach, J.L. Friedman, G.C. Hartmann, H.W. Kendall, and R.E. Taylor et al. *Phys Rev. Lett. 23*, 16 (1969), 930–939.

[47] A. D. Martin, W. J. Stirling, R. S. Thorne, and Watt, G. Parton distributions for the lhc. *Eur. Phys. J. C 63* (2009), 189–285.

[48] V.N. Gribov, and L.N. Lipatov. Deep inelastic e p scattering in perturbation theory. *Sov. J. Nucl. Phys. 15* (1972), 438–450.

[49] G. Altarelli, and G. Parisi. Asymptotic freedom in parton language. *Nucl. Phys. B 126* (1977), 298.

[50] Yu.L. Dokshitzer. Calculation of the structure functions for deep inelastic scattering and e+ e- annihilation by perturbation theory in quantum chromodynamics. *Sov. Phys. JETP 46* (1977), 641–653.

[51] J.C. Collins, D.E. Soper, and G. Sterman. Factorization of hard processes in qcd. *Adv. Ser. Direct. High Energy Phys. 5* (1988), 1–91.

[52] P. M. Nadolsky et. al. Implications of CTEQ global analysis for collider observables. *Phys. Rev. D 78*, 013004 (2008).

[53] T. Sjöstrand, P. Edén, C. Friberg, L. Lönnblad, G. Miu, S. Mrenna, and E. Norrbin. *Computer Phys. Commun. 135 (LU TP 00-30, hep-ph/0010017)* (2001).

[54] T. Sjöstrand, and P. Skands. Transverse-momentum-ordered showers and interleaved multiple interactions. *Euro. Phys. Journal C 39* (2005), 129–154.

[55] P. Golonka, and Z. Wąs. Next-to-leading logarithms and the PHOTOS Monte Carlo. *Euro. Phys. Journal C 50* (2007), 53–62.

[56] G. Corcella, I.G. Knowles, G. Marchesini, S. Moretti, K. Odagiri, P. Richardson, M.H. Seymour, and B.R. Webber. Herwig 6.5. *JHEP 0101 010* (2001).

[57] J. M. Butterworth, J. R. Forshaw, and M. H. Seymour. Multiparton interactions in photoproduction at HERA. *Z. Phys. C 72* (1996), 637–646.

[58] S. Frixione, and B.R. Webber. Matching nlo qcd computations and parton shower simulations. *JHEP 0206* (2002), 029. [hep-ph/0204244].

[59] C.M. Carloni Calame, G. Montagna, O. Nicrosini, and Vicini, A. "precision electroweak calculation of the production of a high transverse-momentum lepton pair at hadron colliders". *JHEP 0710*, 109 (2007).

[60] L. Evans, and P. Bryant. LHC machine. S08001.

[61] T.S. Virdee. The LHC project: The accelerator and the experiments. *Nucl. Inst. and Meth. A 623*, 1 (2010), 1–10. 1st International Conference on Technology and Instrumentation in Particle Physics.

[62] S. Myers. The LEP collider from design to approval and commissioning (lecture).

[63] CERN, http://public.web.cern.ch/public/en/research/AccelComplex-en.html.

[64] A. A. Glazkov, N. R. Lobanov, I. S. Balikoev, V. T. Barchenko, and S. I. Zagranichny. Duoplasmatron-type ion source with improved technical and operational performance for linear accelerator.

[65] The ATLAS Collaboration, G. Aad et al. The ATLAS Experiment at the CERN Large Hadron Collider. *JINST 3* (2008), S08003.

[66] The ATLAS Collaboration, G. Aad et al. Atlas pixel detector electronics and sensors. *JINST 3*, 07 (2008), P07007.

[67] The ATLAS Collaboration, G. Aad et al. The silicon microstrip sensors of the atlas semiconductor tracker. *Nucl. Inst. and Meth. A 578* (2007), 98–118.

[68] The ATLAS Collaboration. Performance of primary vertex reconstruction in proton-proton collisions at $\sqrt{s}$ =7 tev in the ATLAS experiment. Tech. Rep. ATLAS-CONF-2010-069, CERN, Geneva, 2010.

[69] The ATLAS Collaboration, G. Aad et al. The ATLAS TRT barrel detector. *JINST 3*, 02 (2008), P02014.

[70] The ATLAS Collaboration, G. Aad et al. The ATLAS TRT end-cap detectors. *JINST 3*, 10 (2008), P10003.

[71] The ATLAS Collaboration. ATLAS muon spectrometer : Technical Design Report. Geneva, 1997.

[72] http://proj-gaudi.web.cern.ch/proj-gaudi/.

[73] Identification of muon candidates in pp collisions at $\sqrt{s}$=900 gev with the ATLAS detector. Tech. Rep. ATLAS-CONF-2010-015, CERN, Geneva, 2010.

[74] P. Bagnaia, and et. al. Calibration model for the MDT chambers of the ATLAS Muon Spectrometer. Tech. Rep. ATL-MUON-PUB-2008-004, CERN, Geneva, 2008.

[75] The ATLAS Collaboration, G. Aad et al. Commissioning of the ATLAS Muon Spectrometer with cosmic rays. *Euro. Phys. Journal C 70* (2010), 875–916.

[76] The ATLAS Collaboration. Muon reconstruction efficiency in reprocessed 2010 lhc proton-proton collision data recorded with the ATLAS detector. Tech. Rep. ATLAS-CONF-2011-063, CERN, Geneva, 2011.

[77] *Nucl. Inst. and Meth. A 506* (2003), 250–303.

[78] A. Sherstnev, and R.S. Thorne. Parton distributions for lo generators. *Euro. Phys. Journal C 55* (2008), 553–575.

[79] L. Kashif. Measurement of the Z boson cross-section in the dimuon channel in pp collisions at $\sqrt{s}$ = 7 TeV. Thesis (http://www.hepl.harvard.edu/theses), 2010.

[80] The ATLAS Collaboration. Measurement of the $Z \to ll$ production cross section in proton-proton collisions at $\sqrt{s}$ = 7 tev with the ATLAS detector. In *35th. International Conference on High Energy Physics, Paris, France* (2010). ATLAS-CONF-2010-076.

[81] The ATLAS Collaboration. Measurement of the $W \to l\nu$ and $Z/\gamma^* \to ll$ production cross sections in proton-proton collisions at $\sqrt{s} = 7$ tev with the ATLAS detector. *JHEP* (2010). arXiv:1010.2130 [hep-ex].

[82] The ATLAS Collaboration. Luminosity determination using the ATLAS detector, 2010. ATLAS-CONF-2010-060.

[83] The ATLAS Collaboration. Updated luminosity determination in *pp* collisions at $\sqrt{s}$ = 7 TeV using the ATLAS detector. In *46th Rencontres de Moriond on Electroweak Interactions and Unified Theories* (2011). ATLAS-CONF-2011-011.

[84] https://twiki.cern.ch/twiki/bin/view/AtlasPublic/MuonPerformancePublicPlots.

[85] The ATLAS Collaboration. Muon momentum resolution in first pass reconstruction of pp collision data recorded by ATLAS in 2010. Tech. Rep. ATLAS-CONF-2011-046, CERN, Geneva, 2011.

[86] The ATLAS Collaboration. Alignment of the ATLAS inner detector tracking system with 2010 LHC proton-proton collisions at $\sqrt{s} = 7$ TeV. ATLAS-CONF-2011-012 (2011).

[87] R. Hamberg, W. L. van Neerven, and T. Matsuura. A complete calculation of the order $\alpha - s^2$ correction to the Drell-Yan K factor. *Nucl. Phys. B 359* (1991), 343–405.

[88] The ATLAS Collaboration. Studies of the performance of the ATLAS detector using cosmic-ray muons. *Eur. Phys. J.* (2011). arXiv:1011.6665.

[89] see for example: F. James. *Statistical Methods in Experimental Physics.* World Scientific Publishing Co. Pte. Ltd., 2006.